The Effect of Microwave Energy on Sintering

Raghunath Rao Thridandapani

Dissertation submitted to the Faculty of the

Virginia Polytechnic Institute and State University in partial fulfillment of the requirements for the degree of

Doctor of Philosophy

In

Materials Science and Engineering

David E. Clark, Chair

Robert W. Hendricks

Guo-Quan Lu

Gary R. Pickrell

April 1st, 2011

Blacksburg, Virginia

Keywords: Microwaves, Sintering, Activation Energy, Zirconia

Copyright © 2010 Raghunath Rao Thridandapani

The Effect of Microwave Energy on Sintering

Raghunath Rao Thridandapani

ABSTRACT

Spent Nuclear Fuel (SNF) is a by-product of existing nuclear reactors; SNF consists of long-lived radioactive actinides which have an average half-life of several thousand years (e.g. Plutonium-239 with a half-life of 24,000 years, and Americium-243 with a half-life of 7,360 years). Several multinational organizations are making an attempt to extract the energetic value out of these nuclear stockpiles in order to minimize the risk of nuclear proliferation and reduce waste volume. The Inert Matrix Fuel (IMF) concept is being considered as an option to reuse the radioactive actinides present in spent nuclear fuel by means of a transmutation process. Due to the volatile nature of these radioactive actinides, it is expected that the high-temperature conventional processing of IMFs will result in a significant loss of material.

This study investigates microwave sintering of inert matrix material (excluding actinide fuel) as an alternative route to conventional processing. It was observed that microwave sintering showed a reduction of 300 °C in temperature required for full densification when compared to conventional sintering. The reduction in sintering temperatures did not show any significant variation in the resulting properties (hardness and grain size). While these results satisfy the need for the application, it is important to understand why microwaves enhance the sintering phenomena.

It is speculated (by many researchers) that the electric field associated with microwave energy is enhancing flux leading to accelerated densification during microwave sintering. This study has observed a decrease in the activation energy (for sintering 8YZ) with the increase in the magnitude of the applied electric field.

Copyright © 2010 Raghunath Rao Thridandapani

All text, illustrations, graphs, tables, figures, photos and other supplementary material included in this dissertation were created and typeset for publication by the author in Times New Roman, Calibri and Arial Fonts using the free LaTeX document preparation system. Statistical analyses and graphs were obtained using Excel. Additional illustrations were created in Inkscape 0.48 and Microsoft Office 2010.

This dissertation is licensed for public use under the Creative Commons Attribution-Noncommercial-Share-Alike License 3.0. You are free to share, copy, distribute and transmit this work, and build upon it for non-commercial purposes under the following conditions: (1) you agree to attribute the work to the author and (2) if you alter, transform, or build upon this work, you may distribute the resulting work only under the same or similar license to this one. The full legal code is available at http://creativecommons.org/licenses/by-nc-sa/3.0/legalcode.

Acknowledgments

I would like to acknowledge, the Department of Energy, for funding this work (project no. DE-F07-06-ID 14731). I am grateful to Dr. David E. Clark and Diane C. Folz for recruiting me in carrying out this project. This research would not have been complete without their guidance and support. They have always greeted my expensive failures with a smile and constantly reminded me to stay focused on the target.

I feel lucky to have Dr. Clark as my guru; his relentless persistence with teaching is commendable. He has been one of my tough taskmasters, who was able to extract the best work out of me. For me, he has been a guide, a leader, and an example. Thank you. Working with Diane on many occasions has been an unforgettable experience. She was never too busy to point me in the right direction to solve a particular problem or to provide general guidance.

Sincere thanks to the members of the committee, Dr. Robert W. Hendricks, Dr. Guo-Quan Lu, and Dr. Gary R. Pickrell, for their insightful questions and comments.

Carlos E. Folgar, Morsi M. Mahmoud, and Patricia Mellodge, thank you for teaching me the basic skill-set needed for designing the generic hardware and software used for this study. This was an irreplaceable asset to my research.

I owe special thanks to all of my friends in India and the United States for their willingness to help me whenever needed. Finally, I am indebted to my ever loving parents and my brother, Chintu for their endless support and patience.

Contents

List of Figures

List of Tables

List of Symbols

C_p	Heat capacity of the material
D	Diffusion coefficient
D_p	Depth of penetration
E	Energy supplied from an external source
E_{rms}	Root mean square of the electric field
G	Diameter of grain
G_γ	Surface free energy
HV	Vickers hardness number
J	Flux of the diffusing species
$J_{C_\alpha A_\beta}$	Flux of the lattice molecule $C_\alpha A_\beta$
K	Equillibrium constant
L_T	Length of the test line
$L_\circ$	Initial length of the sample
N	Avogadro's number, 6.023×10^{23}
N_l	Number of intercepts per unit test line
P	Applied load
Q	Activation energy
R	Universal gas constant, $8.314\, J\, K^{-1} mol^{-1}$
T	Temperature

W_D	Weight of the dry sample
W_{ss}	Weight of the suspended saturated sample
W_s	Weight of the saturated sample
$\Delta G^{\dagger}$	Activation energy
Γ_1	Scaling parameter proportionate to the mean diffusion distance, driving force and other geometric features
Ω	Atomic volume
$\bar{X}$	Arithmetic mean
$\frac{dL}{dt}$	Rate of change in linear dimension
γ	Surface energy
λ	Interatomic distance
$\mathbf{k_b}$	Probability of backward jump
$\mathbf{k_f}$	Probability of forward jump
$\mathbf{k}$	Reaction rate constant
μ	Chemical potential
ν	Frequency of vibration
$\overline{K}$	Geometric constant
$\bar{l}$	Mean lineal intercept
ρ_L	Density of water
ρ_b	Bulk density
ρ_t	Theoretical density
σ	Standard deviation
$\varepsilon^{'}$	Relative dielectric constant
$\varepsilon_c^{''}$	Dielectric loss due to long range displacement of charges
$\varepsilon_d^{''}$	Dielectric loss due to dipolar rotation
$\varepsilon_{eff}^{''}$	Relative effective dielectric loss

$\varepsilon_e^{''}$	Dielectric loss due to electronic polarization
$\varepsilon_i^{''}$	Dielectric loss due to ionic polarization
$\varepsilon_s^{''}$	Dielectric loss due to interfacial polarization
ε_o	Permittivity of free space, $8.85 \times 10^{-12}\ \frac{F}{m}$
$\widetilde{D}$	Effective diffusion coefficient
c	Concentration
d	Particle diameter
d_l	Length of the diagonal
f	Frequency
k	Boltzmann constant, $1.38 \times 10^{-23} m^2\ kg\ s^{-2}\ K^{-1}$
x	Length of a neck region between two particles

Chapter 1

Introduction

1.1 Microwave energy for sintering

The applications of microwave technology in remote sensing, telecommunication, and food processing industries have had significant impacts on our standards of living. For example, Radio Detection and Ranging (RADAR) is a remote sensing technique that utilizes microwave frequency signals for detecting weather changes, enforcing speed limits, and regulating air-traffic control [1]. With the invention of the satellite in 1957, long-distance communications were possible that used microwaves for sending signals [2]. Early on, microwaves were limited to communications, but it was later found that this energy could be used for heating applications [3]. Now, the microwave oven is a common household kitchen appliance that is used for rapidly heating food.

Microwave technology has proven to be useful in a number of applications and is currently used for processing different materials as an alternative route to conventional processing techniques (details in Section 2.3). The application of microwave heating for sintering some ceramics has resulted in low-temperature processing when compared with conventional sintering methods [4, 5, 6].

1.2 Motivation for this study

Uranium oxide is widely used as a fuel material in nuclear reactors (light and heavy water reactors). The energy released due to the fission reaction of uranium in the form of ^{235}U is $\sim$200 MeV, which is used to produce electricity [7]. As only 4 % of the fuel is fissile (^{235}U), the rest of the fuel consisting of the ^{238}U isotope captures neutrons to form transuranic nuclides (Pu, Np, Am, and Cm). Most of these end up in the Spent Nuclear Fuel (Spent Nuclear Fuel (SNF)) pool, an on-site storage at nuclear reactors [7]. Disposing of these long-lived radio nuclides (e.g.^{239}Pu with a half-life of 24,000 years, and ^{243}Am with a half-life of 7,360 years) raises questions about the long-term integrity of storage facilities [8, 9, 7].

One of the methods proposed for recycling the radioactive material present in the SNF uses the Inert Matrix Fuel (IMF) concept [10, 11]. The actinides from the SNF are added to a matrix material that is transparent to neutrons. This will allow selective incineration of the actinides, as opposed to their production [12]. The long-term goal of the study presented in this dissertation is to use microwave technology for fabricating IMFs to minimize the overall processing cycle.

Sintering is a phenomenon of consolidating particles by developing bonds between them. Bonding between particles becomes significant at temperatures that are 0.5 to 0.7 times that of their melting temperature [13]. Conventional sintering of ceramic-based nuclear fuel involves high-temperature processing, generally above 1600 °C [14]. As the actinide materials tend to exhibit high vapor pressures at these temperatures [15], it is expected that these processing temperatures will result in significant loss of actinides during inert matrix fuel fabrication.

One possible approach to prevent the loss of material during processing (sintering) is to adopt alternative methods for decreasing the processing temperatures. For this study, microwave sintering is being considered, as this technique has been shown to potentially enhance densification at lower temperatures within a shorter period of time for many ceramic materials [4, 5, 6, 16].

1.3 Goals and Objectives

During sintering, flux (matter flow through a unit area per unit time) is required for both densification and grain growth. It is speculated that enhanced densification during microwave sintering is an indirect indication of enhanced flux [17]. Reports in literature (as well our own work) also have shown an acceleration in grain growth during microwave sintering [18, 19]. However, the present study will not be addressing the phenomena of enhancement in grain growth during microwave sintering. It should be noted that critics of microwave processing believe that enhanced sintering (and grain growth) are the result of inaccuracies in temperature measurement.

Typically, densification (during sintering) is quantified as follows

$$\frac{\Delta\rho}{\rho} \approx \left(\frac{\Delta L}{L_\circ}\right)^3 = -\left(\overbrace{\underbrace{D_\circ \exp\left(-\frac{Q}{RT}\right)}^{\text{Transport Coefficient}} \overbrace{\frac{\gamma_{sv}}{n}\frac{dA}{dx}}^{\text{Driving Force}} \frac{c}{RT}}^{\text{Flux}} \overbrace{\frac{2\pi V_m x^2}{a^3}}^{\text{Material Constants}}\right)^{\frac{3}{2}} t^{\frac{3}{2}} \tag{1.1}$$

A detailed description of the above equation is presented in Appendix A.1. In Equation 1.1, $\frac{\Delta\rho}{\rho}$ and $\frac{\Delta L}{L_\circ}$ represent the relative change in density and linear shrinkage, respectively; these parameters are used to monitor the extent of sintering. It is a common practice to measure $\frac{\Delta\rho}{\rho}$ during isothermal sintering experiments and $\frac{\Delta L}{L_\circ}$ (using a dilatometer) during non-isothermal sintering experiments.

Generally, flux is defined as a product of the *transport coefficient* and the *driving force* (see Equation 1.1).

$$[\text{Flux}] = -[\text{Transport coefficient}] \times [\text{Driving force}] \tag{1.2}$$

According to Equation 1.2, enhanced flux could result from an increase in the *transport coefficient*, the *driving force* or both. Several studies investigated the enhancement in flux by focusing on either one of these terms, assuming that the other term was unaffected by the microwave field [18, 20, 21, 22]. The main driving force for conventional sintering is the reduction in surface energy, $\frac{\gamma_{sv}}{n}\frac{dA}{dx}$. In microwave processing, the electric field may be increasing the transport coefficient (through a reduction in Q), or the driving force.

Earlier investigations have focused on measuring the activation energies, Q, for studying the effect of microwaves on the transport coefficient (see Equation 1.1). Many reports have found that microwave sintering has resulted in reduction of measured activation energies that led to an

increase in the transport coefficient [20, 18], thereby enhancing flux. Likewise, it is speculated that the electric field component of the microwave is providing an additional driving force during microwave sintering. This is believed to be increasing the overall flux leading to accelerated densification. Freeman et al [21] have observed enhanced ionic currents in single-crystal NaCl with the increase in applied microwave field. These ionic currents were attributed to the presence of an additional driving force induced by the electric field associated with microwaves. Based on a series of sintering studies in a hybrid furnace, Wroe and Rowley [22] attributed the enhancement in microwave sintering to an additional driving force induced by the electric field. Presently, it remains unclear whether a reduction in the activation energy, the presence of an additional driving force, or both is responsible for the observed enhancement in sintering.

The main goals of this work are twofold. Firstly, to reproduce the enhanced densification (with microwave sintering) eliminating the possibility of inaccuracy in temperature measurement. Secondly, to attempt to understand which of the terms, if any, in the flux equation (Q or the driving force) is leading to enhanced densification during microwave sintering.

The following objectives have been outlined to achieve the goals set-forth for this dissertation:

1. A thorough literature review in the area of conventional and microwave sintering (Section 2.3 and 2.4).

2. Develop a microwave dilatometer to validate the temperature measurements and to monitor the microwave sintering process (Section 3.3.6).

3. Evaluate the microwave sintering behaviour of 8 mol % Y_2O_3-stabilized ZrO_2 relative to

conventional sintering with isothermal and non-isothermal methods (Section 4.4).

4. Examine the microstructural differences (if any) due to microwave and conventional sintering techniques (Section 4.4).

5. Investigate the variation in measured activation energies with the electric field intensity (oscillating at 2.45 GHz) (Section 4.5.2).

6. Provide some insight into the role of microwave energy on sintering (Chapter 5).

Chapter 2 outlines the necessary background on solid state sintering and provides a literature review on sintering ceramics using microwave energy. Chapter 3 presents detailed information on different experimental methods adopted for this research. The results obtained for this study are discussed in Chapter 4 followed by Chapter 5 which summarizes the conclusions drawn from this investigation. Chapter 6 proposes the possible future work. The Appendix A provides relevant calculations and Appendix B provides details of the equipment designed for this study. Appendix C, D and E provides the supporting information used in this study.

Chapter 2

Background

This section provides (1) a background on inert matrix fuels and issues with fuel fabrication, (2) a study on the atomistic view of diffusion with respect to solid state sintering, and (3) an introduction to microwave energy in general and relevant reports on microwave sintering.

2.1 Inert matrix materials

The nuclear power industry is receiving more attention due to the interest in adopting cleaner fuel. Nuclear reactors are used to generate electricity by means of a fission reaction. Uranium dioxide (UO_2) is a common nuclear fuel, consisting of ^{235}U (4 wt.%), a fissional isotope, and ^{238}U (96 wt.%), a fertile isotope [7]. During the nuclear reaction the fissionable nuclei (^{235}U) splits, releases energy and produces additional neutrons. The energy released during a fission reaction is $\sim$200 MeV, that is used for producing electricity [23]. Part of the neutrons generated during

fission reactions is captured by the fertile ^{238}U isotope, transmuting it into isotopes of plutonium (Pu) and actinides in the reactor. A typical fuel pellet provides useful energy for about 3 years after which, the fuel is removed, and stored in on-site storage facilities (spent fuel pools and dry cask storage) [23].

While ^{235}U contributes to producing energy, the ^{238}U isotope breeds artificial fissile materials such as plutonium (^{239}Pu), americium (^{243}Am), curium (^{245}Cm), and neptunium (^{237}Np). Although part of these nuclides contribute to energy production, most of them end up in spent nuclear fuel. Because existing nuclear reactors adopt a once-through fuel cycle strategy, most of these isotopes end up in on-site storage facilities.

By the end of last century, the world's inventory of plutonium (excluding other actinides) coming from the civilian reactors was estimated to be 1700 tons [24]. Disarmament due to the end of the *Cold War* resulted in an additional 200 tons of Pu [25]. In order to dispose of excess plutonium, mixed oxide (MOX) fuels (5 % PuO_2 + 95 % UO_2) were developed [26]. However, the presence of ^{238}U in MOX fuels resulted in a constant production of Pu at a rate higher than its consumption [9].

The risk of nuclear proliferation from the fuel stockpiles led to the formation of the Global Nuclear Energy Partnership (GNEP), a consortium between different nations. The goal of GNEP is to reduce the proliferation risk from existing nuclear stockpiles by reusing them. As part of the GNEP program, The United States Department of Energy's, Office of Nuclear Energy, Science and Technology has initiated Advanced Fuel Cycle Initiative (AFCI). The AFCI focuses on developing programs that provide transition for existing nuclear reactors from using once-through fuel

cycle to a more efficient advanced fuel cycle. The AFCI program develops advanced fuel cycle technologies for next generation (Gen IV) nuclear reactors [27, 28].

The concept of an advanced fuel cycle is shown in Figure 2.1a; it consists of separations technology, fuels technology, and transmutation technology [12]. Separations technology focuses on separating the usable actinide materials from the spent nuclear fuel. Fuels technology aims at fabricating metallic, mixed oxide, and nitride fuels. The purpose of transmutation technologies is to develop strategies for extracting energy by transforming highly radioactive actinides into their lighter counterparts in advanced reactors [27, 28].

Figure 2.1b outlines the Inert Matrix Fuel (IMF) concept that satisfies AFCI requirements [12]. The actinide materials separated from the SNF are added to an inert matrix that is transparent to neutrons. The idea behind replacing the fissile matrix (^{238}U) with a neutron-transparent matrix is that it eliminates the plutonium breeding process in the reactors [25]. The major advantage of IMFs over MOX is that there is no production of fissile isotopes due to the fuel matrix. The goal of using IMFs is to transmute the highly radioactive actinides to their lighter counterparts in Gen IV reactors, enabling safe disposal at the proposed geological repositories.

The primary requirement of matrix materials for IMF compositions is its transparency to neutrons. Compatibility of inert matrices with the fissile material, reactor coolant, and structural materials are also important. A comprehensive review summarizing the research on identifying materials sutiable for inert matrices is provided in "*Viability of inert matrix fuel in reducing plutonium amounts in reactors*" prepared by the International Atomic Energy Agency [25]. In many cases, physical and chemical properties of the inert matrix are compared with UO_2 as a reference.

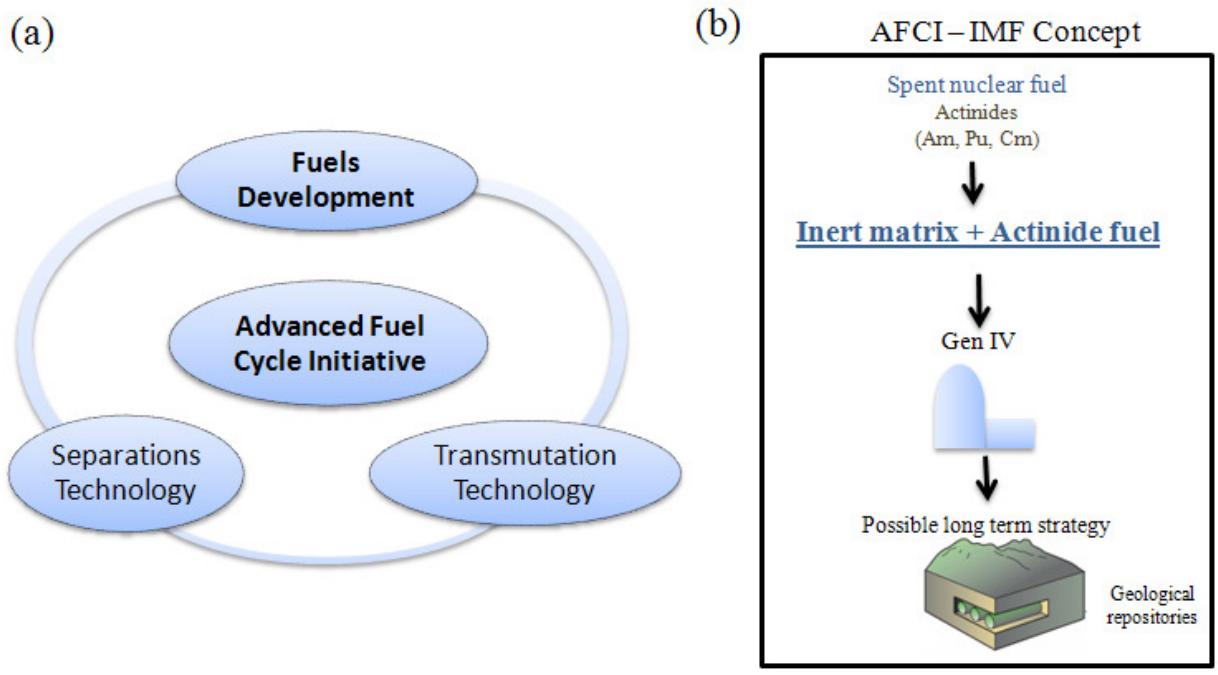

Figure 2.1: (a) Technologies developed by Advanced Fuel Cycle Initiative (AFCI) as a part of Global Nuclear Energy Program, and (b) Inert Matrix Fuel, an AFCI concept for reusing the spent nuclear fuel.

Some of the desired properties for the inert matrix materials are outlined below [25]:

- Low neutron absorption cross section
- High melting point
- Good thermal conductivity
- Good compatibility with the cladding
- Low solubility in the coolant
- Low swelling under irradiation
- Good mechanical properties
- High density

Inert matrix compatibility issues are examined experimentally in test bed reactors before any manufacturing efforts take place. Preliminary studies focus on investigating the sintering behavior (of IMFs) through non-radioactive surrogates [29]. So far, none of the IMFs has been licensed for use in commercial reactors. Only after successful demonstration that the new fuel will meet the safety limits will this technology be transferred for licensing.

2.2 Fuel fabrication issue

The majority of the actinide materials present in the SNF have a tendency to exhibit an increase in vapor pressures with the increase in temperature [30, 31]. Americium (see Figure 2.2) exhibits

a high vapor pressure as compared with other actinides; therefore, this material is considered to be the most volatile species. It is for this reason that processing methods target retention of Am during IMF fabrication.

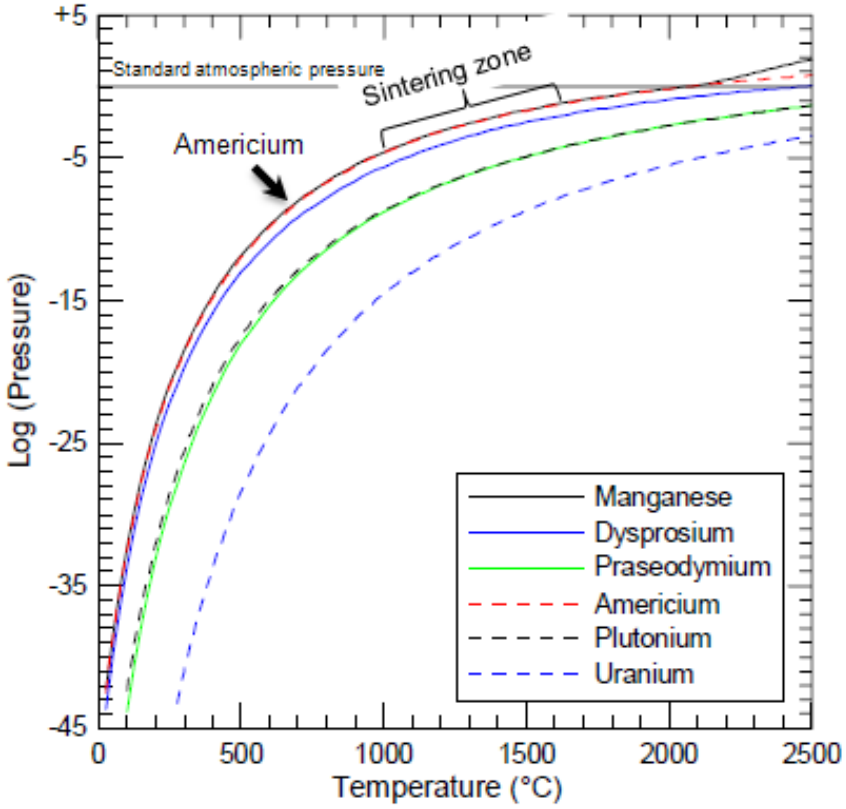

Figure 2.2: Vapor pressure as a function of temperature for various actinide materials present in spent nuclear fuel [31] (used with permission, J. J. Moore, in: 2007 ANS/ENS International Meeting and Nuclear Technology Expo, Washington D.C).

Conventional processing of ceramic nuclear fuel usually involves sintering at temperatures ranging from 1000 to 1600 °C [14]. As seen in Figure 2.2, along these sintering temperatures there is a four-fold increase in saturated vapor pressure of Am. It can be seen that these vapor pressures are approaching the normal atmospheric pressure at which the materials tend to lose mass through evaporation. It is expected that this tendency will result in a significant loss in actinide materials (such as Am) during sintering. In order to minimize the loss in fuel material, alternative processing routes are being considered for fabricating IMFs. One possible approach is to adopt microwave processing, which has been shown to decrease the overall processing time and temperature (for details see Section 2.4.4).

The following section provides a background study on the atomistic view of different mechanisms responsible for solid state sintering. This will be the fundamental basis for understanding the effects of microwave energy on sintering.

2.3 Solid state sintering of ceramics

Sintering is a one of the oldest techniques used for fabricating ceramic components. It dates back to 10,000 BC (Jomon pottery discovered near Nagasaki, Japan) for making earthenware utensils and extends to its modern application in fabricating nuclear fuels for generating energy [32].

Sintering is defined as a process of compacting particles via matter transport events that occur at an atomic scale [13]. Sintering studies aim at understanding the relationship between processing parameters and the resulting microstructures that control the final properties [33]. Sintering is

classified into (a) solid state, and (b) liquid state sintering. The difference between these two types of sintering is that the inter-particle growth takes place with and without the presence of a liquid phase [33]. Solid state sintering is the technique adopted for fabricating IMF materials. Therefore a fundamental understanding of this method will be the main focus of this section.

2.3.1 Driving force for sintering

The main driving force for sintering a system of particles is the reduction in overall surface free energy, G_γ, of a powdered compact (consolidated powder) [17]. Figure 2.3 shows a simplified sketch of sintering between two spherical particles.

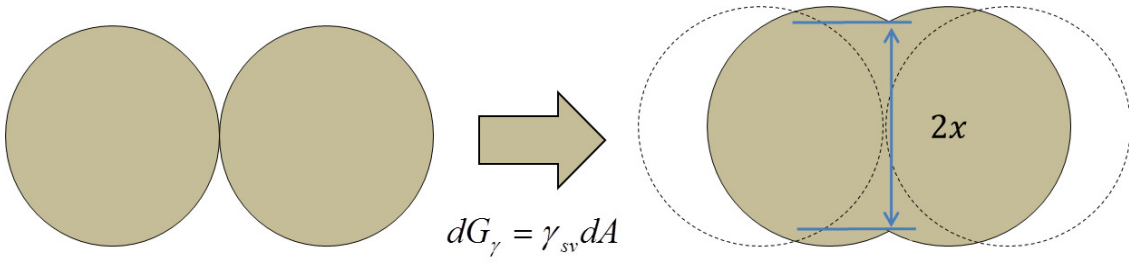

Figure 2.3: Change in surface area between particles before and after sintering.

The region of contact between the two particles is often referred to as the neck region. This region is marked as $2x$ in Figure 2.3. During sintering, high-energy free surfaces are replaced by lower energy sites such as grain boundaries or crystalline regions [34, 33, 13]. The formation of these low-energy sites (neck region), and subsequent reduction in surface area, results in a decrease in the overall surface energy of the powdered compact.

2.3.2 Transport mechanisms for sintering

During sintering, there is a gross flux, J, of the material to the neck regions [35], resulting in a reduction in surface energy of the powdered compact. The rate and the direction at which atoms move during the sintering process is governed by the driving force (reduction in surface energy) and this movement is usually termed as *diffusion*.

Diffusion is a common phenomena observed in gases where there is a wide separation between different molecules, e.g., gas spreading out of a container will occupy the available volume of space. Homogenization of ink droplets in water is another example of diffusion taking place in liquids. In crystalline solids, the atoms are orderly arranged and this makes the situation a little different to the diffusion observed in gasses[1], and in liquids[2]. The ordered arrangement of atoms in solids will cause diffusion to occur at a much slower rate than liquids or gases.

There are many ways in which the atoms can move in a solid: some of the possible ways are shown in Figure 2.4 [36, 37]. The likelihood of a jumping pattern shown in Figure 2.4 depends on the energy requirement; only those jumps are favourable that require the lowest energy. For example, vacancy exchange mechanism is preferred to the direct exchange mechanism.

The diffusion phenomena (Figure 2.4) in solids is a high temperature process and is not readily observed at room temperatures. This is due to the fact that atoms in a solid state cannot move freely as liquids and gasses. It is only at high temperatures that the atoms in solid materials will experience an increase in kinetic energy favouring diffusional events. During sintering, diffusion

[1] In gasses, atoms have a random arrangement

[2] In liquids the arrangement of atoms is neither ordered nor random

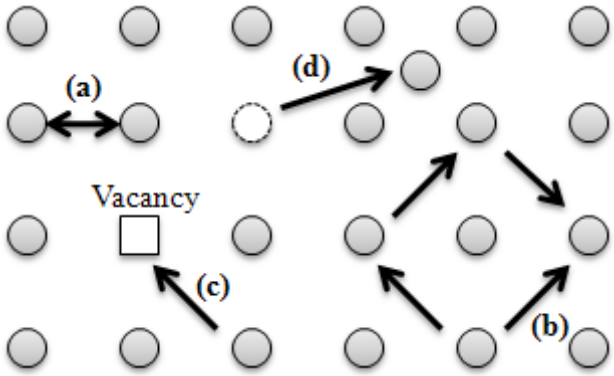

Figure 2.4: Some of the possible atomic level diffusional events in an imaginary solid: (a) direct exchange, (b) ring type of rotation, (c) vacancy exchange, and (d) interstitial mechanicsm.

takes place under the influence of a driving force (reduction in surface area). The result of small scale individual atomic jumps along the direction of driving force (from A $\rightarrow$ B in Figure 2.5) is observed as a large-scale migration of matter. The flux of the material during solid state sintering occurs along different paths; these are outlined in Figure 2.5.

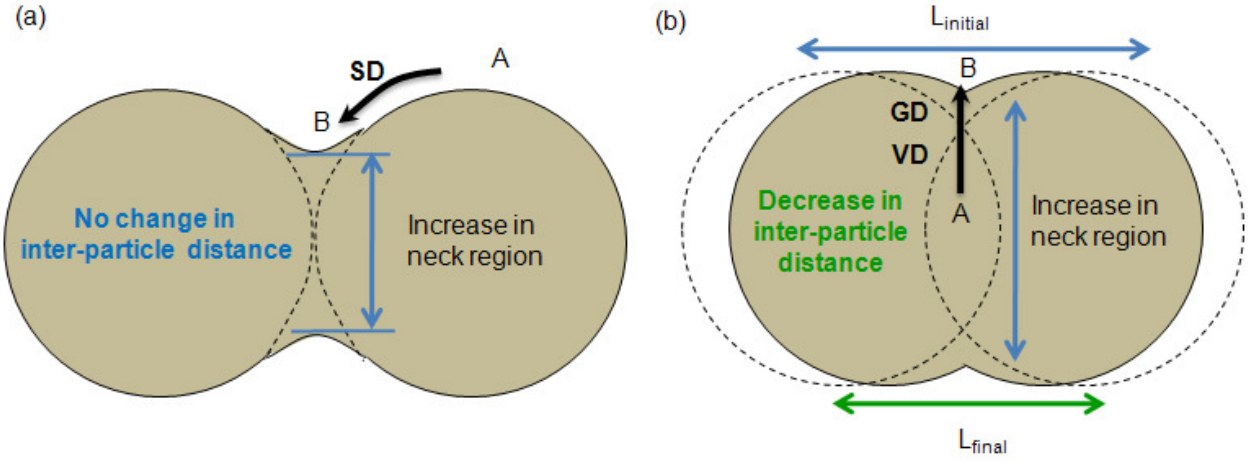

Figure 2.5: Schematic sketches of (a) non-densifying mechanisms (surface diffusion), and (b) densifying mechanisms (volume and grain boundary diffusion).

Surface Diffusion (SD): Transfer of material takes place from the surface of the particle to the

neck (Figure 2.5a) [34, 17]. This type of diffusion is due to the pressure difference associated with the convex surface of the particle (point A in Figure 2.5a) and the concave surface of the neck region (point B in Figure 2.5a) [17]. It was observed that at high enough temperatures the transfer of material takes place through evaporation/condensation; this phenomena is termed as vapor transport.

Volume Diffusion (VD): The difference in vacancy concentration along the neck region and the particle interior (Figure 2.5b) allows matter transport from the interior of the particle to the neck region [17]. During VD, the material transfer occurs through vacancies, interstitials, and substitutional atoms that are present within the lattice region.

Grain Diffusion (GD): This type of diffusion is similar to VD, except that the matter transport occurs along the grain boundary regions (Figure 2.5b) [13, 34].

An actual sintering run involves a mixture of all of the mechanisms discussed above, but they shift in dominance depending on the sintering conditions [13]. Surface diffusion contributes to the growth of the neck region, but fails to induce shrinkage (Figure 2.5a). Volume and grain boundary diffusion mechanisms are responsible for the shrinkage, and thus densification of the powdered compact [13, 17]. There is a gross flow of material from the interior of the particle to the neck region; this phenomenon is schematically represented in Figure 2.5b.

Different models attempt to differentiate VD and GD during sintering by monitoring the rate of change in linear dimensions. It should be noted that SD, VD, and GD contribute towards decreasing the surface energy, G_γ, of the compact due to the decrease in surface area. However, only VD and

GD result in shrinkage and densification.

2.3.3 Analytical models

Several approaches have been considered for studying the densification behavior of a material during sintering. Rahaman [34] has classified these models into different categories based on the methods that were adopted for explaining the sintering mechanisms. A description of the technique used in each of the models is presented in Table 2.1 along with some of their drawbacks.

Table 2.1: Theoretical models adopted for studying sintering phenomena.

Models	**Template**	**Drawbacks**
Scaling laws	An effect of change in scale on the rate of single mechanism is modeled.	A qualitative understanding of particle size dependence on only one sintering mechanism is obtained.
Analytical models	Oversimplified geometry is assumed. Analytical equations are derived for each single mechanism.	Provides a significant advance in qualitative understanding of sintering.
Numerical simulations	Numerical solutions are used for quantifying neck geometry.	Results are complex: a powerful computing method is required.
Phenomenological equations	Models are derived based on phenomenological or empirical data.	Sintering diagrams are sensitive to small changes in material parameters. Enormous amount of work is required to make one diagram.

Of all the methods mentioned above, analytical models are the most widely adopted for studying sintering behavior of a powdered compact [13]. These analytical models classify sintering into different geometric stages. A schematic of the three different stages is shown in Figure 2.6. The first stage is defined as a development of weak cohesive bonds between different particle contacts due to green pellet fabrication (point contact, see Figure 2.6a) [13, 34]. The initial stage is considered to be the onset of sintering and is a stage where rapid growth of inter-particle necks occurs (initial state, see Figure 2.6b).

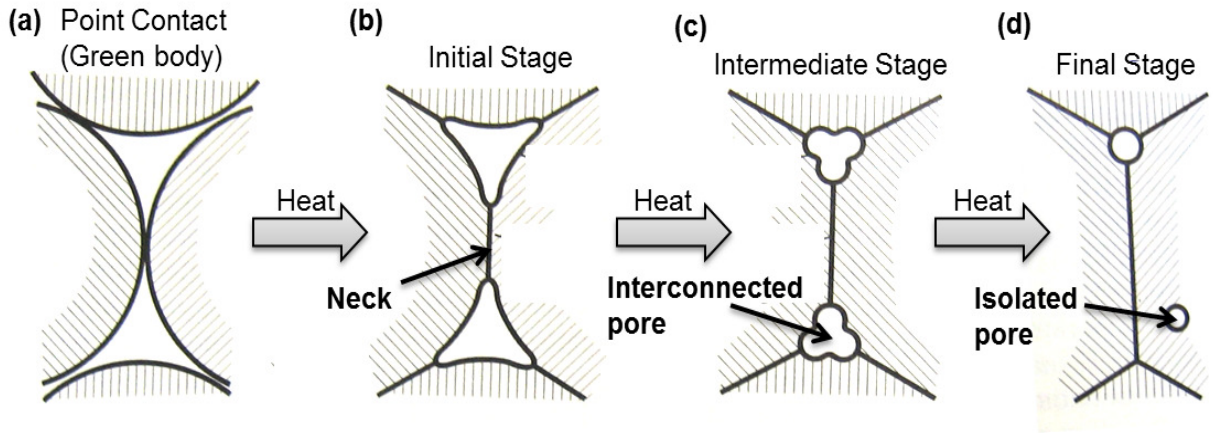

Figure 2.6: Schematic of different stages observed during sintering [13] (used under fair use guidelines, 2011).

During the intermediate stage, there is a simultaneous development of inter-connected pores that form a chain of networks (intermediate state, see Figure 2.6c). The lengths of these interconnects are long when compared to the diameter of the pores. Due to the high aspect ratio of interconnects, the long individual pores break up space into isolated pores. The initialization of these isolated pores indicates the final stage of sintering. (final stage, see Figure 2.6d).

Some of the fundamentals necessary for understanding the basic solid-state diffusion phenomena are presented in the next section. This is essential in understanding the macro-scale sintering phenomena which consists of different micro-scale events that occur at an atomic level [13].

2.3.4 Solid-state diffusion fundamentals

It was Fick who stated that the flux (quantity of material moving a unit area per unit time) of a diffusing species is proportional to the gradients in concentration. Equation 2.1 is known as Fick's first law for the case of diffusion occurring along one direction [17].

$$J = -D\frac{dc}{dx} \tag{2.1}$$

where, J is the flux of the diffusing species ($\frac{mol}{s.cm^2}$), D is the diffusion coefficient ($\frac{cm^2}{s}$), c is the concentration per unit volume ($\frac{mol}{cm^3}$) of the diffusing species, and x is the direction of diffusion.

Fick's first law is based on the empirical observations that only consider the possibility of matter transport due to the gradients in concentration [34]. However, this is only a special case for matter transport. Einstein suggests that the matter transport could be a result of gradients in free energy per mole [17] and Fick's first law has been modified, as shown in Equation 2.2.

$$J = -\frac{Dc}{RT}\frac{d\mu}{dx} \tag{2.2}$$

where, μ is the chemical potential, which is the free energy per mole of a diffusing species

($\frac{J}{mole}$), R is the universal gas constant, and T is the temperature.

The flux of the diffusing species, J, is equivalent to the product of the transport coefficient, $\frac{Dc}{RT}$, and the driving force, $\frac{d\mu}{dx}$ (as shown in Equation 2.2). From a sintering standpoint, the driving force is a reduction in surface area and is given by Equation 2.3.

$$\frac{d\mu}{dx} = \frac{\gamma_{sv}}{n}\frac{dA}{dx} \tag{2.3}$$

where, $\frac{\gamma_{sv}}{n}$ is the surface free energy per mole, dA is the change in the surface area and dx is the change in the radius of neck region (see Figure 2.3).

2.3.5 General theory of reaction rate

The general theory of reaction rate is used for developing a basic understanding of Equation 2.2 that accounts for matter transport, J, due to diffusion, D, and driving force, $\frac{d\mu}{dx}$ [17]. From an elementary viewpoint, a certain amount of energy is required for an atom to diffuse/move from its position to a neighboring position [36]. As the region between the jumps is not as favorable as either its beginning or end position, the atom has to pass through a region of high energy (illustrated in Figure 2.7) [17].

If a plot of the potential energy vs. position for an atomic jump is drawn, a minimum value occurs at the starting and ending positions, and the path between these two sites is a region with maximum energy, $\Delta G^{\dagger}$ (Figure 2.7a). The basis for reaction rate studies is that, even though the lifetime of the activated state (position A, Figure 2.7a) is short, it is treated as an equilibrium

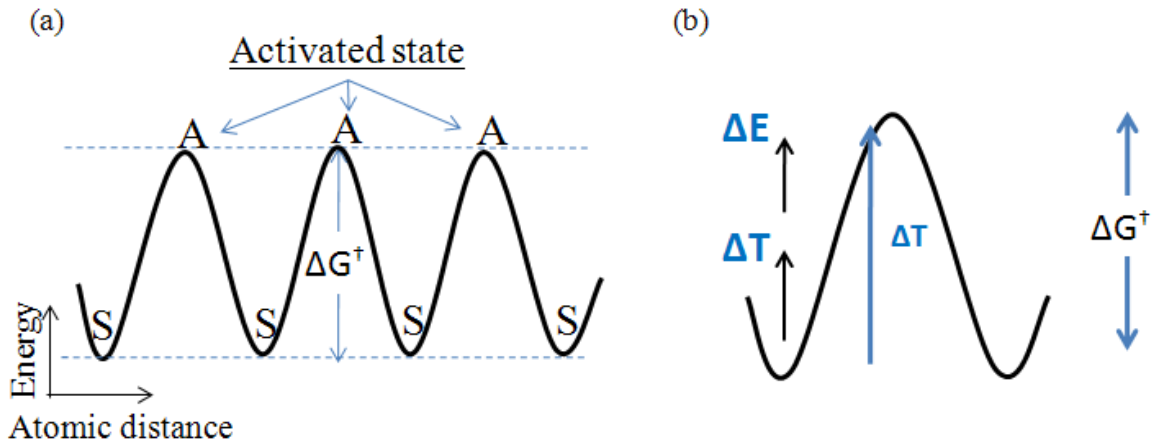

Figure 2.7: Schematic sketch of (a) energy barrier diagrams in a regular crystal lattice, and (b) superposition of the supplied energy and the energy barrier diagram.

process with stable state (position S, Figure 2.7a). Kingery [17] considers this idea to create an equilibrium constant, K, that is related to the free energy of formation, $\Delta G^{\dagger}$, of the activated state by $-kT\,lnK$.

Thermal energy is the most common form of energy supplied to a system. There can also be a situation where at low thermal energies, an external energy source ΔE can supply the additional energy to the atom (Figure 2.7b) for overcoming the activation energy barrier. When the supplied thermal energy, ΔT, is high enough, the atom will overcome the activation energy barrier (shown in Figure 2.7b). In this situation, the likelihood of a forward jump is equal to that of a backward jump, resulting in a net zero flux. That is, simply raising the temperature does not result in a net flux when there is no driving force. The absence of a driving force $(\frac{d\mu}{dx} = 0)$ will result in the probability of a forward $(\mathbf{k_f})$ and the backward jump $(\mathbf{k_b})$ to be equivalent to the reaction rate

constant (**k**) [17]. This is given by the Equation 2.4.

$$\mathbf{k} = \mathbf{k_f} = \mathbf{k_b} = \nu K = \nu \exp\left(-\frac{\Delta G^{\dagger}}{kT}\right) \tag{2.4}$$

where, ν is the attempt frequency of the atom, which for solids is about 10^{13}. The presence of a driving force, $\frac{d\mu}{dx}$, during diffusion would preferentially provide energies along one direction, resulting in a gradient in the supplied energy field, $\frac{d\mu}{dx} \neq 0$ (see Figure 2.8a). Figure 2.8 shows a schematic of this situation by overlaying the supplied energy field with the energy barrier diagram.

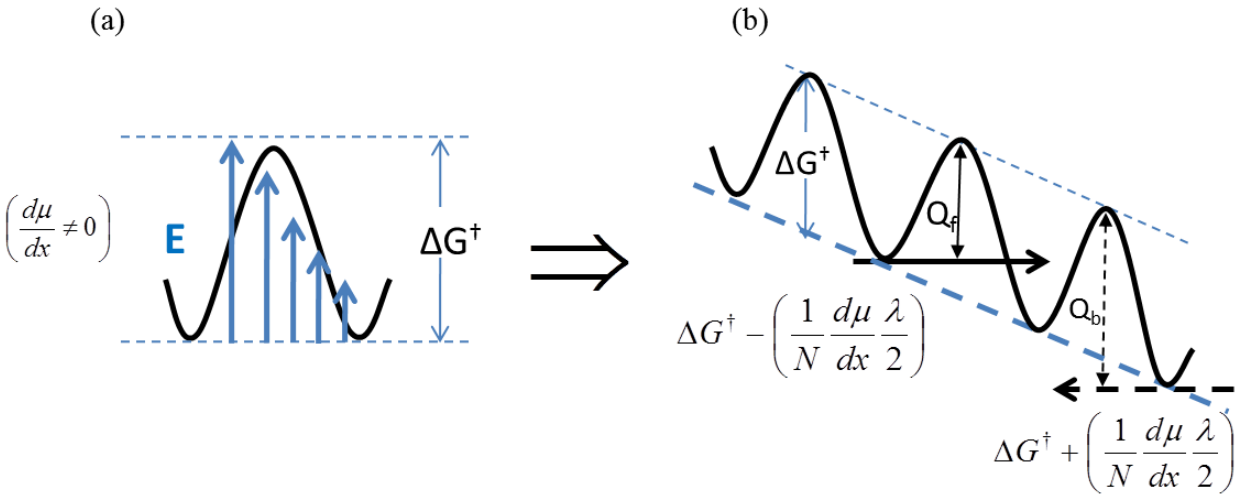

Figure 2.8: Schematic of (a) the preferential energy field (due to driving force) overlaid onto the energy barrier diagram, and (b) resultant change in the apparent energy barrier diagram.

It can be observed from Figure 2.8a, that more energy is available for a forward jump than for a backward jump. In other terms, it is easier for the atoms to jump in the direction of the driving force than against it.

The chemical potential gradients, $\frac{d\mu}{dx}$, can arise due to the differences in concentration, $\frac{dc}{dx}$, (Fick's first law, see Equation 2.1). Interdiffusion between two specimens (along the interface) in a binary alloy diffusion couple is due to the difference in concentration gradients of the diffusing species along the interface (see Figure 2.19). Also, gradients in temperature, $\frac{dT}{dx}$ can create chemical potential differences leading to diffusion (relevant units are presented in Table C.1). This is seen in a binary solution where under a thermal gradient one component diffuses preferentially to the hotter end while the other component diffuses to the colder end. Similarly, sintering phenomena is a result of a decrease in surface free energy for a system of particles. In these situations the probability of atoms jumping towards the direction of driving force will be higher than the probability of atoms jumping against it and this would result in matter flux.

The result of a driving force will *apparently change the energy barrier diagram*, as shown in Figure 2.8b resulting in a preferential jump towards one direction (assuming it is forward). It should be noted that the activation energy $\Delta G^{\dagger}$ is not altered, but the measured activation energy for a forward jump Q_f, is much smaller than for a backward jump, Q_b (see Figure 2.8b). This situation would favor the probabability of forward jumps rather than backward jumps; therefore, $\mathbf{k_f}$ (Equation 2.5) is not equal to $\mathbf{k_b}$ (Equation 2.6) [17].

$$\mathbf{k_f} = \nu \exp\left(- \frac{\Delta G^{\dagger} - \frac{1}{N}\frac{d\mu}{dx}\frac{\lambda}{2}}{kT} \right) \tag{2.5}$$

$$\mathbf{k_b} = \nu \exp\left(- \frac{\Delta G^{\dagger} + \frac{1}{N}\frac{d\mu}{dx}\frac{\lambda}{2}}{kT} \right) \tag{2.6}$$

where, λ is the inter-atomic distance and N is the Avogadro's number.

The net movement of atoms is now given by Equation 2.7, which is the difference between forward and backward movements.

$$\mathbf{k_{net}} = \mathbf{k_f} - \mathbf{k_b} \tag{2.7}$$

$$= \nu \exp\left(- \frac{\Delta G^{\dagger} - \frac{1}{N}\frac{d\mu}{dx}\frac{\lambda}{2}}{kT} \right) - \nu \exp\left(- \frac{\Delta G^{\dagger} + \frac{1}{N}\frac{d\mu}{dx}\frac{\lambda}{2}}{kT} \right) \tag{2.8}$$

$$= 2\nu \exp\left(- \frac{\Delta G^{\dagger}}{kT} \right) \sinh\left[\frac{1}{RT}\frac{d\mu}{dx}\frac{\lambda}{2} \right] \tag{2.9}$$

Expanding the hyperbolic sine function in Equation 2.9, and considering the first order terms, results in Equation 2.10.

$$\mathbf{k_{net}} \approx \frac{\nu\lambda}{RT} \exp\left(- \frac{\Delta G^{\dagger}}{kT} \right) \frac{d\mu}{dx} \tag{2.10}$$

The product of inter-atomic distance, λ, reaction rate constant, $\mathbf{k_{net}}$, and concentration, c, results in flux, J and this is shown in Equation 2.11.

$$J\left(\frac{g}{s \cdot cm^2} \right) = -\lambda\left(cm\right) \cdot \mathbf{k_{net}} \left(\frac{1}{s} \right) \cdot c\left(\frac{g}{cm^3} \right) \tag{2.11}$$

Substituting Equation 2.10 in Equation 2.11 will result in Equation 2.12. This equation represents

the flux (matter transport) due to a driving force, $\frac{d\mu}{dx}$.

$$J = -\left[\frac{\nu\lambda^2 c}{RT}\exp\left(-\frac{\Delta G^{\dagger}}{kT}\right)\right] \times \left[\frac{d\mu}{dx}\right] \tag{2.12}$$

$$[\text{Flux}] = -[\textit{Transport coefficient}] \times [\textit{Driving force}] \tag{2.13}$$

$$J = -\left[D\right]\frac{c}{RT} \times \left[\frac{d\mu}{dx}\right] \tag{2.2}$$

Equation 2.12 is the basic equation for mass transport phenomena. Equation 2.13 represents flux as a product of (1) a transport coefficient, that involves the diffusion coefficient and an activation energy for diffusion, and (2) a driving force. Comparing Equation 2.12 with Equation 2.2 one can observe the diffusion term, D, as related to the fundamental parameters necessary for an atomic jump. This relationship is shown in the following equation.

$$D = \nu\lambda^2 \exp\left(-\frac{\Delta G^{\dagger}}{kT}\right) \tag{2.14}$$

2.3.6 Sintering phenomena in ceramics

In ceramics the matter transport takes place through diffusion of ions (cation and anion). The overall transfer of material is due to a net flux of each component. Even though the rate of diffusion of each type of ion is different the overall flux will take place in such a way that the stoichiometry, and electro-neutrality of the material is preserved. Based on Equation 2.2 the flux of anions and cations can be represented as, Equation 2.15 and 2.16, the subscripts C and A are used to show a

distinction between cation and anion.

$$J = -\left[\frac{Dc}{RT}\right] \times \left[\frac{d\mu}{dx}\right] \tag{2.2}$$

$$J_C = -\left[\frac{D_C c_C}{RT}\right] \times \left[\frac{d\mu}{dx}\right]_C \tag{2.15}$$

$$J_A = -\left[\frac{D_A c_A}{RT}\right] \times \left[\frac{d\mu}{dx}\right]_A \tag{2.16}$$

During the sintering of an ionic compound, $C_\alpha A_\beta$, the material transport takes place by the diffusion of each of the ionic species, $C^{\beta+}$ and $A^{\alpha-}$ (governed by Equation 2.15 and 2.16). The flux equation for the lattice molecule $C_\alpha A_\beta$ can be derived by combining the flux and concentration constraints (shown in Equation 2.17 and 2.18) with the general relationship existing between the chemical potential gradients (see Equation 2.19) [33].

$$J_{C_\alpha A_\beta} = \frac{1}{\alpha} J_C = \frac{1}{\beta} J_A \tag{2.17}$$

$$c_{C_\alpha A_\beta} = \frac{1}{\alpha} c_A = \frac{1}{\beta} c_C \tag{2.18}$$

$$\left[\frac{d\mu}{dx}\right]_{C_\alpha A_\beta} = \alpha \left[\frac{d\mu}{dx}\right]_C + \beta \left[\frac{d\mu}{dx}\right]_A \tag{2.19}$$

Substituting Equation 2.15 and 2.16 in the above equation will result in

$$\left[\frac{d\mu}{dx}\right]_{C_\alpha A_\beta} = \alpha\, J_C \left[-\frac{RT}{c_C\, D_C}\right] + \beta\, J_A \left[-\frac{RT}{c_A\, D_A}\right] \tag{2.20}$$

Replacing the flux and concentration terms (Equation 2.17 and 2.18) in the above equation will result in

$$\left[\frac{d\mu}{dx}\right]_{C_\alpha A_\beta} = \alpha^2 J_{C_\alpha A_\beta}\left[-\frac{RT}{\alpha\, c_{C_\alpha A_\beta}\, D_C}\right] + \beta^2 J_{C_\alpha A_\beta}\left[-\frac{RT}{\beta\, c_{C_\alpha A_\beta}\, D_A}\right] \tag{2.21}$$

After rearrangement (shown in Equation 2.22 and 2.23), the equation for $J_{C_\alpha A_\beta}$ is obtained (see Equation 2.24)

$$-\frac{1}{RT}\left[\frac{d\mu}{dx}\right]_{C_\alpha A_\beta} = J_{C_\alpha A_\beta}\left[\frac{\alpha}{c_{C_\alpha A_\beta}\, D_C} + \frac{\beta}{c_{C_\alpha A_\beta}\, D_A}\right] \tag{2.22}$$

$$-\frac{c_{C_\alpha A_\beta}}{RT}\left[\frac{d\mu}{dx}\right]_{C_\alpha A_\beta} = J_{C_\alpha A_\beta}\left[\frac{\alpha}{D_C} + \frac{\beta}{D_A}\right] \tag{2.23}$$

$$J_{C_\alpha A_\beta} = -\frac{c_{C_\alpha A_\beta}}{RT}\left[\frac{D_C\, D_A}{\beta\, D_C + \alpha\, D_A}\right]\left[\frac{d\mu}{dx}\right]_{C_\alpha A_\beta} \tag{2.24}$$

Equation 2.25 represents the flux of the lattice molecule, $C_\alpha A_\beta$, expressed in the form of Equation 2.2, the modified form of Fick's law.

$$J_{C_\alpha A_\beta} = -\frac{\widetilde{D}\, c_{C_\alpha A_\beta}}{RT}\left[\frac{d\mu}{dx}\right]_{C_\alpha A_\beta} \tag{2.25}$$

$$J = -\left[\frac{Dc}{RT}\right] \times \left[\frac{d\mu}{dx}\right] \tag{2.2}$$

In Equation 2.25 the effective diffusion coefficient, $\widetilde{D}$, is given by

$$\widetilde{D} = \left(\frac{D_C\, D_A}{\beta\, D_C + \alpha\, D_A}\right) \tag{2.26}$$

The transport of cations and anions during densification are interrelated. It is useful to consider two limiting cases, assuming only one diffusion path is dominant, either the lattice or the grain boundary diffusion:

For the first condition, cation diffusion is much faster then the anion diffusion i.e.,

$$D_C >> D_A \text{ then } \widetilde{D} \simeq \frac{1}{\alpha} D_A \tag{2.27}$$

For a second situation, the anion diffusion is much faster than cation i.e.,

$$D_A >> D_C \text{ then } \widetilde{D} \simeq \frac{1}{\beta} D_C \tag{2.28}$$

It can be observed from Equations 2.27 and 2.28 that for both of these situations, the slower diffusing species will be controlling the overall sintering rate in ceramics.

2.3.7 The Arrhenius relation and activation energy

The analysis of Equation 2.14 results in a temperature independent term, $\nu\lambda^2$, and temperature dependent term, $\exp\left(-\frac{\Delta G^{\dagger}}{kT}\right)$. The activation energy required for diffusion is often measured experimentally. This is done by monitoring the diffusion of the atomic species with respect to the temperature. When considering the bulk movement of atoms, the energy per particle, k, is

represented as $\frac{R}{N}$; R being the universal gas constant, and N is the Avogadro's number.

$$D = \nu\lambda^2 \exp\left(-\frac{\Delta G^{\dagger}}{\frac{R}{N}T}\right) \tag{2.14}$$

$$\underbrace{lnD}_{y} = -\underbrace{\frac{Q}{R}}_{m} \times \underbrace{\frac{1}{T}}_{x} + \underbrace{lnD_{\circ}}_{constant}; \qquad \text{where } D_{\circ} = \nu\lambda^2 \text{ and } Q = N\,\Delta G^{\dagger} \tag{2.29}$$

The plot of lnD versus T^{-1} gives a straight line with slope being, $\frac{Q}{R}$, and the intercept being $D_{\circ}$ (see Equation 2.29) . Q, is the symbol widely used in literature for representing experimentally determined activation energy. It is evident that Equation 2.29 is in the form of the well known Arrhenius relation.

The Arrhenius method of measuring activation energy is used in situations where one can measure diffusion with respect to the temperature. Most of the sintering experiments usually involve measurement of densities before and after sintering, it is a common practice to express these values relative to their theoretical density (see Equation A.15). It is not always feasible to track the movement of the diffusing species and estimate the diffusivity. Therefore, to determine activation energy for diffusion during a sintering process, two different approaches were developed; they are classified as isothermal and non-isothermal methods [38, 39, 40, 41].

Isothermal method:

Isothermal sintering methods estimate the time required to reach a target density at a specific temperature. The rate of densification is recorded at each individual temperature; a normal tendency is that with increasing temperature the time required for densification decreases.

The densification behaviour is typically monitored using a dilatometer. In the absence of a dilatometer, sintering runs are performed at regular intervals of time and the resulting densities are recorded. Experiments are designed with higher ramp rates (> $20\frac{^{\circ}C}{min}$) to reach the target temperatures as quickly as possible and then to maintain the isothermal conditions. Figure 2.9

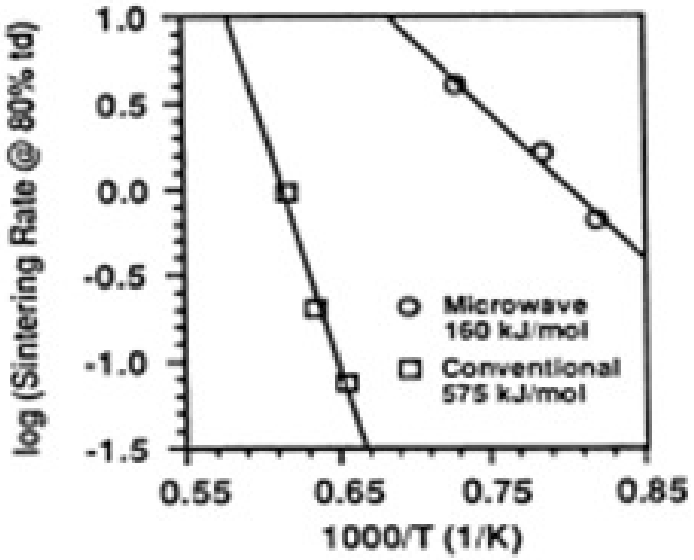

Figure 2.9: Apparent activation energy estimation for sintering of high-purity alumina using two different sintering methods [42] (public domain, work by the U.S government OSTI ID: 5193919).

shows an example of a plot that uses the isothermal sintering method to estimate the activation energy. Three different temperatures were used (in Figure 2.9) to estimate the time required to reach 80% Theoretical Density (TD). It can be observed that, as the temperature increases, the amount of time required to reach 80% TD decreases.

The rate of densification, $\frac{d\rho}{dt}$, for each individual temperature is calculated. The plot of the logarithmic of $\frac{d\rho}{dt}$ and the inverse of temperature will exhibit an Arrhenius (see Equation 2.29) type of behavior (as shown in Figure 2.9). The slope of this plot gives the measured activation energy

for that sintering process. It can be seen from Figure 2.9 that the measured activation energy, Q, for sintering high-purity alumina was 575 $\frac{kJ}{mol}$ for a conventional process and 160 $\frac{kJ}{mol}$ for a microwave process.

The high heating rates adopted for this method will mask some of the changes that occur during the initial stages of sintering. Also, there is a greater chance of developing a large number of stresses due to the presence of higher ramp rates. To avoid these experimental difficulties, a different method was developed based on conducting experiments at a constant heating rate. These techniques are addressed in the following section.

Non-isothermal method:

Non-isothermal sintering methods aim at determining the activation energies by monitoring the sintering behaviour of a material as a function of heating rate. Constant Heating Rate (CHR) and the Master Sintering Curve (MSC) are the two non-isothermal sintering methods that were found in the literature.

Constant Heating Rate Method:

Young and Cutler [41] were the first to apply this method. Figure 2.10 will be used for explaining the CHR technique.

Typically three to four different heating rates are used for this study e.g., 5, 10, 20 $\frac{^{\circ}C}{min}$, since the densification rate is a function of heating rates. The variation in densification rates is monitored with respect to a particular temperature for each given heating rate, resulting in density lines lying parallel to one another (see Figure 2.10) [39, 40]. The slope of these lines multiplied by the

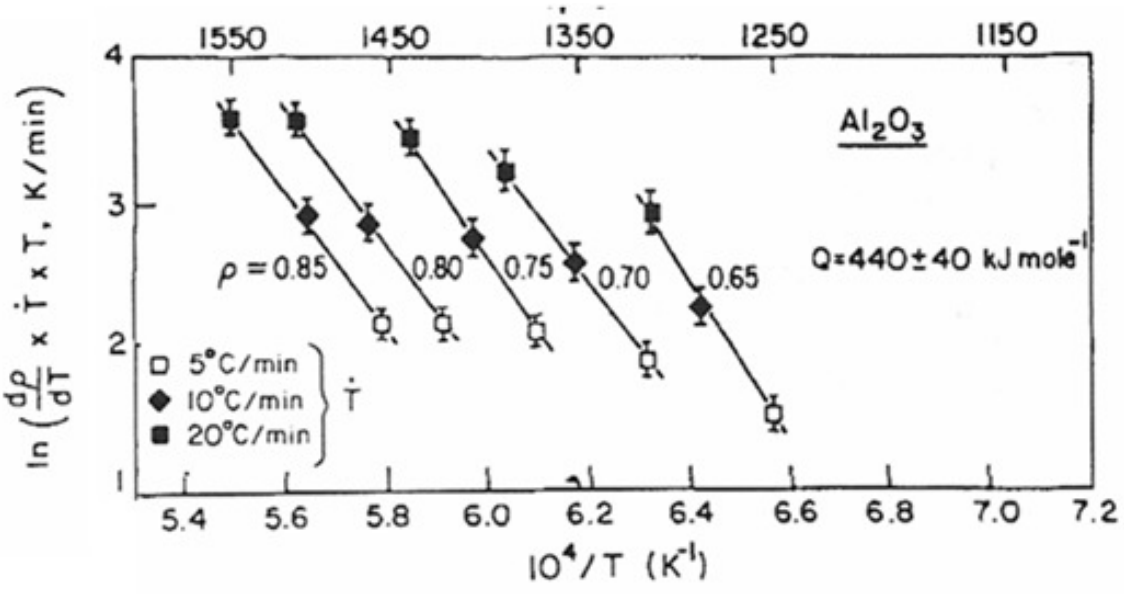

Figure 2.10: Activation energy measurement using the CHR method for alumina [40] (used under fair use guidelines, 2011).

universal gas constant, R, would give the activation energy for diffusion during sintering. A value of 440$\frac{kJ}{mol}$ is recorded from Figure 2.10 for alumina.

Master Sintering Curve Method:

The Master Sintering Curve model is another method of measuring activation energy from sintering studies. This technique was developed by Su and Johnson [38]. The MSC method was developed from a combined stage sintering model that relates the instantaneous linear shrinkage to its process variables *time* and *temperature* [38]. Assuming that during sintering only one diffusion mechanism dominates, the rate of change in linear shrinkage is given by the following equation.

$$-\frac{1}{L_\circ}\frac{dL}{dt} = \left(\frac{\gamma\Omega}{k}\frac{\Gamma_1}{G^3}D_\circ\right)\frac{1}{T}\exp\left(-\frac{Q}{RT}\right) \tag{2.30}$$

where, $L_\circ$ is the initial length of the sample, $\frac{dL}{dt}$ is the rate of change in linear dimension during sintering, γ is the surface energy of the material, Ω is the atomic volume, G is the grain size, $D_\circ$ is the coefficient of diffusion, and Q is the activation energy. Rearranging Equation 2.30 results in the separation of variables that effect the microstructrual properties and process variables such as temperature, T, and time, t; This is shown in Equation 2.31.

$$\underbrace{-\frac{1}{L_\circ}dL\frac{1}{\left(\frac{\gamma\Omega}{k}\frac{\Gamma_1}{G^3}D_\circ\right)}}_{\textit{Microstructural variables}} = \underbrace{\frac{1}{T}\exp\left(-\frac{Q}{RT}\right)dt}_{\textit{Process variables}} \tag{2.31}$$

The equality between process variables and the resulting densification is defined as a *master sintering curve*. A series of sintering experiments at different heating rates is required for estimating Q.

Figure 2.11 is a schematic between densification (equivalent to the left-hand term in Equation 2.31) and process variables (right-hand term in Equation 2.31) for different heating rates.

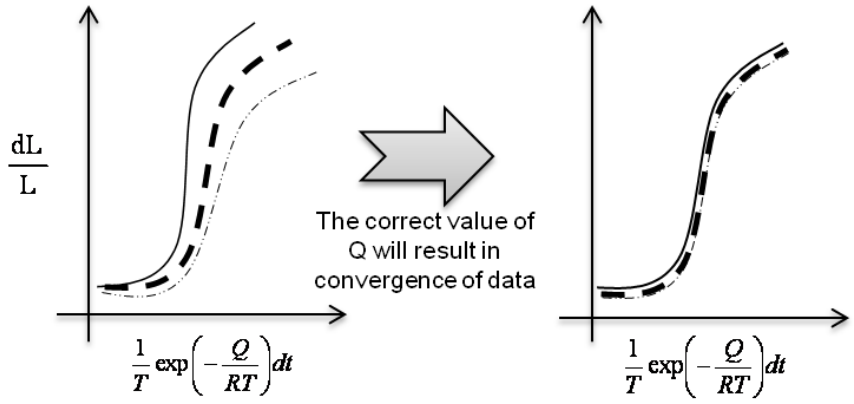

Figure 2.11: Estimation of apparent activation energy from a master sintering curve.

The right hand term of the Equation 2.31 is experimentally determined and is plotted against the left hand term in the Equation 2.31. The Y-axis in Figure 2.11 is a function of temperature, time and activation energy, Q. Since, Q, is the value to be determined, using the trial and error method MSC curves are plotted at different values of Q. The value of, Q, at which there is a best convergence in densification curves (see Figure 2.11) is considered to be the activation energy for diffusion during sintering.

2.4 Ceramic sintering using microwave energy

Microwaves are electromagnetic waves that lie between radio and infrared frequency regions in the electromagnetic spectrum (see Figure 2.12). While the majority of the microwaves frequencies are dedicated for communications and radar purposes, the following frequencies are designated for industrial, scientific, and medical uses: 915 MHz, 2.45 GHz, 5.8 GHz, and 20.2-21.1 GHz [5, 6].

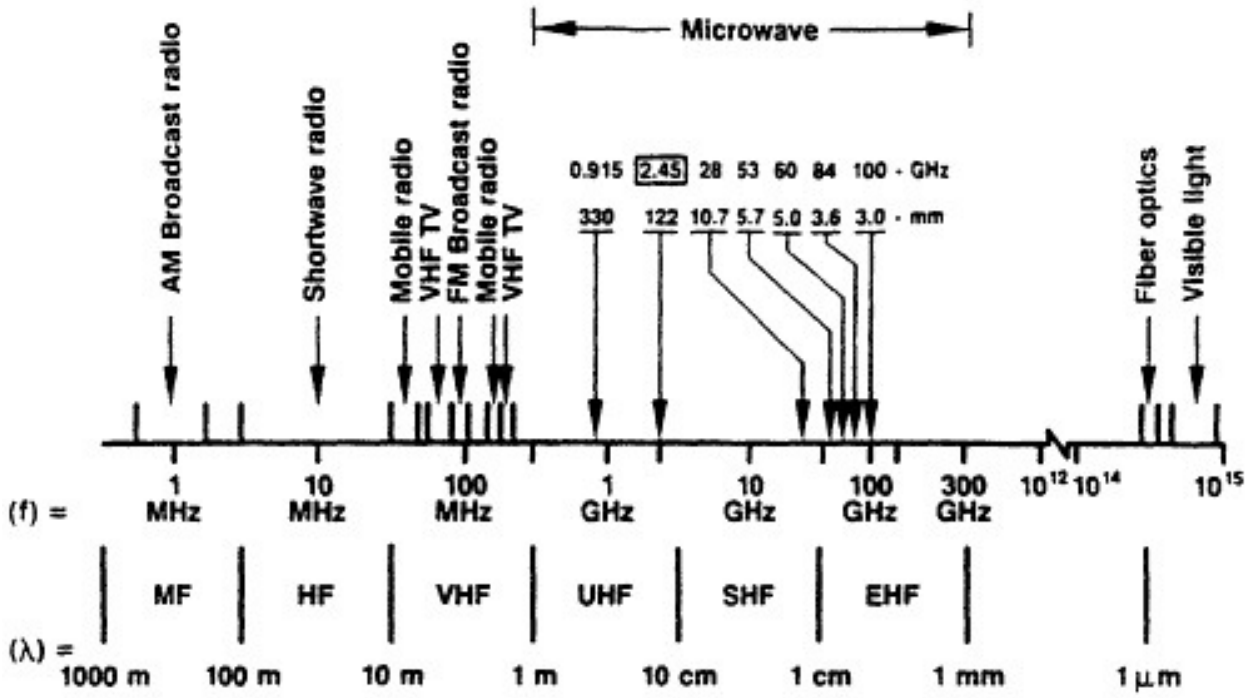

Figure 2.12: Electromagnetic spectrum illustrating specifically the microwave range [43].

Home-model microwave ovens operate at a frequency of 2.45 GHz frequency due to the fact that the water molecules present in food show good microwave absorption at this frequency. The relative availability of 915 MHz and 2.45 GHz microwave ovens resulted in their application to processing ceramics [5].

Microwaves interact with materials in different ways. They are generally reflected, transmitted, or absorbed. The ability of certain materials to convert microwaves into heat makes microwave processing possible [43]. The main difference between a conventional and a microwave process is shown in Figure 2.13.

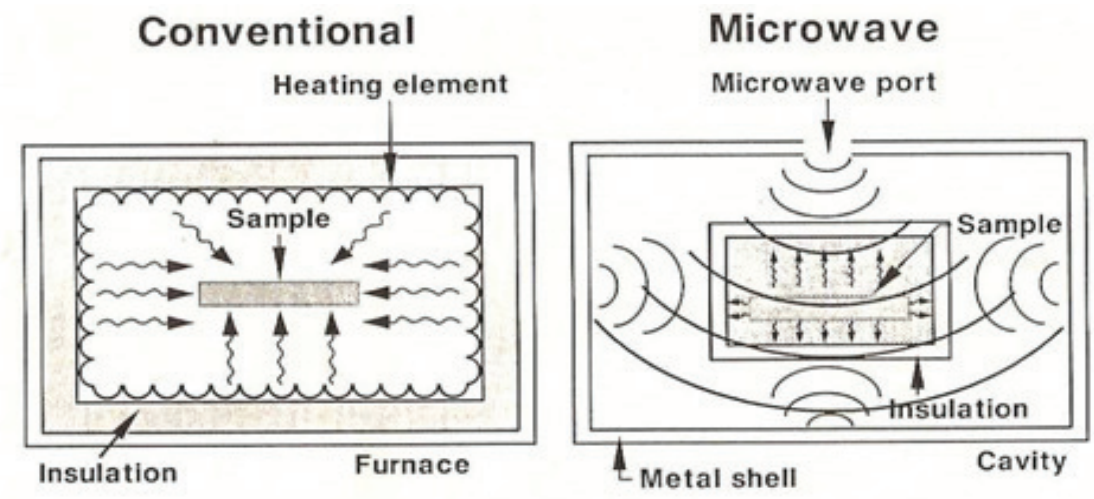

Figure 2.13: Heating patterns in conventional and microwave furnaces [4].

In conventional furnaces, the heating elements supply heat to the sample; the majority of heat is concentrated along the surface of the body when compared with the interior of the sample. In a microwave furnace, the material will absorb microwave energy and will convert it into heat. The heating pattern during microwave processing is more internal in nature.

2.4.1 Historical perspective

The first reported work on sintering ceramics using microwaves dates back to the 1960's with the patent on firing refractories by Levinson [44]. Since then, microwave technology has been

applied to process some of the common ceramics consisting of oxides, borides, carbides, nitrides, and a combination of these materials (see Figure 2.14).

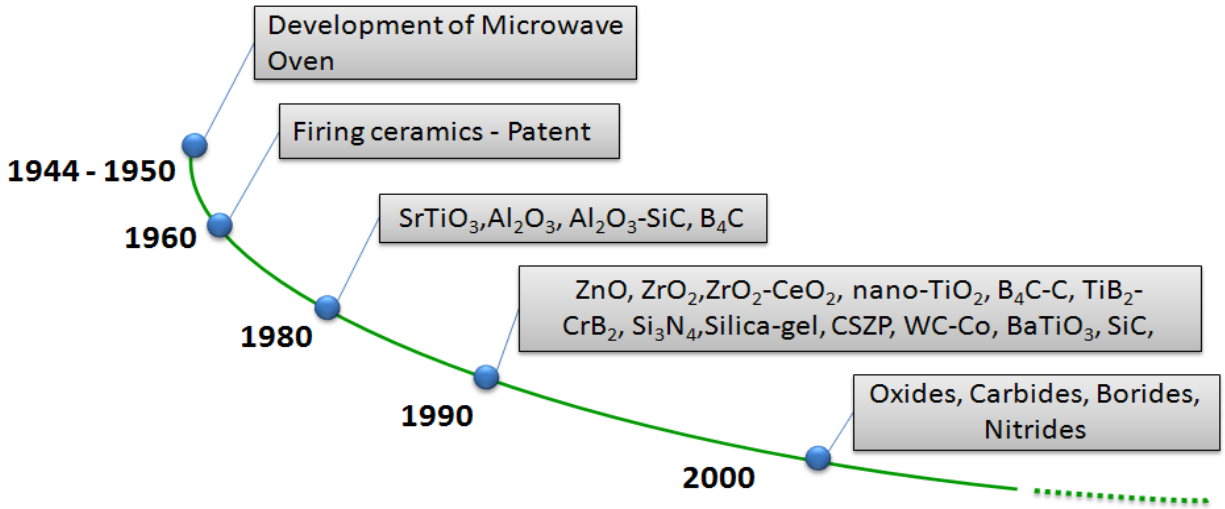

Figure 2.14: Historical perspective of sintering ceramics using microwave energy.

Research on microwave sintering showed promising results for applications that demand rapid sintering at low temperature. Due to these initial observations, numerous studies were initiated that focused on

- application of microwave energy for processing different materials (see Figure 2.14),
- modification of existing microwave equipment to accommodate material processing, and
- understanding the effect of microwaves on materials.

Interest in this area of research resulted in several symposia. Starting in 1988 [45], these symposia were alternated between meetings of the Materials Research Society and the American Ceramic Society. The result of a common interest in microwave processing by various individuals led

to the formation of the Microwave Working Group; this group actively coordinates new symposia with a mission of bringing microwave science from the lab to commercial applications.

2.4.2 Microwave absorption theory

Microwave heating is a phenomena of electromagnetic energy dissipation inside a material [46]. Considering non-magnetic materials, the charges present in the material would respond to the electric field (that is associated with microwave) by the following two processes [5]:

Polarization: short range formation and displacement of dipoles present in the material; quantified as ($\varepsilon_d^{''}$) and

Conduction: long-range displacement of charged particles; quantified as ($\varepsilon_c^{''}$)

The formation and displacement of dipoles is dominant at the microwave frequencies ($2.45\,GHz$). Some of the other types of polarization observed in materials (at different frequencies) include electronic polarization ($\varepsilon_e^{''}$), ionic polarization ($\varepsilon_i^{''}$), and interfacial polarization ($\varepsilon_s^{''}$). Due to the experimental limitation with differentiating each type of polarization, a termed referred to as effective loss, $\varepsilon_{eff}^{''}$, has been introduced [5]. The effective loss factor is equal to the sum of $\varepsilon_e^{''}$, $\varepsilon_i^{''}$, $\varepsilon_s^{''}$, $\varepsilon_d^{''}$, and $\varepsilon_c^{''}$. Microwave heating is mainly due to polarization and ionic conduction. The frequency dependence of each of these processes is presented in Figure 2.15.

Figure 2.15 shows the temperature dependence of $\varepsilon_{eff}^{''}$ with frequency. It can be observed that the ionic conduction losses decrease with an increase in frequency. This behavior is due to the fact

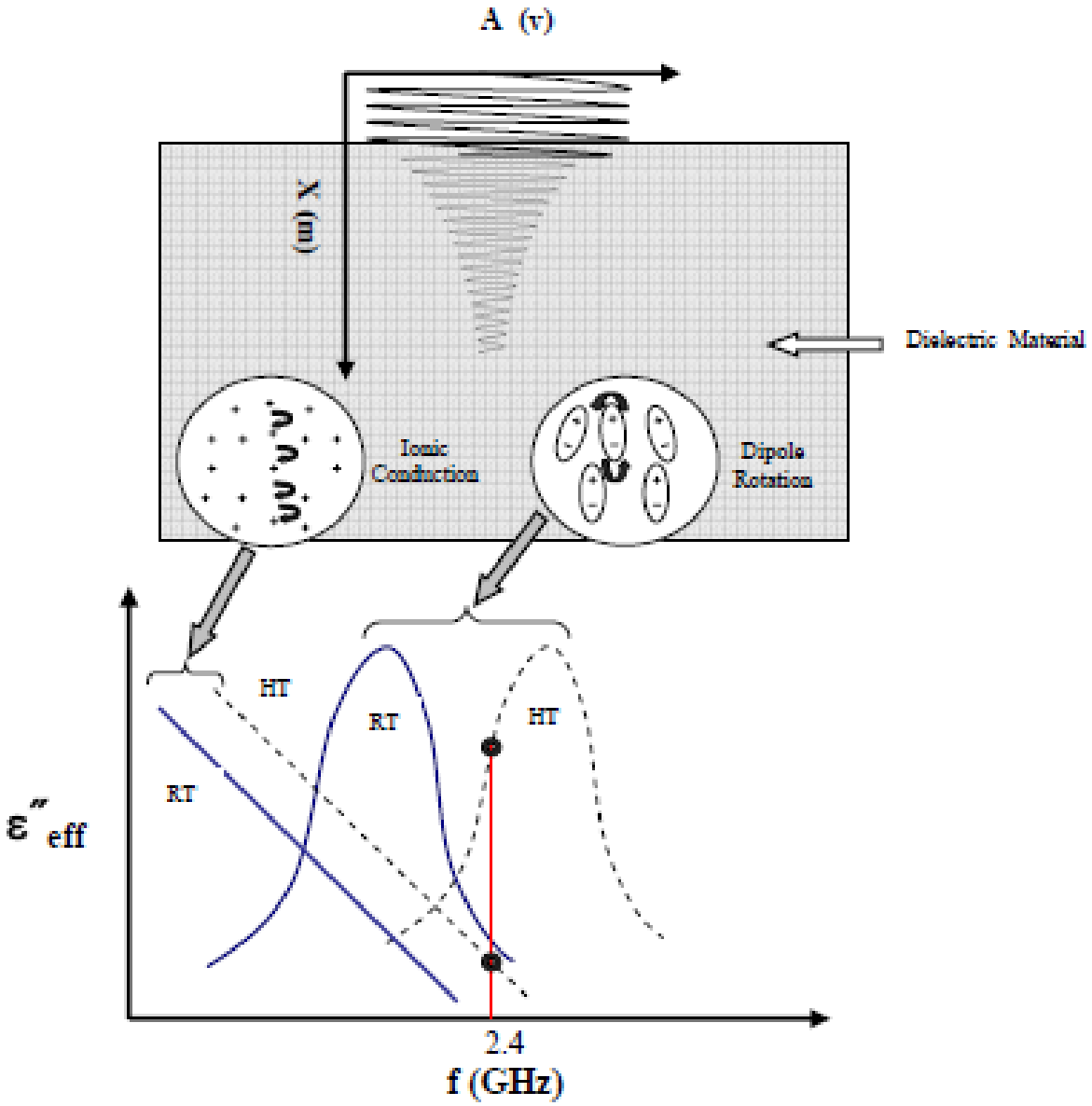

Figure 2.15: Variation of ionic conduction and dipolar rotation with frequency and temperature: $X \equiv$ distance; $A \equiv$ Amplitude of electric field; $\varepsilon''_{eff} \equiv$ effective dielectric loss; $f \equiv$ frequency; $RT \equiv$ room temperature; $HT \equiv$ high temperature: [5] (used under fair use guidelines, 2011).

that as the frequency increases, a greater amount of time is available for the charge to transport in the direction of field. Another observation that is important to microwave processing is the shift in the losses due to dipolar rotation towards microwave frequencies with temperature. This behavior is due to the increase in kinetic energy of molecules with temperature. This phenomenon can lead to unstable accelerated heating often termed as *thermal runaway* [5].

The absorption of microwave energy and conversion to heat is due to polarization and conduction would result in a rise in temperature, $\frac{\Delta T}{\Delta t}$, and this is given by the following equation:

$$\frac{\Delta T}{\Delta t} = \frac{2\pi f \varepsilon_o \varepsilon_{eff}^{''} E_{rms}^2}{\rho c_p} \left(\frac{^\circ C}{s}\right) \tag{2.32}$$

where, ε_o is the permittivity of free space $(8.85 \times 10^{-12}\ \frac{V}{m^3})$, $\varepsilon_{eff}^{''}$ is the relative effective dielectric loss due to ionic conduction and dipolar reorientation, f is the frequency $(\frac{1}{s})$, E_{rms} is the root mean square of the electric field within the material $(\frac{V}{m})$, ρ is the bulk density of dielectric material $(\frac{kg}{m^3})$ and C_p is the heat capacity of the material at constant pressure $(\frac{J}{kg \cdot ^\circ C})$ [46].

The dissipation of microwave power is limited by the attenuation of electromagnetic waves within the material and this is quantified as *depth of penetration*, D_p. It is defined as the distance from the surface of the material at which the power level drops to 37 % and is given by the following equation [46]:

$$D_p = \frac{\lambda}{2\pi\sqrt{2\varepsilon^{'}}} \left[\sqrt{1 + \left(\frac{\varepsilon_{eff}^{''}}{\varepsilon^{'}}\right)^2} - 1\right]^{-\frac{1}{2}} \tag{2.33}$$

where, $\varepsilon^{'}$ is the relative dielectric constant of the material.

For a given microwave frequency, it can be observed from Equation 2.32 that microwave absorption depends on the effective dielectric constant, $\varepsilon^{''}_{eff}$, and the magnitude of the internal electric field, E_{rms}. The higher these values are, the more energy (microwave) that would be absorbed. However, the extent to which microwaves are converted to heat is limited by their depth of penetration. It can be observed from Equation 2.33 that, with the increase in $\varepsilon^{''}_{eff}$, the D_p will decrease i.e., at very high effective dielectric loss values, the microwave heating will focus more along the material's surface similar to that of conventional heating.

Due to wide availability of 2.45 GHz microwave ovens, this frequency is used by many researchers for heating different ceramics [20, 47, 48, 18, 49]. The $\varepsilon^{''}_{eff}$ for most ceramics at room temperature is low ($\varepsilon^{''}_{eff} < 0.08$), which makes microwave heating inefficient [50]. However, at temperatures greater than 400 °C, the $\varepsilon^{''}_{eff}$ are high enough ($\varepsilon^{''}_{eff} > 1$) for microwave heating to be possible [50].

2.4.3 Microwave heating techniques

Microwave-assisted heating

Microwave-assisted heating techniques were developed to process ceramics with very low $\varepsilon^{''}_{eff}$ values. These techniques rely on a susceptor that supply heat to the sample by absorbing microwaves. Susceptors are designed to raise the temperature of a sample high enough that the material starts to absorb microwaves and heat by itself, independent of the suscepting material [43]. In

these situations, the sample would experience a combination of both conventional heating (during the initial stages) and microwave heating (at the later stage). There is a large body of literature that focuses on engineering suceptors for sintering; some of the most commonly used susceptors are outlined in Table 2.2.

Table 2.2: Susceptors for microwave-assisted heating.

Author	Susceptor	Materials system
Dé [47]	SiC based Al_2O_3 composite	Al_2O_3
Samuels et al [49]	ZrO_2 fiber boards	ZrO_2
Janney et al [20]	Pure - SiC rods	8 mol % Y_2O_3 - ZrO_2
Goldstein et al [48]	SiC grit layer	$MgAl_2O_4$
Moore [51]	SiC based Al_2O_3 composite	Al_2O_3
Brosnan et al [18]	SiC based Al_2O_3 crucible	Al_2O_3

One of the disadvantages with using these suceptors is that there is a limited control over the amount of conventional heat (radiant) supplied to the sample. Wroe and Rowley [22] have come up with a new design for microwave-assisted heating. They modified a microwave cavity to incorporate heating elements that have an independent power supply. This set-up essentially regulates the amount of conventional heat required for raising the temperature of the sample.

Direct microwave heating

Most of the published studies on microwave sintering have used microwave-assisted heating; only a few studies [52, 53] have focused on studying the effects of direct microwave heating on sintering. Direct microwave heating is solely due to the interaction between microwave energy

and the sample [52, 43]. The absence of a susceptor during microwave sintering (1) minimizes the perturbation of the electromagnetic field distribution in the cavity, (2) eliminates the presence of additional heating sources external to the sample, and (3) may potentially enhance the overall sintering behavior.

According to Equation 2.32, the rise in temperature for a given material is directly proportional to the frequency, f, ε''_{eff}, and E_{rms}. For a given frequency, direct microwave heating relies on increasing the temperature of the sample by increasing the applied electric field. As the temperature of the sample increases, the rise in effective dielectric loss contributes to further heating. For this investigation, the sintering behaviour of 8YZ was examined using both microwave-assisted and direct microwave heating methods.

The following two sections review the prominent results found in literature that show a difference between microwave and conventional sintering.

2.4.4 Review of microwave sintering

For many ceramic materials, microwave heating has been shown to accelerate the sintering process when compared to conventional methods. This technology has been investigated for applications that focused on

1. lowering the thermal expansion mismatch stresses among various materials while fabricating a multi-component system [20].

2. suppressing the problem associated with grain growth at high temperatures [54].

3. reducing the energy consumption to lower the overall manufacturing costs [55, 51].

Janney et al [20] adopted microwave sintering for processing fully stabilized zirconia. It was reported (see Figure 2.16) that the densification behavior of ZrO_2 (8 mol % Y_2O_3) was different in a microwave furnace and a conventional furnace. It can be observed from Figure 2.16 that microwave sintering shifted the density curves by ∼100-150 °C towards lower temperature, as compared to conventional sintering.

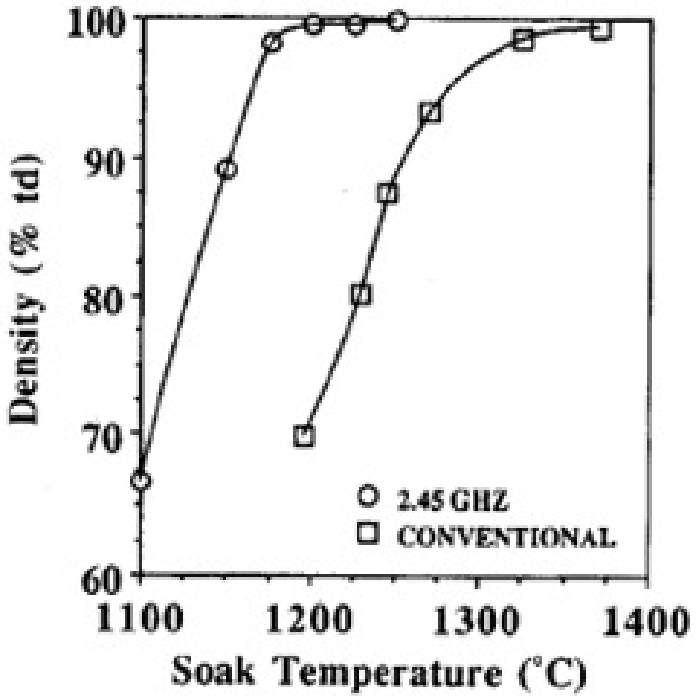

Figure 2.16: Microwave firing accelerated the densification of ZrO_2 (8 mol % Y_2O_3) as compared to that for conventional firing [20] (used under fair use guidelines, 2011).

Cheng et al [54] have applied microwaves for sintering tungsten carbide, a cutting tool material. The idea here was to mitigate the problem of grain growth normally associated with high-temperature conventional processing. It was reported that microwave heating could sinter WC-Co

tool bits with better properties. Table 2.3 a comparison between a microwave, and a conventionally processed WC/Co cermets.

Table 2.3: Comparison of microwave and conventional processes for sintering WC-Co composite [54].

	Microwave	**Conventional**
Sintering temperature (°C)	1300	1450
Total cycle time	90 min	12-24 h
Sintering time (min)	10	60
Density (% T.D.)	99.8	99.7
Average grain size (μm)	0.6	2
Bending strength (MPa)	1800	1700
Hardness (Rockwell A)	93	91

Table 2.3 shows that microwave sintering resulted in fine microstructures (0.6 $vs.$ 2 μm) in about one-tenth the cycle time required for conventional sintering. This trend also implies that microwave sintering may eliminate the need for the addition of grain growth inhibiters, such as TiC, TaC, and VC.

Dé's [47] investigation on ultra-rapid hybrid microwave sintering of alumina showed accelerated densification (as compared with conventional sintering). For this study, the variation in properties such as porosity, grain sizes, hardness, and fracture toughness were examined along the cross-section of a sample (see Figure 2.17a) .

Figure 2.17b shows the heating profile (30 min hold time at 1500 °C) adopted for sintering. Microwave-sintered samples showed higher density (96 % vs. 87 %theoretical density) when com-

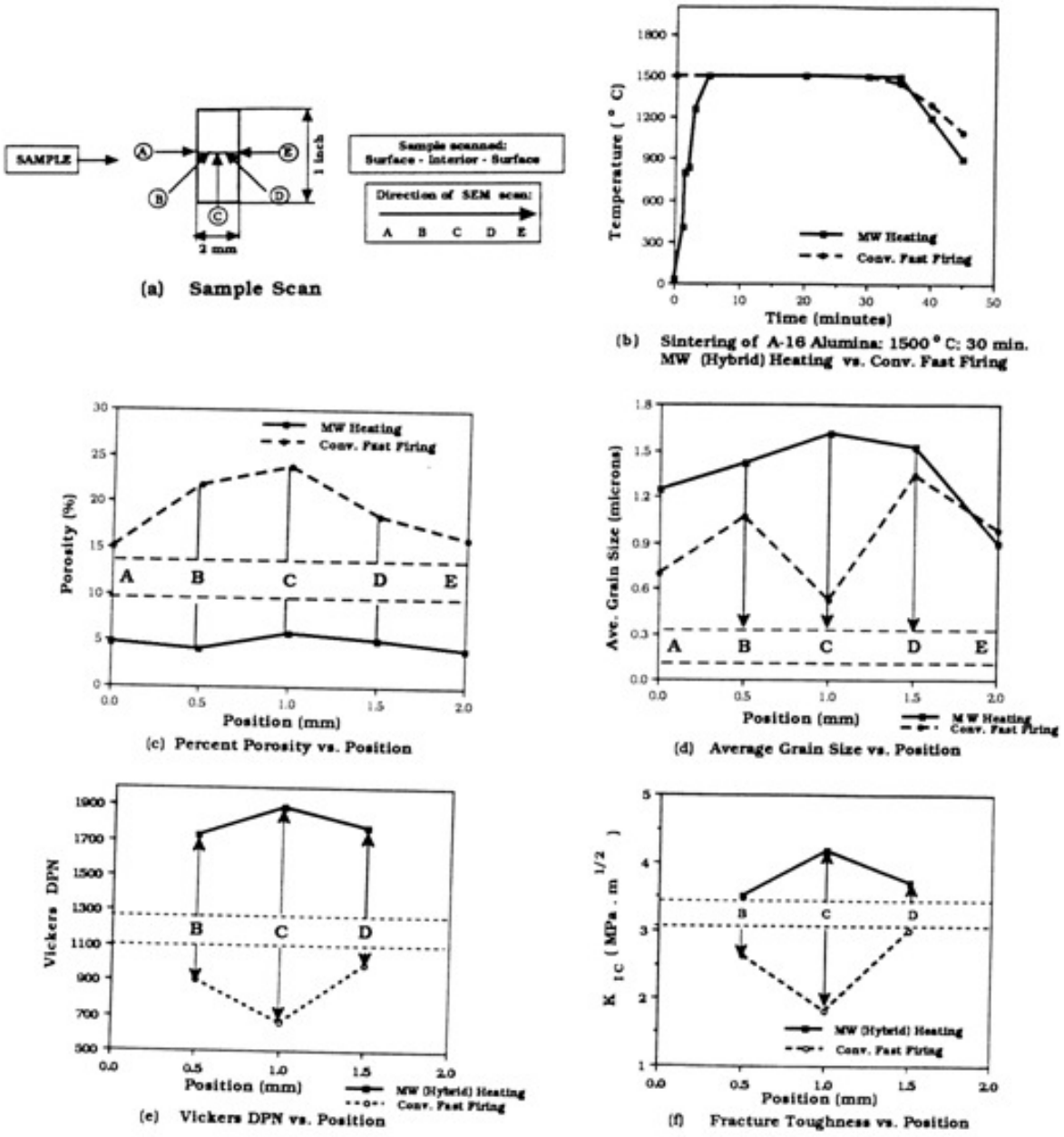

Figure 2.17: Fast firing of alumina: microwave (hybrid) heating vs. conventional fast firing [47] (used under fair use guidelines, 2011).

pared with conventionally sintered samples. Figure 2.17c shows that there was a greater variation in porosity across the cross-section of a conventionally sintered sample than a microwave-sintered sample. Figure 2.17d, 2.17e, and 2.17f show that both microwave and conventional sintering had differences in property between surface of the sample and it's interior.

Microwave-sintered samples exhibited higher hardness and fracture toughness (see Figure 2.17e and 2.17f) values at the center of the sample. These observation indicate that the interior of the sample experienced better sintering with microwave heating. This improvement is due to the difference in heating patterns between a conventional and a microwave furnaces (see Figure 2.13) [4].

Sherritt Inc. [56] evaluated the energy consumption for scaling up the sintering process for manufacturing cutting tools (Si_3N_4) using microwave energy. The energy requirements for microwave sintering was found to be one-tenth that of a conventional process. In addition to the energy savings, the resulting product exhibited finer grain size along with a greater uniformity in structure. Similar observations were made by Bronsan et al [18] and Moore [51] while investigating the possibility of minimizing the production costs for mass manufacturing of armor plates.

Wroe and Rowley [22] developed a hybrid furnace with the ability to shift between two heating sources (microwave and conventional). In addition, a dilatometer was attached to this furnace to record the in situ shrinkage of the sample during sintering. This set-up was used to study the effect of microwave-assisted sintering on partially stabilized zirconia. Figure 2.18 is a normalized linear shrinkage plot as a function of temperature.

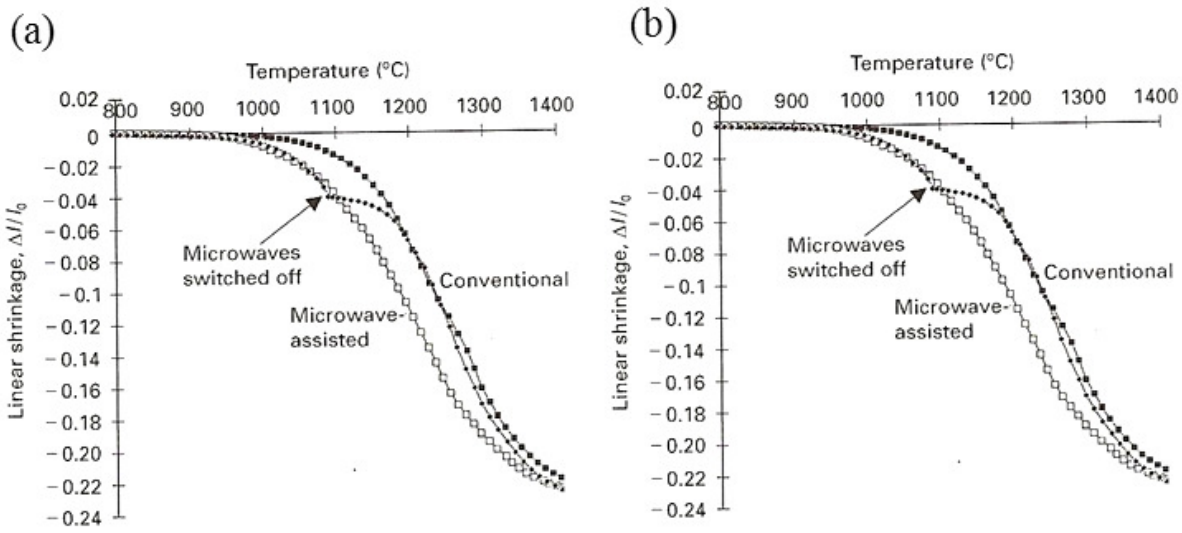

Figure 2.18: Normalized linear shrinkage of zirconia plotted as a function of temperature for (a) conventional and microwave-assisted sintering (b) different microwave powers [22] (used under fair use guidelines, 2011).

The data presented in Figure 2.18a shows a shift in the shrinkage curve by ∼80 °C for microwave sintering when compared with conventional sintering. It can also be observed (Figure 2.18a) that by switching the microwave source to a conventional heating source (at ∼1080 °C), the sintering slowed down until it reached a high enough temperature for it to continue further shrinkage. It was also reported that with the increase in microwave power (see Figure 2.18b) the densification curves shifted towards lower temperatures.

Solid-state sintering occurs through a mixture of volume, surface, and grain boundary diffusion (see Section 2.3.2) [34]. The phenomenological observations (presented above) are an indirect indication to the fact that microwaves are enhancing matter transport. Some of the studies in the literature provide clear evidence by directly measuring diffusion (of ions) during microwave heating; the following section summarizes these reports.

2.4.5 Microwave enhanced diffusion

Diffusion in crystalline regions

Annealing studies were performed by Ahmad [57] on a diffusion couple consisting of zinc oxide and single-crystal alumina. Diffusion studies in single crystals are preferred to eliminate any of the effects coming from grain boundaries (present in polycrystals). The annealing was performed at 1100 °C inside conventional and microwave furnaces for a period of 3 h. The elemental mapping technique (back-scattered electron imaging) was used to track the movement of zinc atoms inside single-crystal alumina. As shown in Figure 2.19, the diffusion barrier of zinc is thicker in microwave-annealed samples than in the conventionally annealed samples.

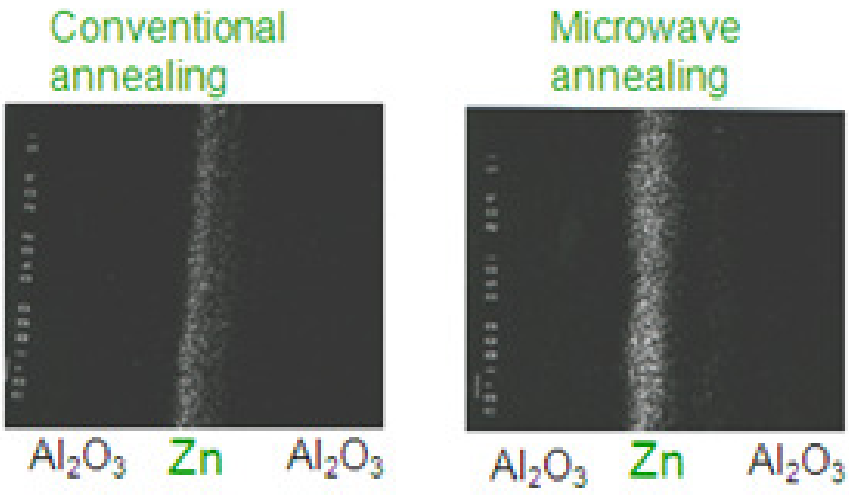

Figure 2.19: Elemental mapping of zinc oxide diffusion in single-crystal alumina [57] (used under fair use guidelines, 2011).

Diffusion in non-crystalline regions

Fathi et al [58] focused on studying the diffusivity of K^+ ion in an amorphous material, sodium-alumino silicate glass. It was observed (see Figure 2.20) that the penetration depth of K^+ ion was

higher for microwave-annealed samples. It was also reported that an increase in the microwave power increased the penetration depth of the ions.

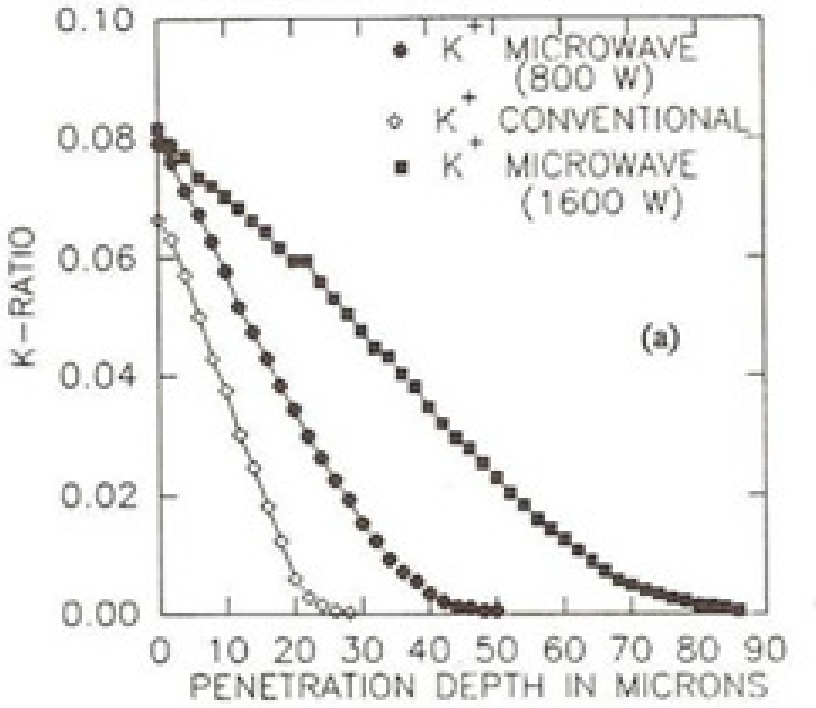

Figure 2.20: Pottassium ion diffusion in sodium-alumino silicate glasses [58] (used under fair use guidelines, 2011).

Meek et al [59] have studied the diffusion of cobalt ions in Pyrex ® glass. A similar observation was made i.e., cobalt-ion diffusion was enhanced due to microwave heating when compared with conventional heating. Figures 2.19 and Figure 2.20 supports the speculation that microwave heating is enhancing the volume diffusion (diffusion along the crystalline regions) and grain boundary diffusion (diffusion along amorphous regions).

Effect of microwave polarization on diffusivity:

Whittaker [60] studied the diffusion behaviour of Y^{+3} in $YBa_2Cu_3O_{7-\delta}$ with respect to the

polarization angle of microwaves during heating. The diffusion species (Y^{+3}) is embedded inside the $YBa_2Cu_3O_{7-\delta}$ matrix. After subjecting the sample to heat treatment, the diffusivity of Y^{+3} ions was monitored across the radial line of the sample. These results are shown in Figure 2.21.

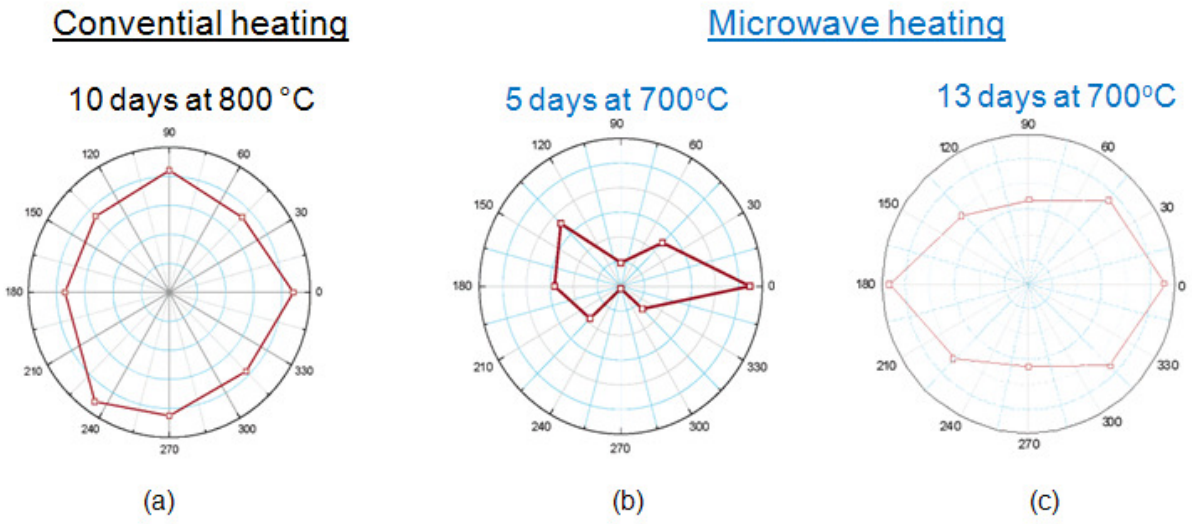

Figure 2.21: Polar plot of the relative diffusion coefficient (radial axis) for Y^{+3} diffusing into $YbBa_2Cu_3O_{7-\delta}$ as a function of angle to microwave polarization: (a) conventional heating; (b) sample heated by microwaves polarized along 0-180° axis [60] (used under fair use guidelines, 2011).

Conventional heat treatment (800 °C for 10 $days$) resulted in isotropic distribution of Y^{+3} ion along the matrix (see Figure 2.21a). A preferred direction for Y^{+3} ion diffusion was observed during microwave heating (700 °C for 5 $days$); shown in Figure 2.21b. With the increase in the soak time to 13 $days$ ($vs.$ 5 $days$), the diffusivity of Y^{+3} ion is equal in all direction. Figures 2.21b and 2.21c show that, during microwave heating, the diffusivity is a function of direction of the electric field (associated with microwaves).

The gradients in concentration of the diffusing species along interface is responsible for diffusion shown in Figures 2.19, 2.20, and 2.21. It can be observed that microwave annealing results

in accelerated diffusion and is also a function of polarity [60].

Rate of diffusivity

Janney et al [61] monitored the rate of diffusivity with respect to temperature for ^{18}O isotope in sapphire during microwave and conventional heating. Figure 2.22 is the logarithm of the diffusivity (of ^{18}O) with respect to temperature.

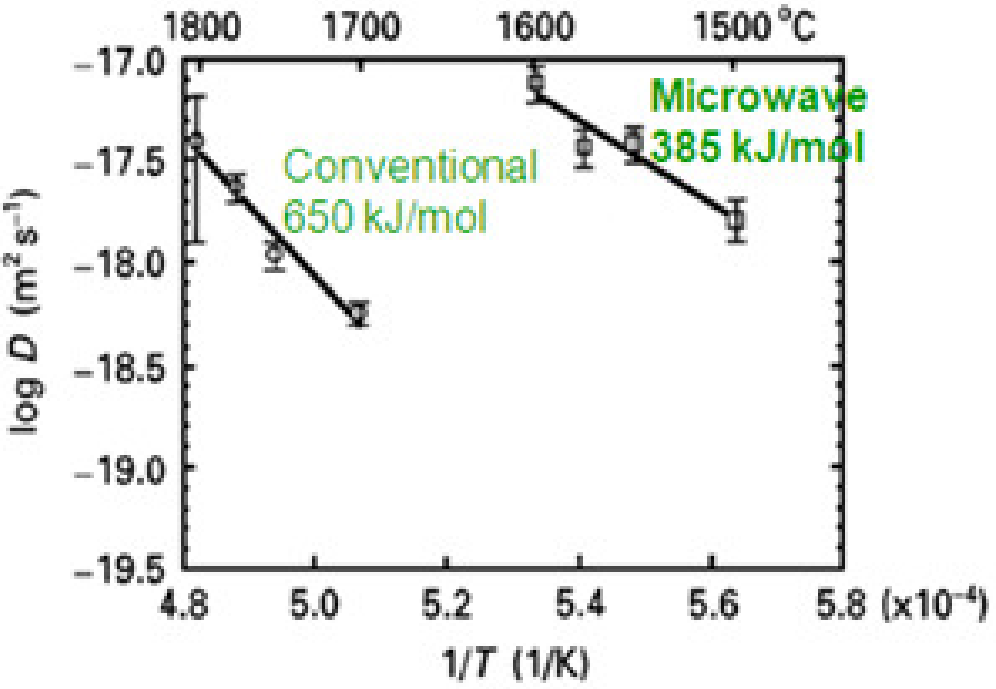

Figure 2.22: The measured activation energy for diffusion of ^{18}O in sapphire was lower for microwave firing as compared with conventional firing [61] (used under fair use guidelines, 2011).

The gradient of the line shown in this plot is used to calculate the measured activation energy of ^{18}O ion diffusion in sapphire. It was observed that the measured activation energy required for the oxygen ion jump was lower for microwave annealing ($385\ \frac{kJ}{mol}$), as compared to conventional

annealing ($650\ \frac{kJ}{mol}$).

Microwave induced ionic currents

Freeman et al [21] measured the intensity of ionic currents in NaCl single crystal when short pulses ($400\,ms$) of microwave power ($14\,GHz$) were applied. Their study revealed that the microwave fields yielded additional ionic currents in NaCl. These enhancements were attributed to the presence of an additional driving force due to the electric fields associated with microwaves.

Equation 2.13 shows that enhanced flux is a result of an increase in *transport coefficient* or *driving force* or both. Janney's [61] study show that the reduction in activation energy is responsible for increasing the transport coefficient that is enhancing flux. Freeman's [21] work showed that it is the presence of an additional driving force from the electric field that is contributing to accelerated matter transport. In the study undertaken for this dissertation, experiments are designed to determine if the electric field component of the microwave energy is inducing a non-zero driving force or is decreasing the measured activation energy or both.

Chapter 3

Experimental Procedure

This chapter provides the details on fabricating inert matrix material using both conventional and microwave heating techniques. Figure 3.1 provides an overview of the experimental procedure designed during the course of this study. From the view point of fuel fabrication the main features for processing a fuel pellet are material selection, powder compaction, sintering, and characterization. A brief description of each of the furnaces (both conventional and microwave) and the heating procedures adopted for this study are discussed in this chapter. As temperature measurements are often critically evaluated in a microwave furnace, a detailed explanation on the set-up used for this study is provided in Section 3.3.7. The techniques used for characterizing the sintered pellets are in accordance with the ASTM international standards.

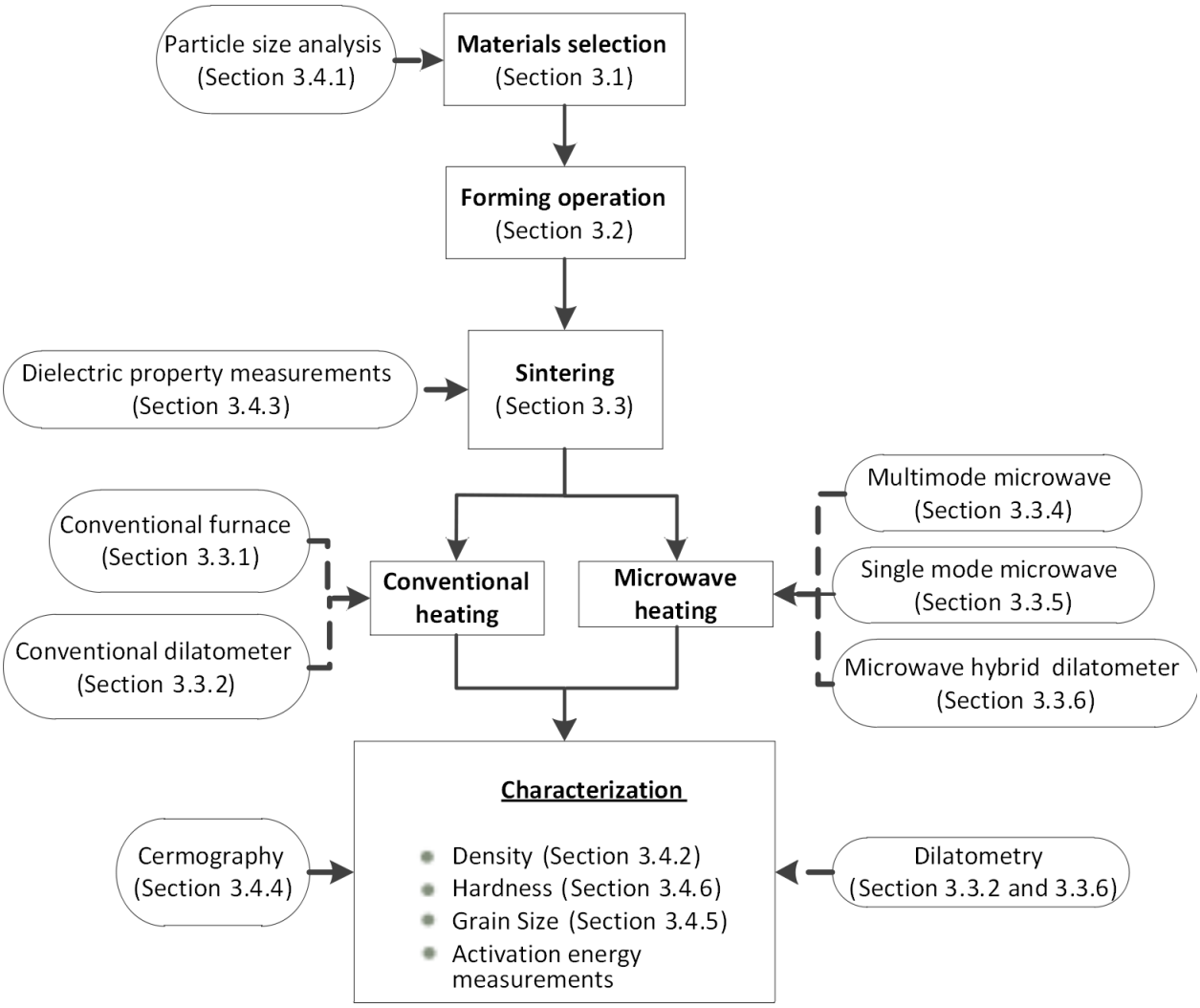

Figure 3.1: Flow chart showing the experimental procedure used for investigating the effect of microwave energy on a sintering process.

3.1 Materials

The inert matrix material used for this study is selected based on the following property requirements:

- Low neutron absorption cross section
- High melting point
- Structural stability under irradiation
- Face centered cubic - Flourite type structure

Considering the above mentioned constraints, ZrO_2 stabilized with 8 mol % Y_2O_3 (8YZ), is selected as the inert matrix material. This is due to its low neutron absorption (< 2.7 b), high melting point (2700 °C) and face centered cubic structure. The fluorite structure contains large voids in the center of the unit cell that can accommodate fission products. The structural stability of this material under irradiation was examined by Degueldre et al [62]. They have reported that fully stabilized zirconia retained its structural stability under different radiation levels (between 60 keV and 1.5 MeV) of Xe ions with $\sim 1.8 \times 10^{16}\, cm^{-2}$ dosage.

Commercially available spray dried granules of 8YZ[1] produced through a hydrolysis process was used for this study. Spray drying is a technique used for synthesizing free-flowing powder suitable for pressing. This is necessary for achieving a uniform particle size distribution to minimize

[1] TZ-8Y, Tosoh Corporation

the fabrication flaws that arise in non-uniform particles (non free flowing powders) often observed during the final sintering stage.

The detailed compositional analysis of these powders is shown in Table 3.1. It can be observed that the powders are 99.81 % pure. Apart from the base composition ZrO_2 and Y_2O_3, the presence of trace impurities[2] such as Al_2O_3, SiO_2, Fe_2O_3, and Na_2O, can be seen in Table 3.1.

Table 3.1: Compositional analysis for 8 mol % Y_2O_3-stabilized ZrO_2.

Composition	**Mol %**
ZrO_2	91.9813
Y_2O_3	7.8385
Al_2O_3	0.0063
SiO_2	0.0065
Fe_2O_3	0.0032
Na_2O	0.1639

3.2 Powder compaction and pellet fabrication

Approximately 3.5 g of the as-received powder was poured into the mold, which was tapped for a period of 5 s. The compaction behavior of these powders was studied using both uniaxial pressing and cold isostatic pressing. Both of these techniques involve the following three steps: (1) filling of the mold with powdered particles, (2) pressing, and (3) pellet ejection.

[2]As reported by Tosoh Corporation

3.2.1 Uniaxial pressing

Figure 3.2a shows the uniaxial mold design that was used to make right circular cylindrical shapes with an aspect ratio of one (this is a typical shape of nuclear fuel).

Along with the uniaxial mold design, Figure 3.2a shows the high carbon stainless steel die used for pressing 8YZ powders. A single-action pressing technique is used for uniaxial compression of the powders in the die. The bottom ram supports the powdered particles, while the top ram moves and compacts the powder. The single-action pressing technique involves the application of pressure only through the top ram; the bottom ram and the die are fixed. The consequence of this process is that the powder particles (inside the die) will undergo simultaneous rearrangement and compaction, resulting in a right circular cylindrical shape.

A typical green pellet pressed using uniaxial pressing is shown in Figure 3.2b. It was observed that the conventional sintering of the uniaxial pellets resulted in end capping and spalling type defects (see Figure 3.2b).

The end capping defect observed during uniaxial pressing (shown in Figure 3.2b) is attributed to the sudden release in the elastic compression experienced by the particles along the pressing direction. This situation is often termed as *springback or strain relaxation*. During the pellet ejection process the surface of the pellet experiences frictional drag with the die wall. This will result in spalling type defects. A schematic of this situation is shown in Figure 3.3. These defects may be are invisible in the green pellet, but are greatly enhanced during sintering leading to spalling and end cap type defects (shown in Figure 3.2b).

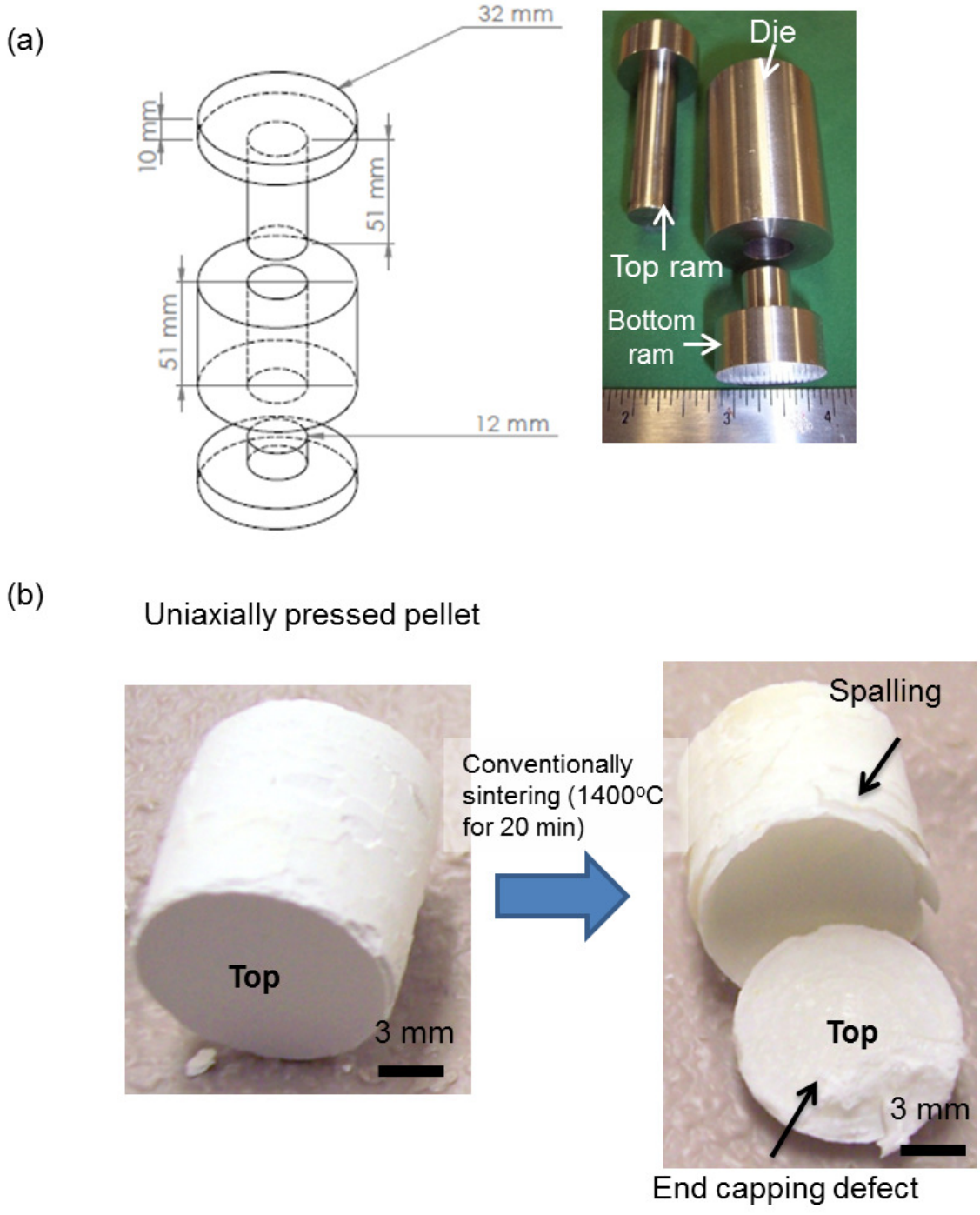

Figure 3.2: (a) Design specifications for the uniaxial mold along with the actual picture of the mold and (b) Powders compacted using uniaxial pressing resulted in enhancement of defects after sintering.

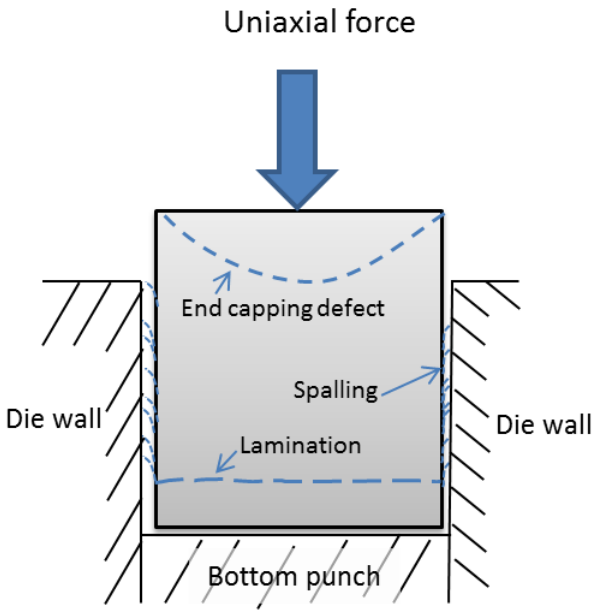

Figure 3.3: Schematic showing the mechanism of formation of end capping, spalling and lamination type defects during uniaxial pressing.

3.2.2 Isostatic pressing

The defects produced during sintering uniaxially pressed pellets have been avoided by adopting isostatic pressing. Figure 3.4a shows the design specifications of the isostatic mold used for this study along with the actual picture of the mold[3].

Isostatic pressing[4] involves the application of hydrostatic pressure to a rubber mold containing powdered particles. Figure 3.4b shows the isostatically pressed pellet. It can be observed that the isostatic pressing resulted in the absence of defects after sintering (see Figure 3.4b).

The isostatic compaction of powders results in application of force equally along all directions. A schematic of this situation is shown in Figure 3.5. The release in pressure is also equal in all

[3] "TR" Polyurethane, The Trexler Rubber Company, Inc.,
[4] ISI, ISO-Spectrum Inc.,

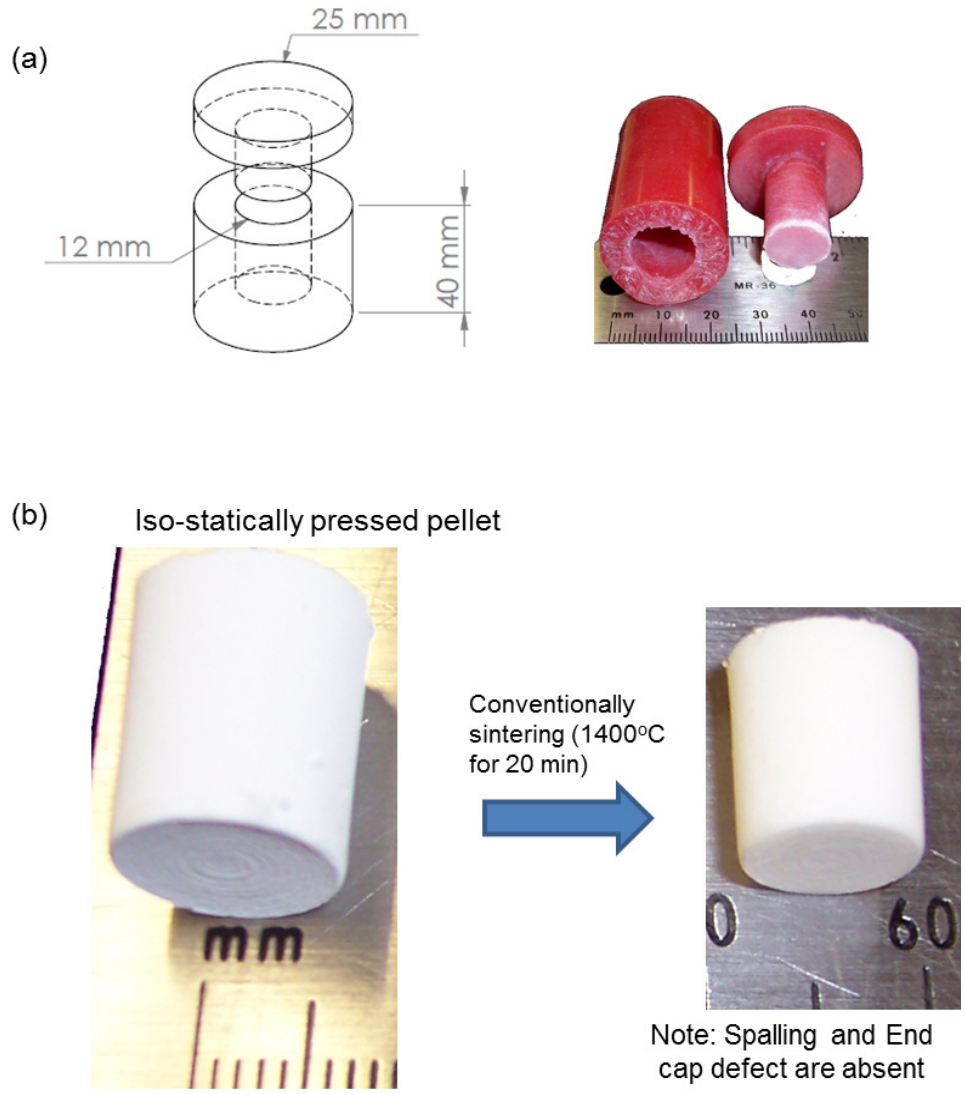

Figure 3.4: (a) Design specifications for the isostatic mold and the actual picture of the mold (b) Isostatically pressed powders showed few, if any, defects after sintering.

directions allowing the strain relaxation to be equal in all directions. Also, there is no frictional drag associated with compacted powders and the rubber mold during the ejection of the pellet. These situations improve the overall sintering behavior of the green pellet made using isostatic pressing (see Figure 3.4b). Therefore, isostatic pressing was used to further study the effect of pressure (37 to a maximum of 200 MPa) on compaction behavior of these powders (presented in Section 4.2).

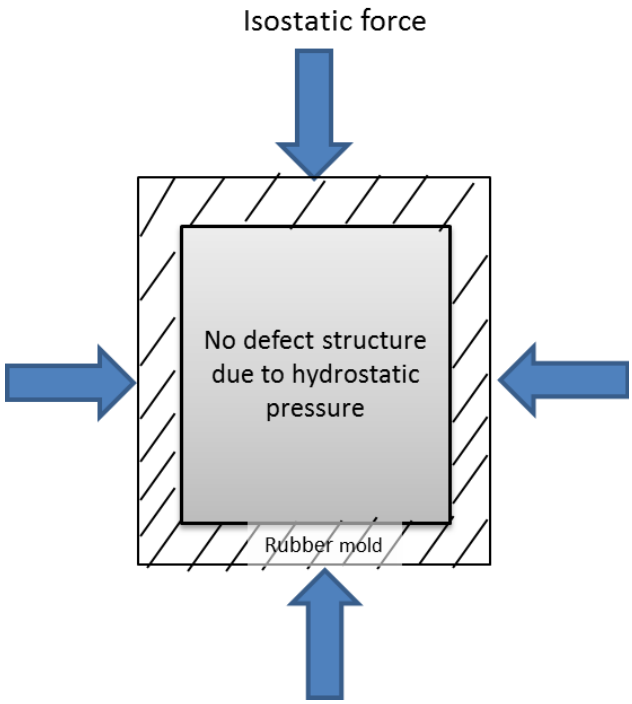

Figure 3.5: Schematic showing the hydrostatic distribution of force in isostatic pressing results in defect free pellet.

3.3 Sintering

3.3.1 Conventional furnace

The conventional sintering runs were performed in a high-temperature furnace[5]. This furnace utilizes resistance type heating elements (molybdenum disilicide). The molybdenum disilicide elements are exposed in the oven chamber thereby heating the inner chamber wall and simultaneously radiating heat to the sample. This furnace was rated to a maximum operating temperature of 1650°C in air. Temperature measurement inside this furnace is monitored using an alumina-sheathed, type-R, platinum-rhodium thermocouple. To ensure that the temperature measured by the thermocouple is the actual representation of the sample, a setter plate is used to bring the sample close to the vicinity of the thermocouple (shown in Figure 3.6a).

Figure 3.6a shows the schematic sketch of the conventional furnace along with its three main components: heating elements, thermocouple and sample positioning. Figure 3.6b shows the picture of the actual furnace used for sintering experiments. The desired heating rates for sintering experiments is controlled by a feedback controller.

The heating profile used for examining the effect of temperature on sintering behavior is shown in Figure 3.7. Sintering experiments were performed at five different temperatures (1000, 1100, 1200, 1300, 1400, and 1500 °C). The heating rate (20 $\frac{^{\circ}C}{min}$) and the soaking time (20 min) were set to be constant for all the experiments.

[5]CM bloomerg model no: 0100153

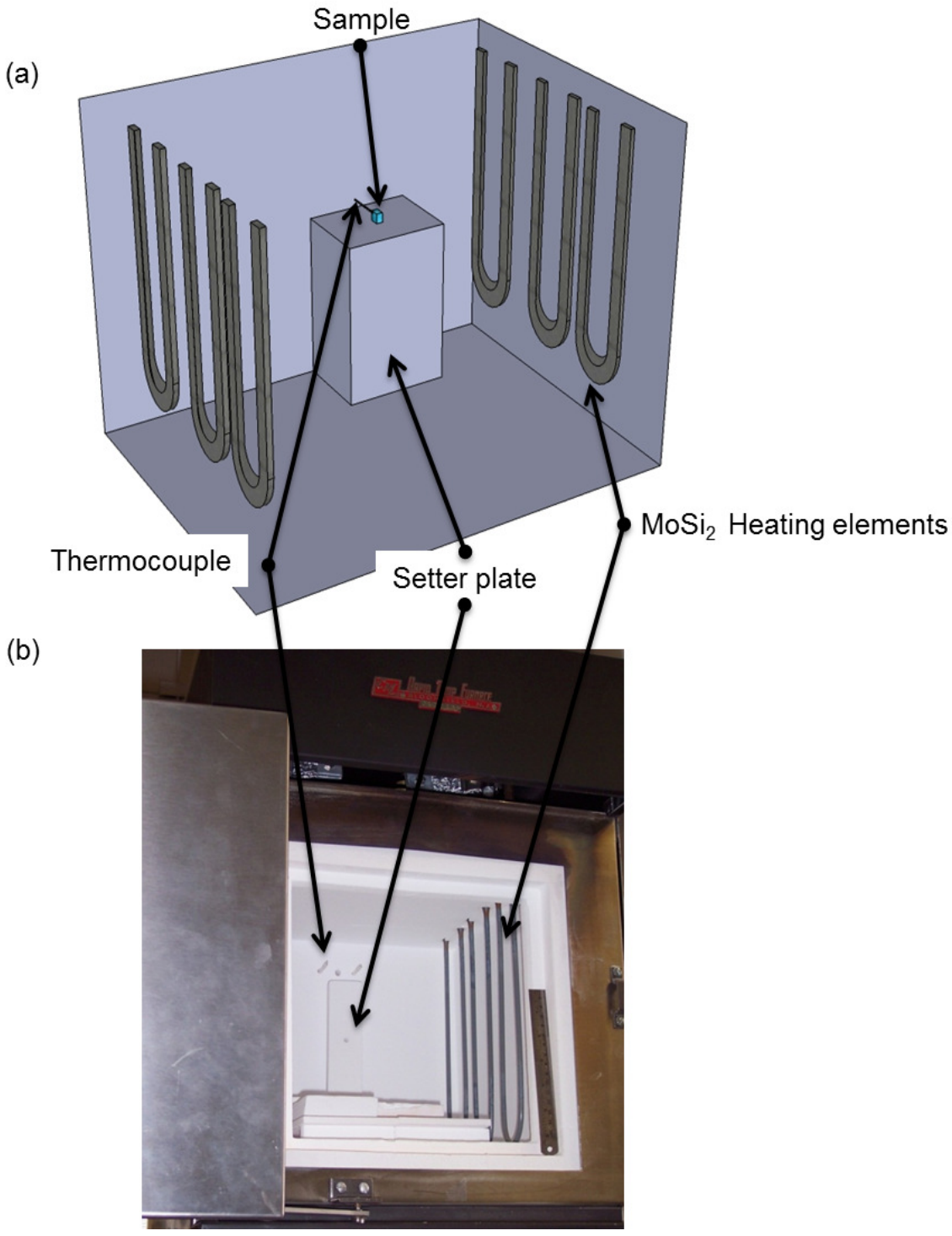

Figure 3.6: (a)Schematic sketch and (b) the actual picture of the conventional furnace used for conducting sintering experiments.

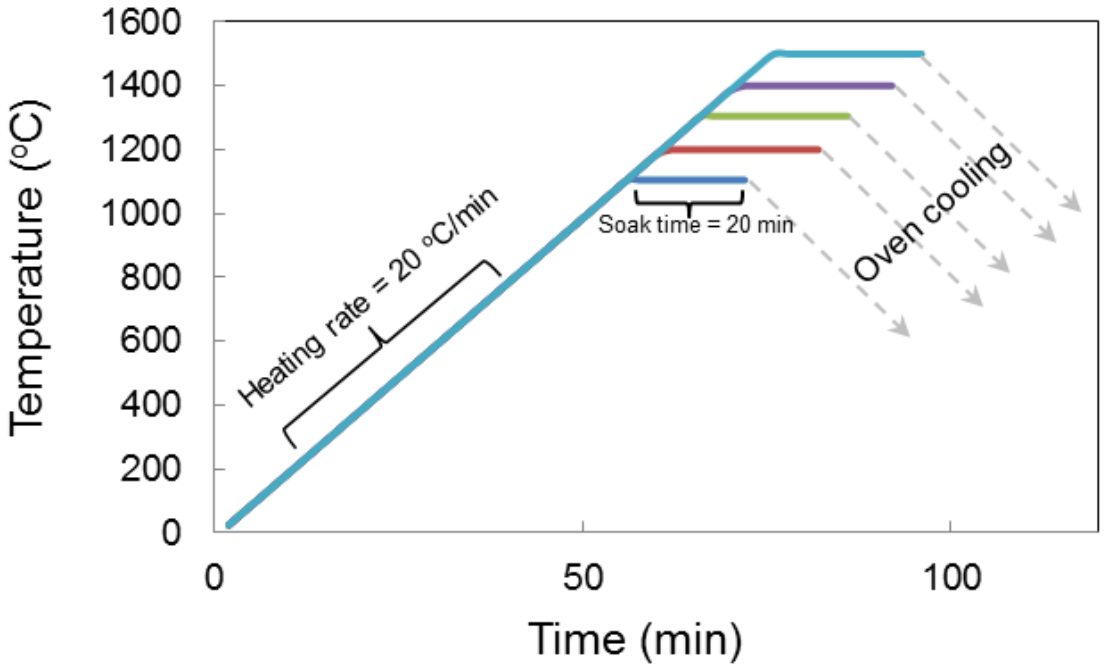

Figure 3.7: Schematic sketch of the temperature-time profile used for studying the effect of temperature on sintering 8YZ.

Equation 3.1 shows the general equation used for quantifying sintering. It shows the relationship between linear shrinkage and the processing variables [63].

$$\frac{\Delta L}{L_\circ} = -\left(\frac{2\pi D c V_m x^2 t}{RTa^3}\frac{d\mu}{dx}\bigg|_\gamma\right)^{\frac{1}{2}}; \text{here } D = D_\circ \exp\left(-\frac{Q}{RT}\right) \tag{3.1}$$

A detailed description of the above equation can be found in Appendix A.1. The term D in Equation 3.1 is the self diffusion in the absence of a driving force; this term is exponentially related to temperature. The terms t (time), and T (Temperature) have their usual meanings. The following observations can be made from Equation 3.1:

- for a given temperature-time profile, a small decrease in the initial size of the particle would result in an increase in the sintering rate. Shrinkage is proportional to $a^{-1.5}$
- for a given particle size, it seems as if though the temperature has a minor contribution to the overall sinteirng rate. In fact it is the diffusion coefficient D, that is raised exponentially with temperature and this leads to an acceleration in sintering. Shrinkage is proportional to $\exp\left(-\frac{Q}{RT}\right)$
- isothermal sintering would show a sudden acceleration in sintering within a short period of time, but, with further increase in time it would take a longer period to show any further sintering. Shrinkage is proportional to $t^{0.5}$

One of the limitations with conventional furnaces is that linear shrinkage measurements cannot be made in-situ. This is essential for evaluating the *objective # 5* (presented in Section 1.3), as the

models adopted for determining activation energy require in-situ shrinkage measurements (outlined in Section 2.3.7). Push-rod dilatometers are the most common and reliable way of measuring the thermal expansion/contraction experimentally. The following section outlines the details on the conventional push-rod dilatometer that was used for this study.

3.3.2 Conventional dilatometer

Conventional dilatometers are broadly categorized into two main classes: (1) relative methods, in which the linear expansion/contraction is measured relative to that of another material; and (2) absolute methods, in which the expansion/contraction of the material is measured directly. The dilatometer that is used for this study utilizes an absolute method of measuring the expansion/contraction of the material.

Figure 3.8 shows the actual picture of the dilatometer[6] used for this study. It consists of a bridge supporting the measuring head, and the alumina holder. This bridge is attached to the conventional furnace. A closer look at the alumina holder (inset in Figure 3.8) shows the positioning of the thermocouple with respect to the sample. Here the push-rod holds the sample in place to the alumina holder. The alumina holder is designed in such a way that the push-rod, thermocouple and the sample can be carefully moved in and out of the furnace.

During sintering experiments, the furnace not only heats the sample, but would also heat the alumina tube and the push-rod. The result is that the final shrinkage of the sample recorded by the

[6]P 367, Theta Industries Inc.,

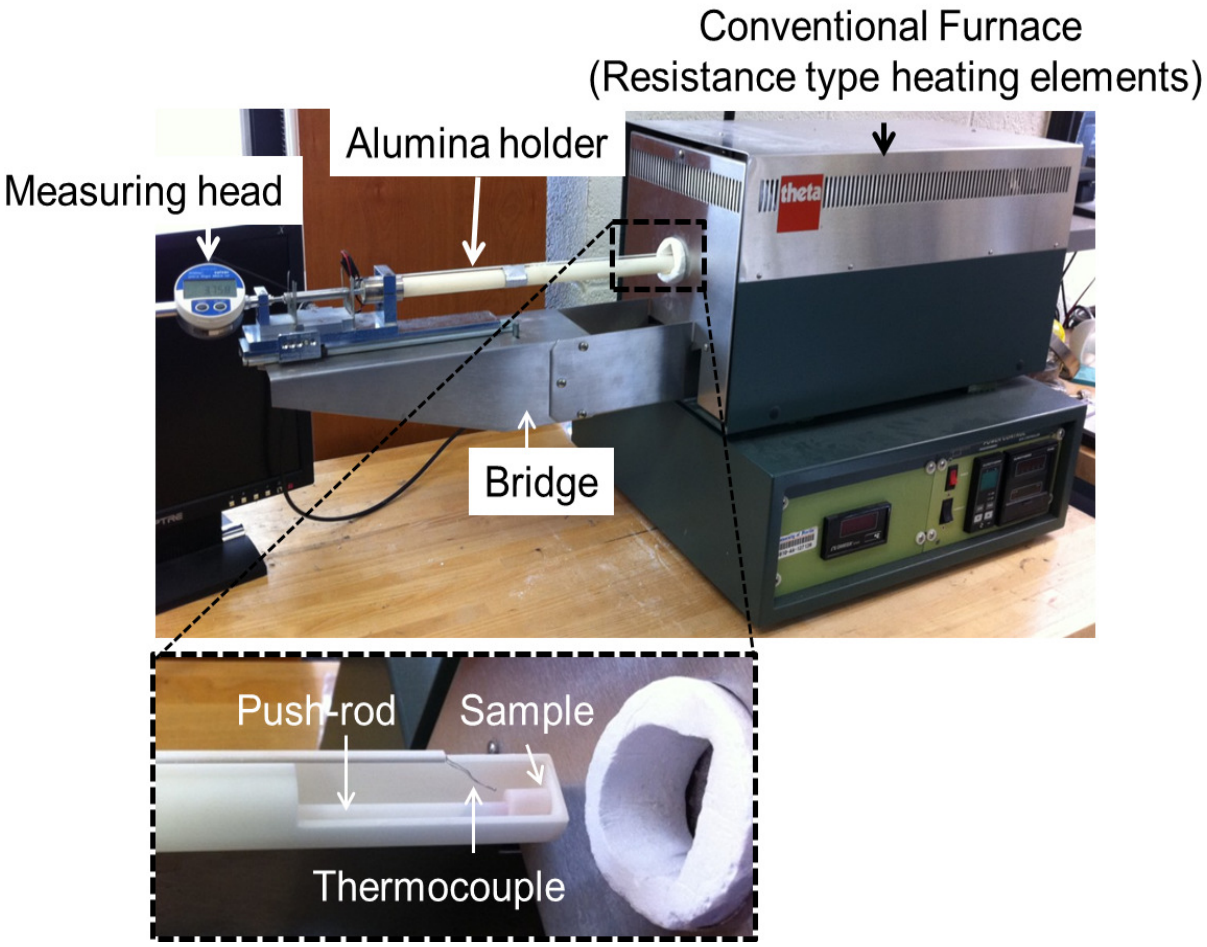

Figure 3.8: Dilatometer used for conducting in-situ linear shrinkage measurements during conventional heating.

measuring head has the expansion of the tube (alumina holder) and the push-rod. This situation is shown in the following equation:

$$\left(\frac{\Delta L}{L_o}\right)^{\text{Measured}}_{\text{Shrinkage}} = \left(\frac{\Delta L}{L_o}\right)^{\text{True}}_{\text{Shrinkage}} + \left(\frac{\Delta L}{L_o}\right)^{\text{Push-rod}}_{\text{Expansion}} + \left(\frac{\Delta L}{L_o}\right)^{\text{Alumina holder}}_{\text{Expansion}} \tag{3.2}$$

From the above equation it can be observed that the true shrinkage of the sample can be obtained by subtracting the expansion of the alumina holder and the push-rod from the total measured shrinkage.

The expansion of the alumina holder and the push-rod are determined by measuring the expansion of a reference standard, that is identical to the length of the sample (for a given heating rate). For this study, high purity (99.99%) alumina[7] was used as a standard reference material for determining the expansion of push-rod and the alumina holder.

Figure 3.9 shows a typical sintering cycle used for measuring the percentage linear shrinkage during isothermal sintering experiments. As mentioned in Section 2.3.7 the isothermal runs usually involve fast heating rates. The time required to reach a target density or linear shrinkage is observed as a function of temperature. The slope of the line representing the log of densification or percentage linear change with respect to $\frac{1}{T}$ would result in the activation energy (see Equation 2.29).

Figure 3.10 shows the typical sintering cycle used for monitoring the percentage linear shrinkage as a function of heating rate for non-isothermal sintering experiments. This data is required for

[7]Theta 410, Theta Industries Inc.,

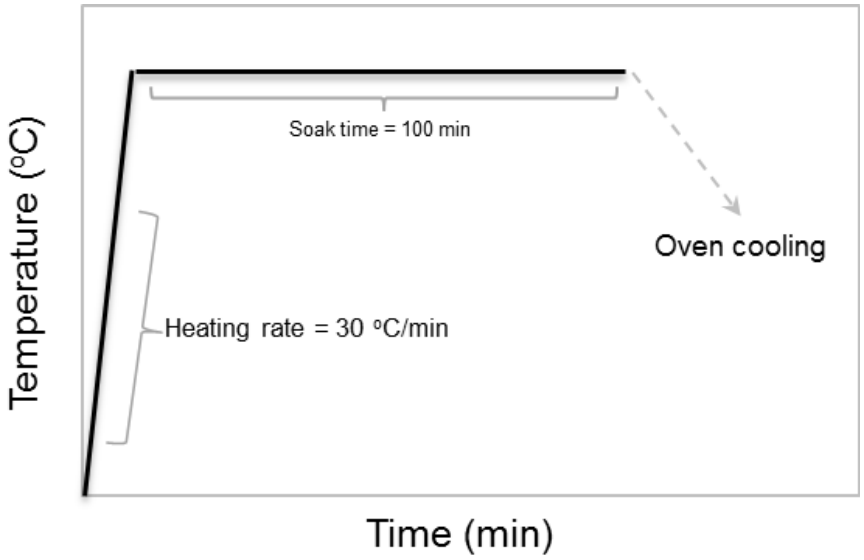

Figure 3.9: Heating profile adopted for conducting isothermal sintering experiments for determining activation energy for sintering 8YZ.

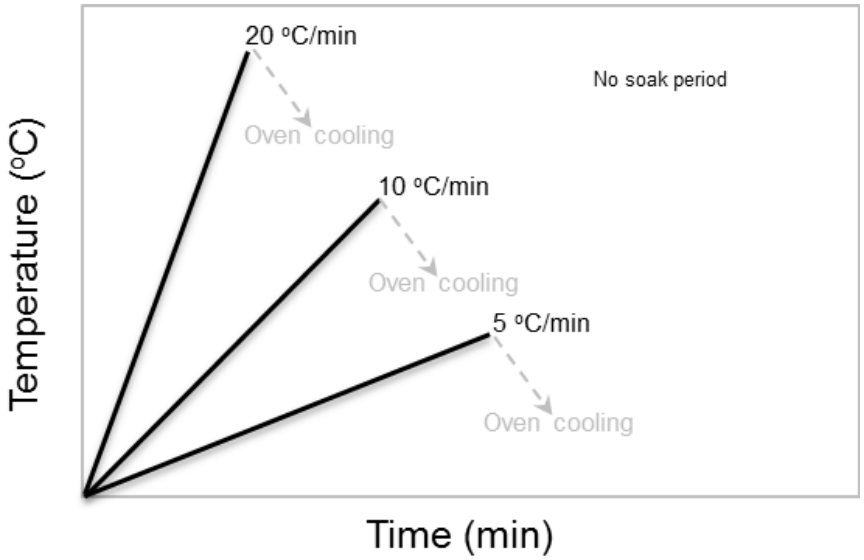

Figure 3.10: Heating profile adopted for conducting nonisothermal sintering experiments for determining activation energy for sintering 8YZ.

determing the activation energy using non-isothermal sintering methods (outlined in Section 2.3.7). Due to the limitation with the equipment design both of the above mentioned sintering cycles (non-isothermal and isothermal) were allowed to oven cool.

3.3.3 Microwave furnace components

The microwave heating system consists of: (a) microwave generator, (b) transmission-line, and (c) applicator. A typical home model microwave oven has all of these components packed into one single unit. The only component that is visible to the end user of the home microwave is the applicator (cavity) as this is used for heating food. Microwave furnaces used for conducting research require greater control over each of the above mentioned components. A schematic sketch of each of the components are shown in Figure 3.11 and a brief description is provided below:

Microwave generator: Microwave generators consist of a magnetron for producing microwave energy. Magnetrons are made up of a cathode enclosed in circular anode cavities. These cavities are surrounded by powerful magnets designed for producing strong magnetic fields inside the cavity. The cathode produces electrons when heated (using high currents), these are accelerated towards anode. Due to the surrounding magnetic field the electrons move in a spiral path inducing alternating currents in the anode cavities. This will result in the generation of electromagnetic wave. It is the size of the anode cavity that determines the frequency of the electromagnetic radiation. The magnetron used for this study produced 2.45 GHz microwave frequency. The output of this field is transfered into the transmission line (wave guide) using a small loop. The transmission line

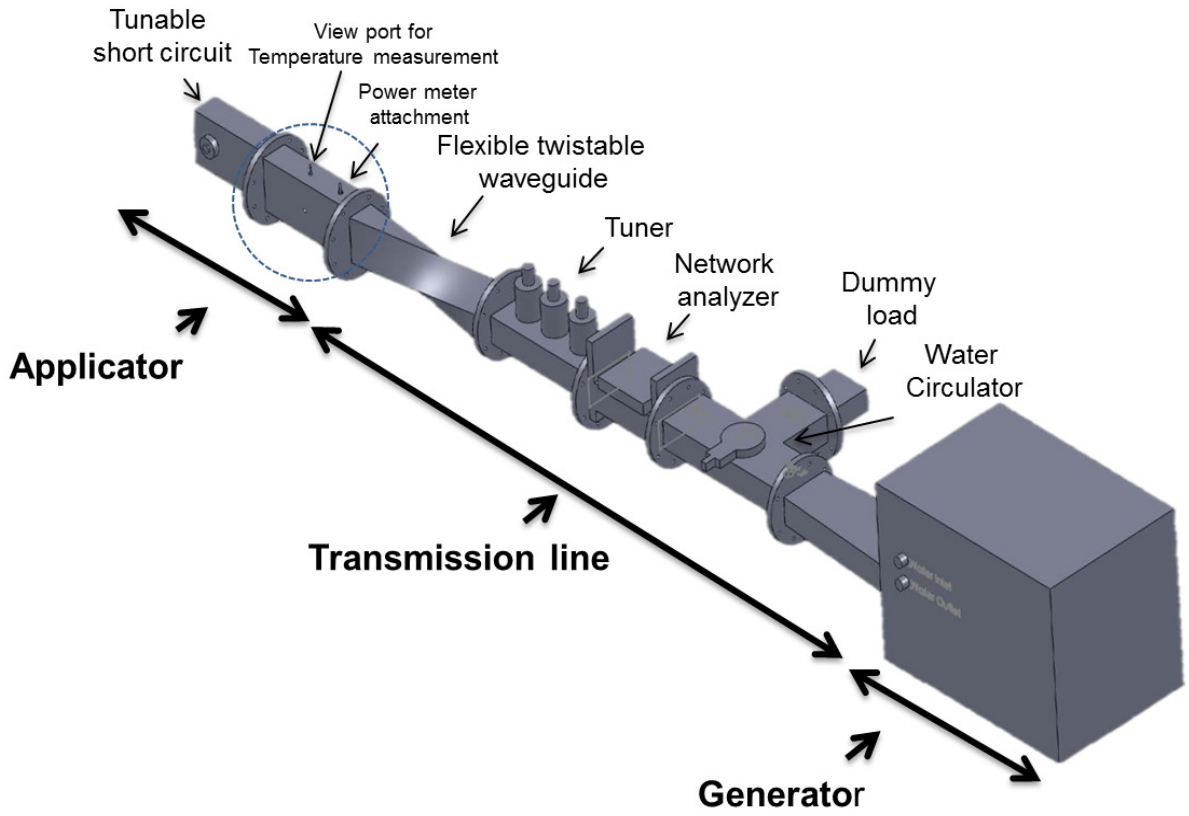

Figure 3.11: A schematic sketch of various components in the microwave furnace used for this investigation.

would essentially transfer the electromagnetic radiation to the applicator containing load (material to be heated).

Two types of microwave generators[8] were used for this study. These generators have a built in cooling system for protecting the magnetron from over heating. The power of the microwaves is regulated by controlling the voltage applied to the anode. This is done using a high power supply unit[9].

Transmission line: Waveguides provide a viable means of transmitting high power microwaves, from generator to the load (see Figure 3.11). These are essentially hollow metallic tubes either rectangular or circular in shape, made using brass, copper or aluminum. An example of a TE_{10} rectangular type wave guide[10] used for this study is shown in Figure 3.12a. A flexible twistable waveguide made using brass (with a polymer encasing) was also used for this study that allowed 90 degree rotation flexibility to the microwave applicator (shown in Figure 3.11).

In free space, the electric field and the magnetic field components of microwaves are perpendicular to the direction of propagation; these are often referred to as TEM (transverse electromagnetic) waves. TEM wave propagation is well defined in space and time; this is quantified using Maxwell's equations. During microwave energy transmission, the TEM waves are confined to the boundaries of waveguide (see Figure 3.12a), this would restrict the wave propagation to either transverse electric (TE) or transverse magnetic (TM) waves. In TE waves the electric field component is perpendicular to the direction of propagation whereas in a TM waves the magnetic field is

[8] Singlemode: CWM-4S, Cober Electronics, Inc.,; Multimode: GA4006A, Gerling Applied Engineering, Inc.,
[9] Singlemode: SM 1545D, 10242, Cober Electronics, Inc., Multimode: SM 1150, Alter Reggio Emlia, Italy
[10] WR284, Space Machine and Engineering Corp

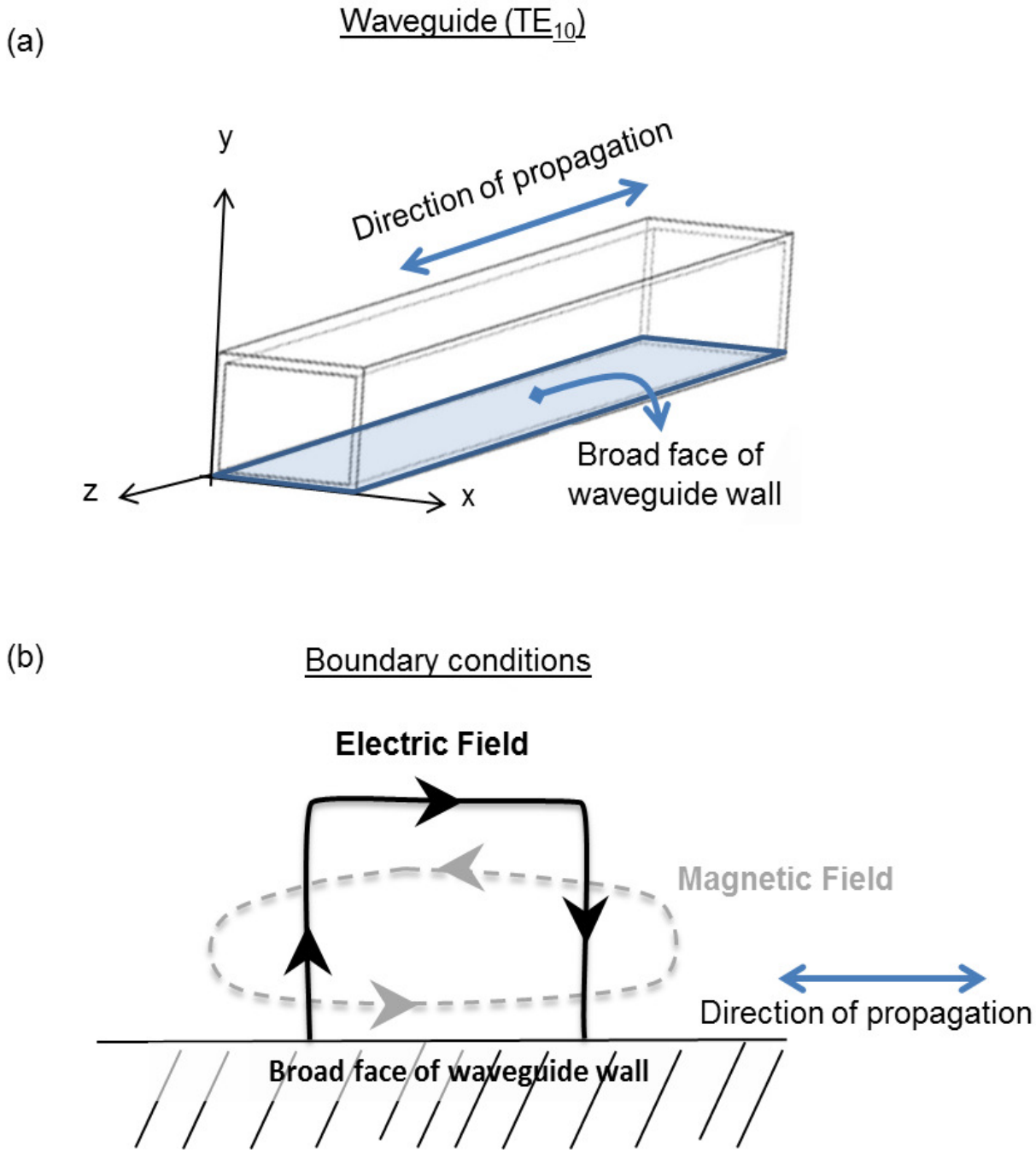

Figure 3.12: Schematic sketch of (a) TE_{10} wave guide and (b) the electromagnetic field distribution along the boundary wall of waveguide.

perpendicular to the direction of propagation. The type of wave pattern (TE or TM) is dependent on the geometry of the waveguide. These distributions can be obtained by applying the boundary conditions (defined by the geometry of waveguide) to the Maxwell's equations. The equations defining the wave propagations in waveguides is not presented here as this is not the major focus of this study. Instead, two of the most important conditions have been outlined below to help visualize the microwave field distribution in a TE_{10} type of wave guide.

- The electric fields are perpendicular to the broad faces of the TE_{10} waveguide (see Figure 3.12b)
- The magnetic fields form closed loops that are parallel to the broad faces of the waveguide (shown in Figure 3.12b).

Figure 3.13 illustrates the distribution of wall currents, electric and magnetic fields in a typical TE_{10} waveguide. The solid lines are electric fields patterns aligned perpendicular to the direction of propagation (along z direction). It can also be observed that the magnetic fields are oriented along the direction of propagation (parallel to the z direction). It is essential to know the positioning of wall currents and the field distribution from the stand point of making slots along the surface of the waveguide. These slots are useful for attaching temperature sensors and power meters (for measuring the electric field intensities). Also, for a given frequency the electric and magnetic fields show half sinusoid variation along the waveguide with an effective wavelength $(\frac{\lambda_g}{2})$, where λ_g is the guided wavelength that is different to the wavelength observed in free space.

The main objective of the transmission line is to provide an efficient means of transferring

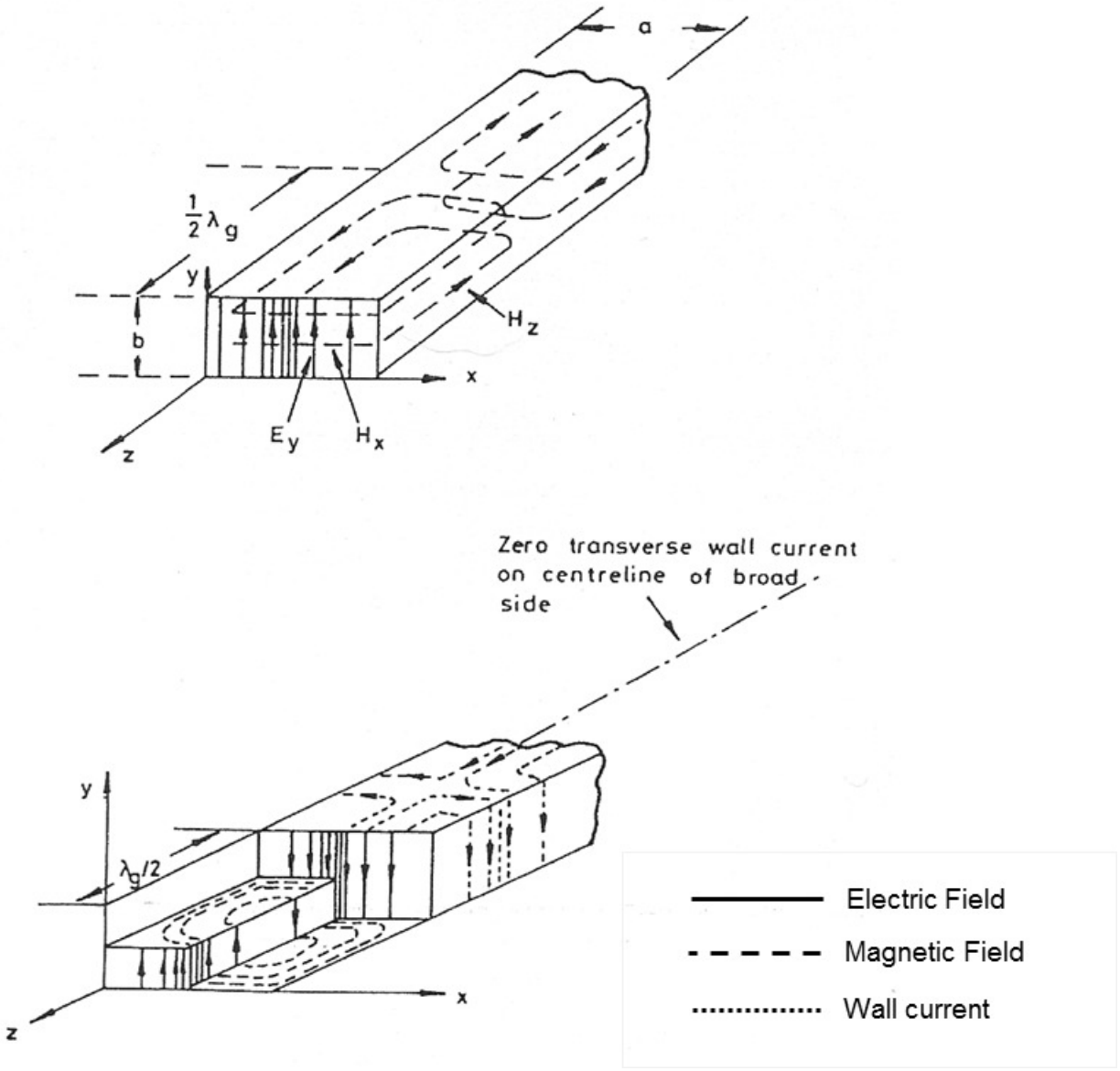

Figure 3.13: Electric and magnetic field distribution along TE_{10} type rectangular waveguide[46].

microwave energy from generator to the applicator. The transfer efficiency is limited by

1. the microwave absorption along the waveguide; these losses are often neglected as they are very small, and

2. the power reflection due to improper load matching; this is a result of poor absorption of microwave by load/material.

These situations will create partial reflection of microwave energy back to the generator. The percentage of reflected waves are distinguished from that of the forward waves using a network analyzer. The network analyzer[11] (shown in Figure 3.11) uses a directional coupler to measure the voltage induced by a forward and backward wave. The reflection coefficient, S_{11}, which is the voltage ratio of forward wave to the reflected wave is instantaneously displayed on a Smith chart[12] using a network analyzer software.

To prevent the reflected waves from entering back to the magnetron a circulator[13] is installed between network analyzer and the microwave generator (see Figure 3.11). This will preferentially divert the reflected waves toward the microwave absorbing dummy load[14] (deionized water, see Figure 3.11). Tuners[15], shown in Figure 3.11 does the same job of preventing the reflected waves from entering back into the magnetron by redirecting the reflected waves back to the cavity using adjustable metallic stubs.

[11]MW-HWD 2450-00, Muegge
[12]Circumferential scaling between magnitude of S_{11} with respect to the phase angle
[13]WG284-3PC, 2.45 GHz, Cober Electronics Inc.,
[14]GA1201, Gerling Applied Engineering
[15]GA100x, Precision 3-stub tuner, Gerling Applied Engineering

The flexible twistable waveguide shown in Figure 3.11 is also a part of the transmission line as it allows the microwave cavity to rotate by a 90° angle without altering the field distribution. This is essential for attaching the dilatometer assembly, specifically designed for this study (discussed in Section 3.3.6).

Applicator: Applicators are essentially hollow metallic cavities that contain load (in some cases are similar to waveguides). The microwave signal fed into these cavities will suffer multiple reflections along the preferred directions. The forward and reflected waves in the cavity superimpose on one another, producing a standing wave pattern. These standing wave patterns are well-defined and are a function of the cavity dimensions [46].

There are many different types of microwave cavities found in the literature. These are mainly classified into singlemode and multimode cavities. Singlemode cavities allow only a single wave pattern; one such cavity with its electric field distribution is shown in Figure 3.16. This cavity is designated as TE_{103}. It is expected that the presence of a load inside the TE_{103} would perturb the field. To restore the original modes (within the cavity), the closing end of the waveguide is attached to a movable wall (tunable short circuit, shown in Figure 3.11). This design allows one to alter the length of the cavity to restore the distribution of the field in the cavity when a load is introduced. Cavities that have more than one type of wave pattern are referred to as multimode applicators. Multimode applicators are designed to support large number of resonant modes at a given frequency. One such multimode applicator used for this study is shown in Figure 3.14.

The advantage of multimode applicators is that they are versatile in accepting a wide range of heating loads. The advantage with single mode cavities is the well-defined field distribution that

can be measured precisely. This precision will allow for proper positioning of the sample at high intensities of electric field during processing. Also, the power distribution per unit mode is higher in single mode than the multimode cavities.

All of the components shown in Figure 3.11 were controlled via. a power interface that was run by a software. The power interface and the software used for this study were developed by former Ph.D students, Carlos Folgar and Patricia Mellodge, at Virginia Tech.

3.3.4 Multimode microwave furnace

The multimode microwave applicator[16] shown in Figure 3.14 was used for performing microwave-assisted sintering experiments in this study. The following are the dimensions of the cavity: $254\,mm \times 394\,mm \times 419\,mm\,(l \times b \times h)$. Figure 3.14a shows the overall furnace design; it can be observed that a special type of waveguide ("H-plane bend") was used to connect the applicator to the transmission line. A network analyzer and power meter were used for simultaneous monitoring of the reflection parameter S_{11}. This is the signal used for tuning the cavity to its best possible resonant mode. The heating rate for the sintering experiments is controlled by manually increasing the applied power.

Microwave hybrid (combination of microwave and susceptor heating) sintering experiments were performed in multimode microwave applicator. Figure 3.14b shows the sample location, the susceptor design and the insulation[17]. The susceptor was made of 2 wt% partially stabilized ZrO_2[18]

[16]Gerling Applied Engineering no. 930096
[17]KVS 174/400, Rath Incorporated
[18]TZ-3YS, Tosoh Corporation, USA

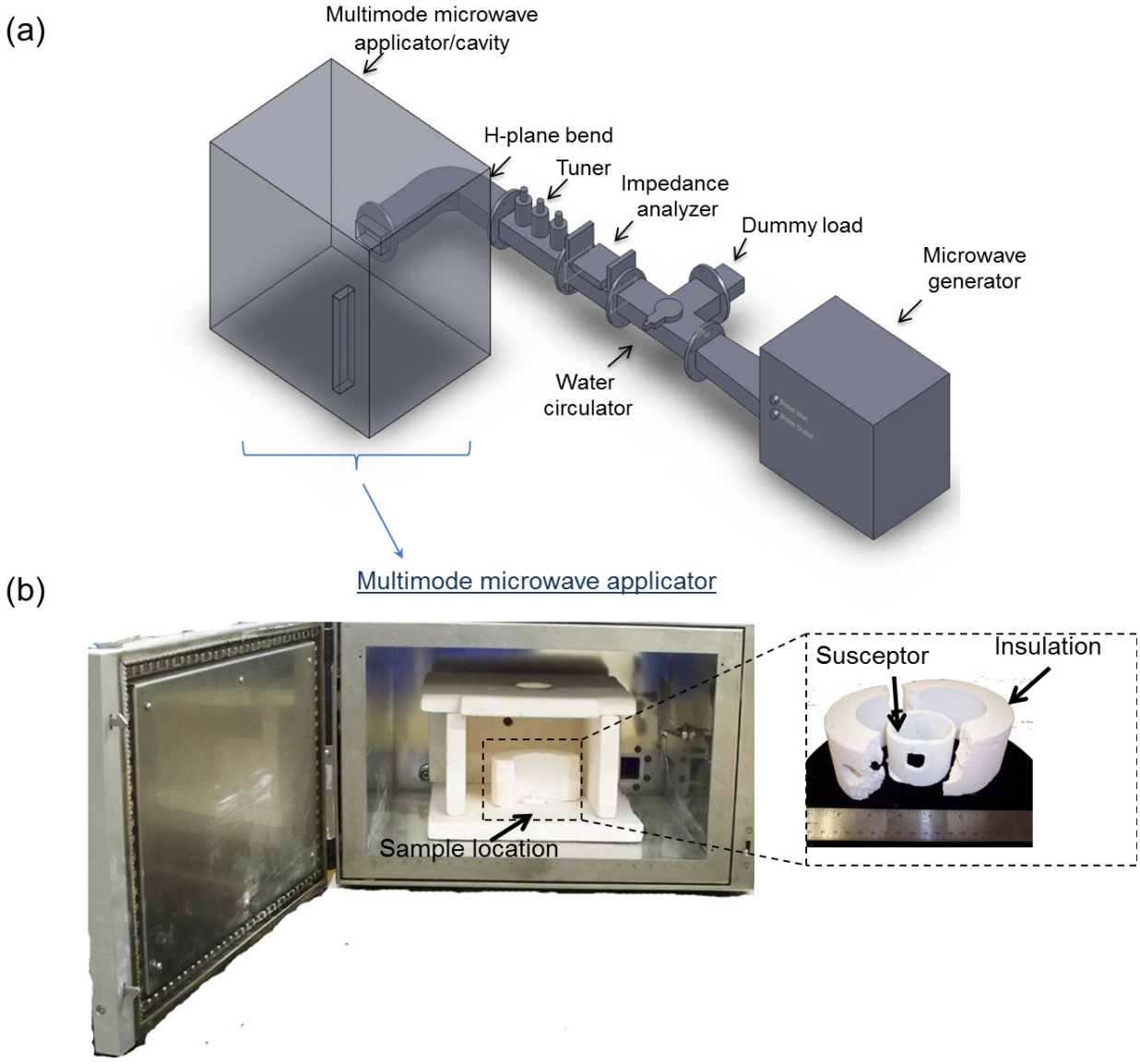

Figure 3.14: (a) Schematic sketch of the multimode microwave system used for performing hybrid sintering experiments and (b) Multimode microwave cavity showing the insulation, the susceptor design and the sample location.

with 98 wt% Al_2O_3 cement[19]. This particular composition allowed the susceptor to supply heat to the sample in a conventional manner. The temperature measuring unit was installed from the bottom of the cavity (not seen in the Figure 3.14b) so that the thermocouple is close to the vicinity of the sample. A compression type fitting was used to connect the thermocouple to the applicator (details are provided in Section 3.3.7).

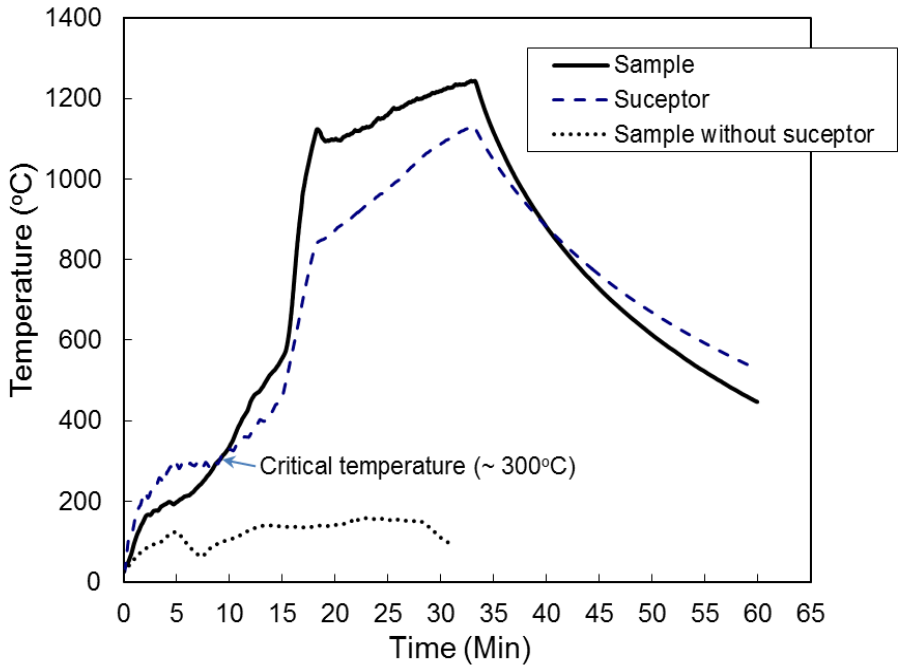

Figure 3.15: Temperature-time profile for susceptor and sample. Data collected from the multimode microwave furnace.

Figure 3.15 shows the heating profile of susceptor and the sample. It can be observed that the sample without the aid of the susceptor was unable to reach temperatures above 150°C by-itself. With microwave hybrid heating the susceptor preferentially absorbs microwave energy and provides heat to the sample conventionally. Above the critical temperature (> 300 °C) the sample absorbs microwaves and continues to heat by itself independent to susceptor (see Figure 3.15).

[19] Alfrax No. 66, Saint-Gobain Ceramics, MA

3.3.5 Single mode microwave furnace

Direct microwave sintering experiments were conducted in a Transverse Electric (TE) single mode microwave cavity $(72\ mm \times 34\ mm \times 307\ mm)$. In TE cavities, the electric field (see Figure 3.16) associated with a microwave signal (Y-axis) is perpendicular to the direction of propagation (Z-axis) [46]. As seen in Figure 3.16, the standing wave pattern has one variation along the x-direction, a zero variation along the y-direction, and along the z-direction there are three $\frac{1}{2}$ wavelengths. Thus, these cavities are designated as TE_{103} microwave cavities.

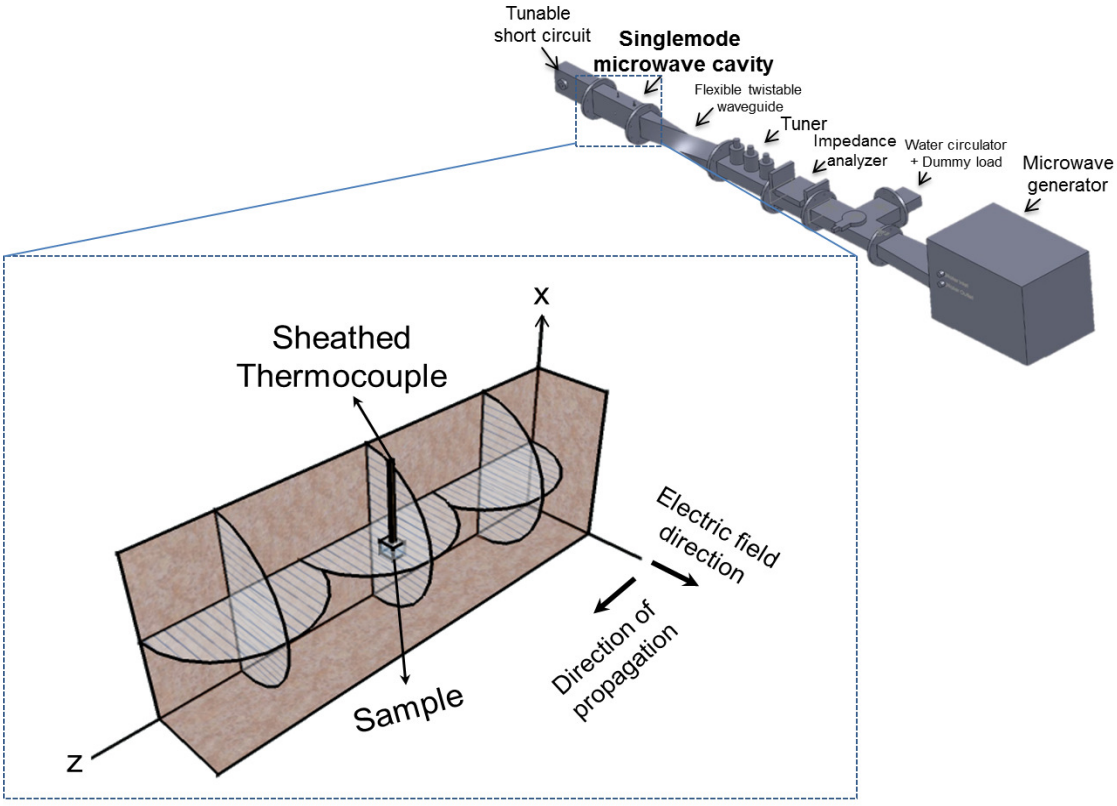

Figure 3.16: Electric field pattern in a TE_{103} singlemode microwave cavity.

Due to the fact that microwave absorption (by a sample) depends on the incident electric field

(see Equation 2.32), microwave sintering experiments were conducted along the regions of high-intensity electric fields (sample region is shown in Figure 3.16).

The heating profile adopted for studying the effect of temperature on sintering behavior was kept the same as that of conventional and microwave assisted heating (see Figure 3.7). This is essential to compare the sintering behavior of the green pellet using conventional and microwave heating techniques.

As outlined in Section 3.3.1 the limitation with studying the sintering phenomena in microwave furnaces is that the linear shrinkage cannot be measured in-situ. Several models have been identified for estimating the activation energies for sintering (for details see Section 2.3.7). The majority of these models require in-situ monitoring of linear shrinkage, usually obtained from a standard dilatometer. While conventional dilatometers are readily available, dilatometers that use microwave energy as a heat source are non-existent. Therefore, for this study, a hybrid type of dilatometer was designed and built that utilized Silicon Carbide (SiC) suceptors for studying the sintering behavior (of 8YZ) as a function of electric field intensity.

3.3.6 Microwave hybrid dilatometer

The microwave hybrid dilatometer design had a SiC suceptor that allowed variation in the electric field intensity (along the sample) without any loss in temperature. This is a requirement since the rate of raise in temperature during microwave heating is directly related to the applied electric field (see Equation 2.32).

The dilatometer setup has a push-rod assembly that is used for in-situ linear shrinkage measurements. The SiC suceptors were placed directly into the microwave cavity (along the regions of low intensity electric fields). A schematic of this design is shown in Figure 3.17. The relevant hardware, software, and the calibration procedure developed for this instrument are outlined in Appendix A.

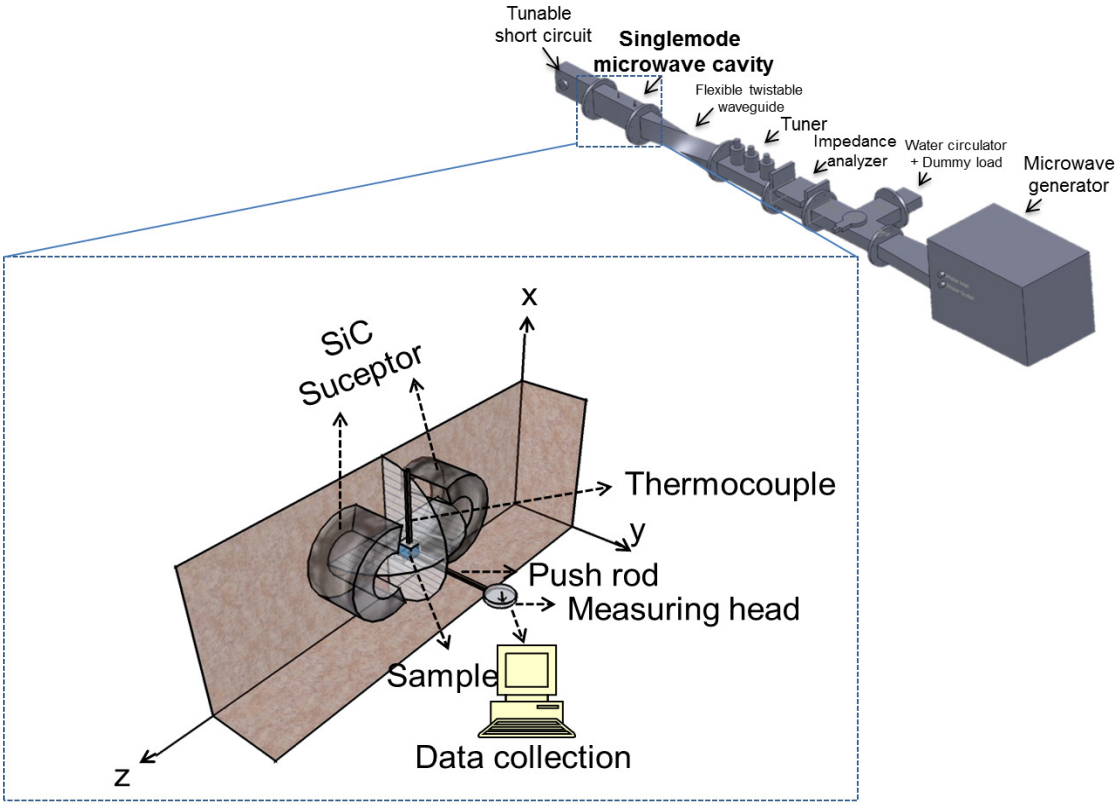

Figure 3.17: Schematic sketch of the microwave hybrid dilatometer specifically designed for this study.

The heating profiles adopted for performing the non-isothermal and isothermal sintering experiments were the same as that of the conventional dilatometer experiments (see Figure 3.9 and 3.10).

3.3.7 Temperature monitoring system

Thermocouples are the most common way of measuring temperature inside a furnace, but conducting temperature measurements in a microwave furnace is not a simple task due microwave interaction with metallic elements of thermocouples. It has been observed that the thermocouples exhibited simultaneous arching and melting of leads in relatively short periods of time inside microwave furnaces.

Non-contact temperature techniques, such as infrared sensors, were used to measure the temperature in the microwave furnace as an alternative to thermocouples [64]. The lack of reliable data on emissivity of different materials requires calibration of these sensors using thermocouples. The necessity of using thermocouples as a primary means of measuring temperature led researchers [64, 65] to investigate different ways of positioning the thermocouples inside microwave cavities with minimum interaction. As electric fields cannot penetrate the metallic sheets, thermocouples with metallic sheath's were preferred for temperature measurements. It was also reported that by placing thermocouples (in well grounded metallic sheaths) perpendicular to the electric field, resulted in reliable and accurate measurements [64, 65].

For this study, a platinum-rhodium thermocouple with a platinum sheath was used[20] for measuring temperature. Figure 3.18a shows the $\frac{1}{16}^{th}$ inch stainless steel compression fitting used to provide grounding to the cavity wall. Figure 3.18b shows the top-view of the microwave cavity with the thermocouple positioned perpendicular to the $X-Z$ wall of the cavity (i.e., perpendicular to the electric field, see Figure 3.16).

[20]XPA-P30R-U-062-30-M-SX-6, Omega Engineering

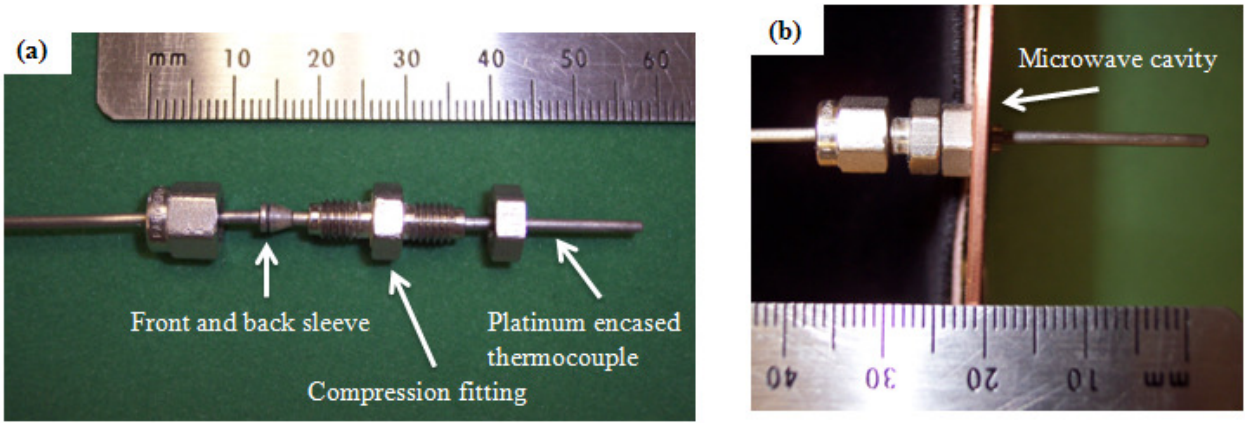

Figure 3.18: Stainless steel compression fitting ($\frac{1}{16}^{th}$ inch) set-up used for grounding the thermocouple to the microwave cavity.

The sintering runs were governed by monitoring the temperature at the exact location of the thermocouple tip. The temperature variation during microwave sintering was determined to be within a range of ± 10 °C.

3.4 Characterization

3.4.1 Particle size analysis

The 8YZ particulate size was determined through sieve analysis, a particle size analyzer[21], and microscopic imaging. The powder samples were selected from the bottom, center, and top regions of the container to provide a better representation of the bulk powder.

Seiving: The aperture opening for the seives[22] selected for this study were in the size range of

[21] Horiba Model no: LA-950
[22] DUAL Manufacturing. Co., Inc.

300, 250, 150, 90, 75, and 53 μm. The as-received powder was allowed to pass through sieves with decreasing mesh size. The size distribution was then determined by measuring the weight percentage of material retained on the mesh for a given size.

Particle size analyzer: This instrument[23] determine's the particle size distribution by monitoring the scattering of a laser beam by particles in a liquid stream. Dispersion of the particles was essential for determining the true particle size. This was accomplished through simultaneous application of ultrasonication and mechanical agitation.

Microscopic imaging: The particles were directly observed under a Scanning Electron Microscopy (SEM)[24] and their size was determined by measuring the diameter of the particulates using the linear intercept method (see section 3.4.5 [66]).

3.4.2 Density measurements

Bulk densities for all of the sintered samples was measured using the liquid displacement method[25] [67]. The sintered samples were saturated with distilled water by boiling them for $4\,hr$, followed by a $24\ hr$ soak period. Equation 3.3 was used to calculate the bulk density (ρ_b).

$$\rho_b = \frac{W_D}{V_b} = \frac{W_D \times \rho_L}{W_s - W_{ss}} \tag{3.3}$$

[23]LA950, Horiba Instruments Inc.,
[24]LEO 1550, Carl Zeiss
[25]ASTM C 20

where, V_b is the bulk density, W_D is the weight of the dry sample, W_s is the weight of the saturated sample, W_{ss} is the weight of the saturated sample when submerged in liquid, and ρ_L is the density of water.

The bulk density of the sintered pellet was then expressed as the ratio of bulk density to the theoretical density[26] (ρ_t); this is given by

$$\% \quad \text{Theoretical} \quad \text{density (TD)} = \frac{\rho_b}{\rho_t} \times 100 \tag{3.4}$$

The theoretical density of 8YZ is $5.96 \ \frac{g}{cc}$; this value was determined by matching the X-ray diffraction[27] pattern of the as-received powder with the diffraction file index[28]. The bulk density of the unsintered (or green) pellets was determined by dividing the weight of the sample by its volume (that was measured geometrically), as opposed to using Equation 3.3. This procedure was used because the unfired pellets disintegrated during water saturation.

3.4.3 Dielectric property measurements

The variations in relative effective dielectric loss with respect to temperature was measured by Microwave Properties North[29] using a cavity perturbation technique [68].

[26]Density of a material with zero microstructural porosity
[27]X'PERT PRO, PANanalytical Inc.,
[28]PDF index number: 00-030-1468
[29]Microwave Properties North, Ontario, Canada

3.4.4 Cermography

A standard cermographic procedure [69] was adopted for attaining the surface quality desired for revealing structural details. Longitudinal sections of each sample were obtained using a diamond blade saw[30]. These samples were mounted into epoxy resin which was allowed to cure for 9 hr. These samples were subjected to a series of coarse polishing through a standard progression of SiC papers (180, 320, 400, 600, and 1000 grits). Fine polishing was done using 15, 6 and 1 micron diamond suspensions in oil. The grain structure on polished samples was revealed by thermally etching at temperatures 150 °C below the normal sintering temperatures [69].

3.4.5 Grain size determination

A thin layer ($\sim$10 nm) of gold-palladium was coated onto the etched sample for improving the conductivity of the surface for SEM imaging. At least five images were taken from different regions of the sample. These images were used for determining the grain size. A mean lineal intercept method was used to estimate the average grain size, in accordance with ASTM E-112 [66]. Each micrograph was divided by drawing ten equally spaced test lines. The total number of grain boundary intercepts with the test line was estimated and the average grain diameter was calculated using the following equation.

$$\bar{l} = \frac{L_T}{N_l} \tag{3.5}$$

[30]Buehler Isomet 1000

where $\bar{l}$ is the *mean lineal intercept* in μm (is represented as average grain size), L_T is the length of the test line, and N_l is the number of intercepts per unit test line. Four sets of ~ 400 intercepts were counted for each micrograph before estimating the average grain size.

3.4.6 Hardness testing

Hardness testing was performed according to ASTM C 1327 [70]. The testing conditions included the application of a $10\,N$ load using a Vickers-indenter[31] for a period of $5\,s$. The hardness values were determined using the following equation.

$$HV = \frac{0.0018544 \times P}{d_l^2} \tag{3.6}$$

where, HV is the vickers hardness number in GPa, P is the load in N and d_l is the length of the diagonal in mm. For each result, at least 15 indentations were carried out and the mean values recorded.

[31]LECO LV 700 AT Micro-indendation Hardness Machine

Chapter 4

Results and Discussion

This chapter presents the results from the experimental setup (as outlined in Chapter 3) and draws the best possible implications from these observations. The statistical measures used for analyzing the data are presented in Appendix C. Section 4.4 examines the microwave sintering behaviour of 8 mol % Y_2O_3-stabilized ZrO_2 relative to conventional sintering. It was observed that microwave sintering resulted in a 300 °C reduction in processing temperatures (compared to conventional sintering) and this difference is not due to the inaccuracy in temperature measurement. Even though these results satisfy the need for the application (low temperature sintering of inert matrix material using microwaves), it is important to understand why there is an enhancement in densification during microwave sintering. Section 4.5.2 and 4.5.1 evaluate the variation in activation energy and driving force. These results were then used to understand the effect of microwaves on the overall enhancement in flux during microwave sintering.

4.1 Powder characterization

The measurement of the particle size and their distribution is shown in Figure 4.1. SEM imaging, sieve analysis and particle size analysis were used to characterize the 8YZ powders. Figure 4.1a shows the SEM imaging of the as-received powder. It can be observed that the starting powders mainly consisted of agglomerates/granules of $\sim$50 μm in diameter. The inset in Figure 4.1a shows that the average particle size within the agglomerates were less than 0.5 μm. Particle size analysis from the SEM observations were confirmed through sieving and laser scattering techniques.

Figure 4.1b is a plot between the weight fractions of particles (agglomerates) on each screen vs. the sieve size. As can be seen in Figure 4.1b the average agglomerate size was $\sim$50 μm. As the lower limit of measurement with sieves was $\sim$20 μm, a laser scattering technique was used to determine the actual particle size. The results from particle size analysis are shown in Figure 4.1c. This plot illustrates the count fractions of particles vs. the particle size diameter. It shows that the particles within the agglomerates were less than 0.3 μm.

4.2 Compaction behavior

Uniaxial and Isostatic pressing are the two most common techniques used for consolidating dry ceramic powders. Section 3.2 has shown that the pressing technique (uniaxial vs. isostatic) has a major effect on the final sintering behavior. The sintering of isostatically pressed 8YZ pellet

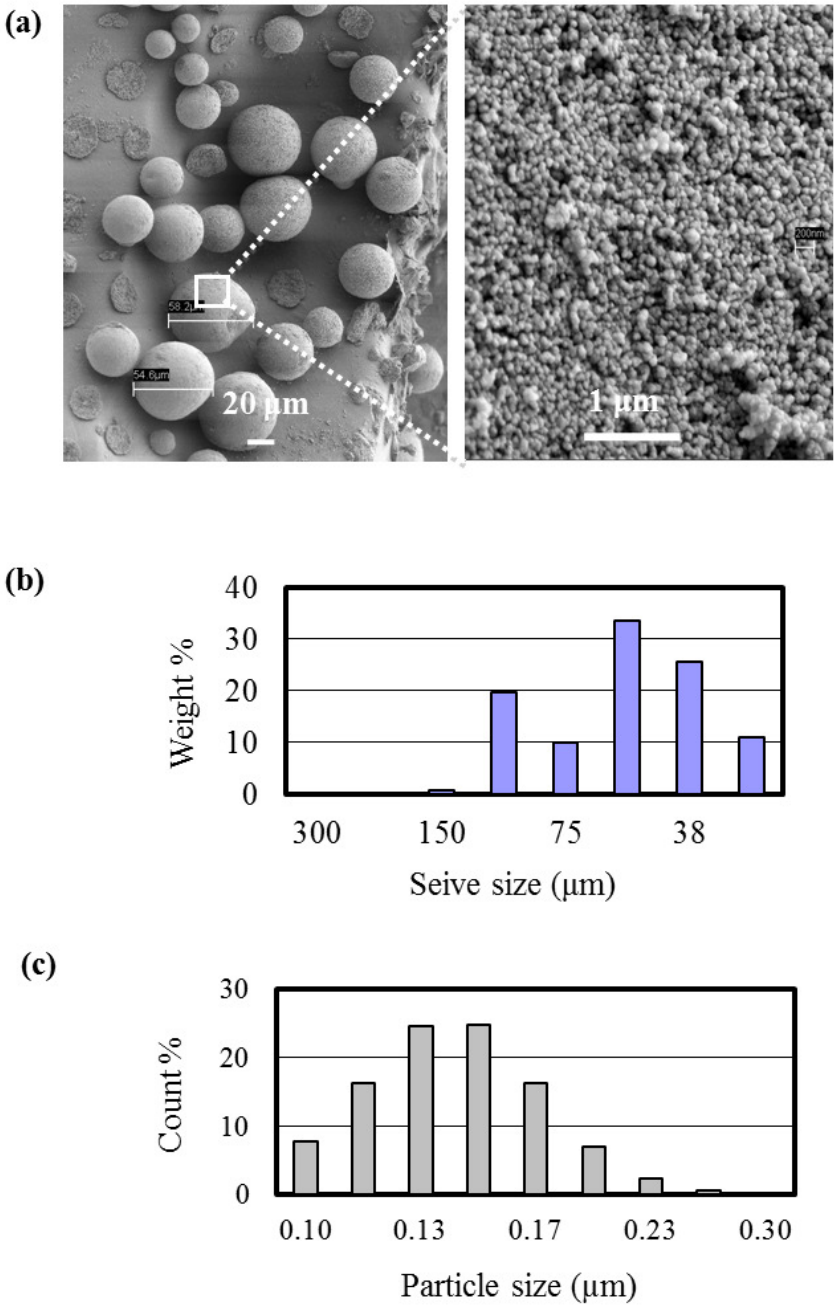

Figure 4.1: (a) SEM imaging of 8YZ powder; particle size distribution through (b) sieve analysis and (c) particle size analysis (laser scattering).

showed little or no cracking (as compared with uniaxial pressing). This is due to homogeneous packing of particles in the green body (unfired pellet) with isostatic pressing. Further understanding on compaction behavior of 8YZ powders with respect to pressure in isostatic machine is shown in Figure 4.2.

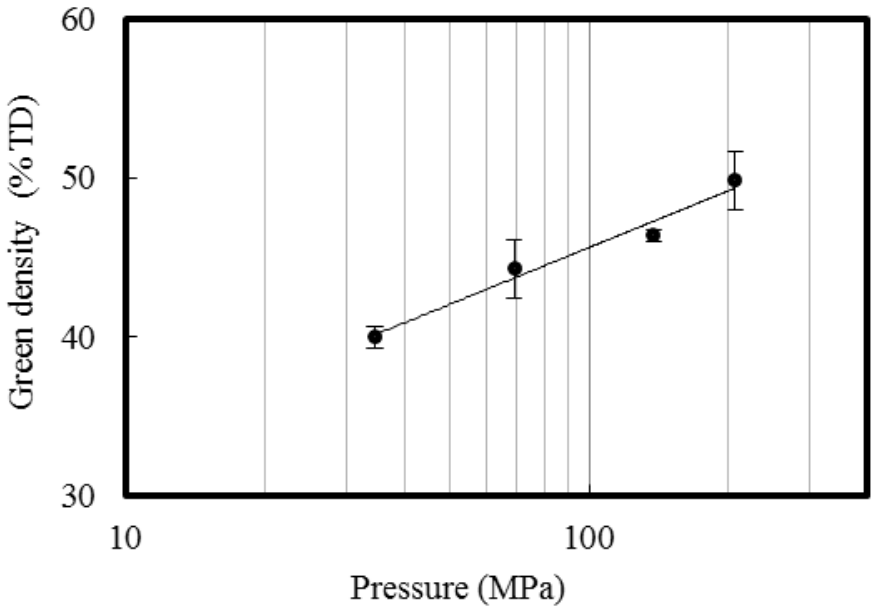

Figure 4.2: Effect of isostatic pressure on green density of 8YZ pellets. The bars on each data point represent a 95 % confidence interval surrounding the mean value (solid circle).

It can be observed that the increase in pressure resulted in an increase in green density. This is due to the inter-particle rearrangement and fracture of agglomerates with the application of pressure. Gibson et al [71] observed a similar behavior for 8YZ powders that were produced through a co-milling technique. Due to a limitation with the operating pressure of the isostatic machine, the green pellets selected for this study were 46 % of the Theoretical Density (TD).

4.3 Effect of temperature on dielectric properties

Figure 4.3a shows the temperature dependence of ε''_{eff} and ε' for 8YZ at 2.45 GHz microwave frequency. These values were measured on a sample that was undergoing sintering. This set-up accounted for the changes in ε''_{eff} and ε' values with a continuous change in volume (bulk) associated with sintering. It can be observed that the ε''_{eff} value increased exponentially; whereas, ε' increased at temperatures greater than 1000 °C. Above 200 °C this material starts to absorb microwaves. Below 200 °C either a high electric field was required or preheating the sample using another source of heat was needed to ensure a reasonable raise in temperature with time.

Figure 4.3b shows the penetration depth (see Equation 2.33) of microwaves into the 8YZ pellet as a function of sintering temperature. It can be observed that at 200 °C the penetration depth was about 3 m. This increase in D_p is due to the lack of microwave absorption by 8YZ below 200 °C. Above 200 °C the depth of penetration of the microwaves started to decrease (see Figure 4.3b). This suggests that at temperatures above 200 °C the 8YZ pellet starts to absorb microwaves and converts it into heat. At higher temperatures > 1000 °C, the D_p value decreased to 3 mm (see inset Figure 4.3b). The penetration depth, D_p, represents the depth at which 37 % of the microwave power has been absorbed by the sample. The sample dimensions used in this study (dia. = 12 mm $\times$ ht. = 12 mm) allow for most of the power to be absorbed by the sample in a fairly uniform manner. Evidence for this is discussed in Section 4.4

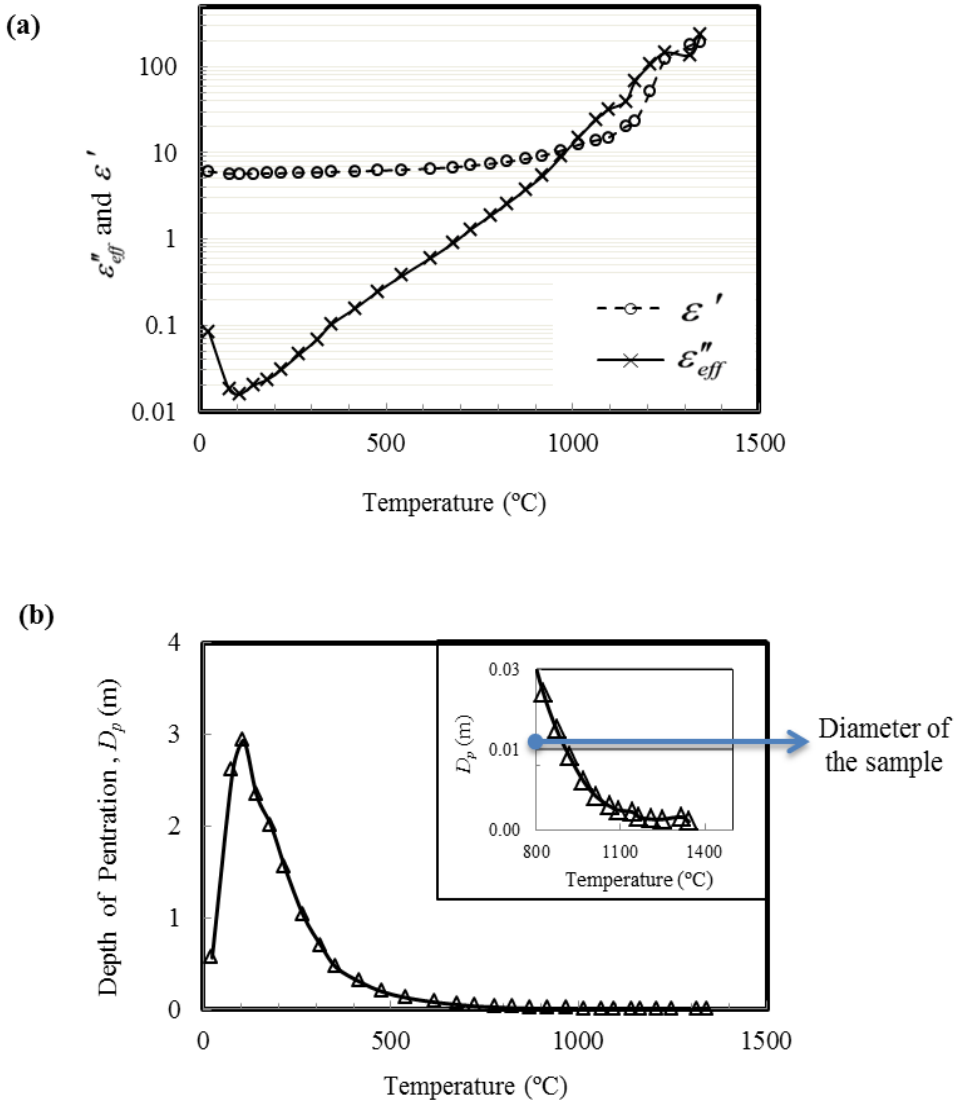

Figure 4.3: (a) Variation in the relative effective dielectric loss (ε''_{eff}) and relative dielectric constant (ε') and (b) depth of penetration (D_p) with temperature for 8YZ at 2.45 GHz frequency.

4.4 Verification of microwave enhanced densification

One of the goals set-forth for this study was to reproduce the enhanced densification reported in the literature (with microwave sintering) eliminating the possibility of inaccuracy in temperature measurement. For this study, a metallic sheathed B-type thermocouple was used to monitor the temperature. Proper care was taken to position the thermocouple (see Figure 3.18) in order to avoid any interference with the microwave field. To ensure that the measured temperature is the actual temperature of the sample and not the air in the furnace, the thermocouple was placed in close vicinity ($\sim 3\ mm$) of the sample. The following section outlines the procedure adopted for validating the temperature measurement.

Figure 4.4a shows the variation in the temperature recorded by the thermocouple when the microwave was cycled ON and OFF. It can be seen that when the microwave field is cycled *on* and *off* there were no sudden large discontinuities in the temperature measurement; this indicates that the microwave field has no or minimum effect on the thermocouple. If the thermocouple were absorbing the microwave or experiencing arching due to the microwave field, a sharp spike in temperature would have been observed. This phenomena is observed with un-grounded thermocouples and is shown in Figure 4.4b. The decrease in temperature when the microwave field has been turned *off*, as shown in Figure 4.4a, was attributed to the normal cooling experienced by the sample. When the field is turned back *on* the sample starts to heat again and this is reflected in the thermocouple reading. This confirms that there was no interaction between thermocouple and the microwave field during sintering studies in the microwave furnace.

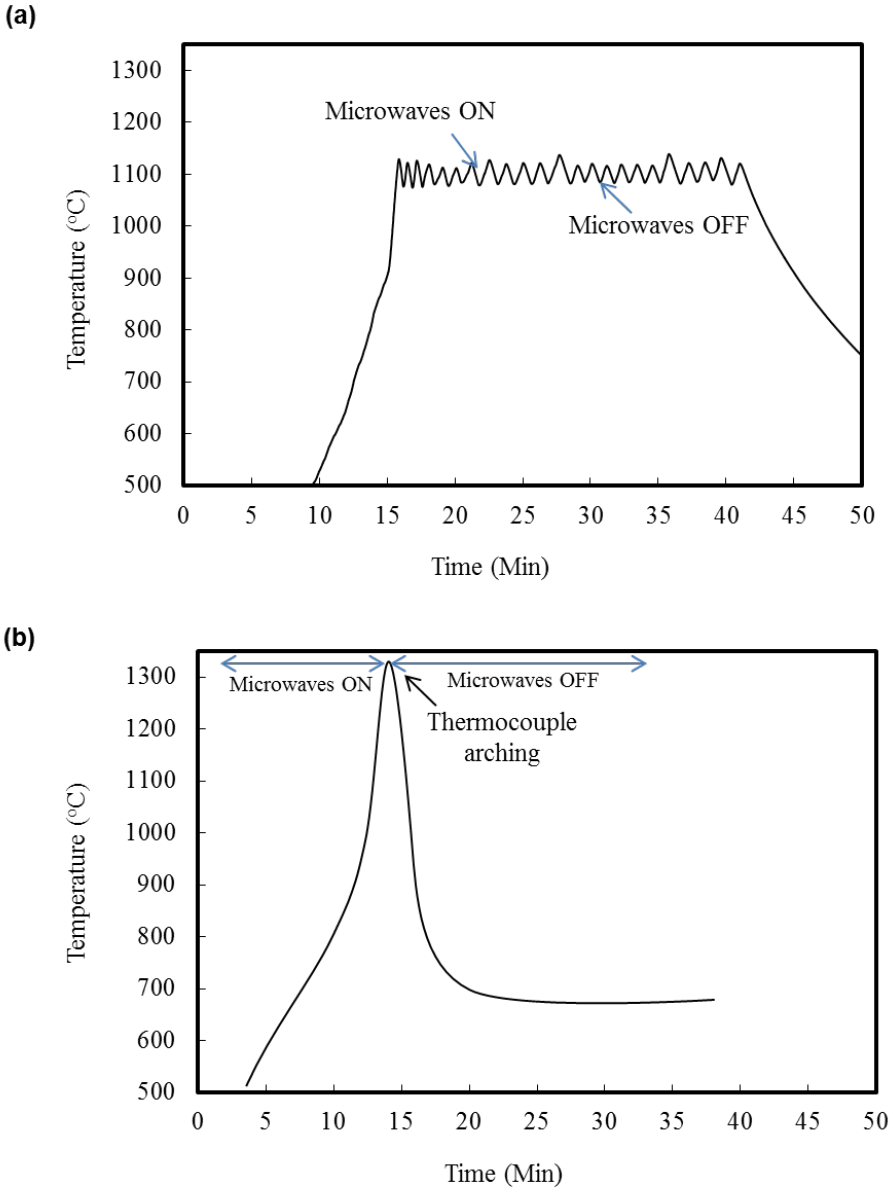

Figure 4.4: Temperature-time profile recorded by a Platinum-Rhodium thermocouple with ON-OFF cycling of microwave power for a (a) grounded thermocouple and an (b) un-grounded thermocouple. Data collected from the multimode microwave system.

Expansion of standard materials is a classic way of representing temperature. For this study a 99.99 % dense alumina was selected as a standard material for validating the thermocouple measurements in the microwave furnace. The expansion of alumina with respect to temperature is measured using the microwave dilatometer that was specifically built for this study (for details see Section 3.3.6). Without altering any of the experimental conditions, the expansion of alumina is recorded using conventional heating. These results are shown in Figure 4.5.

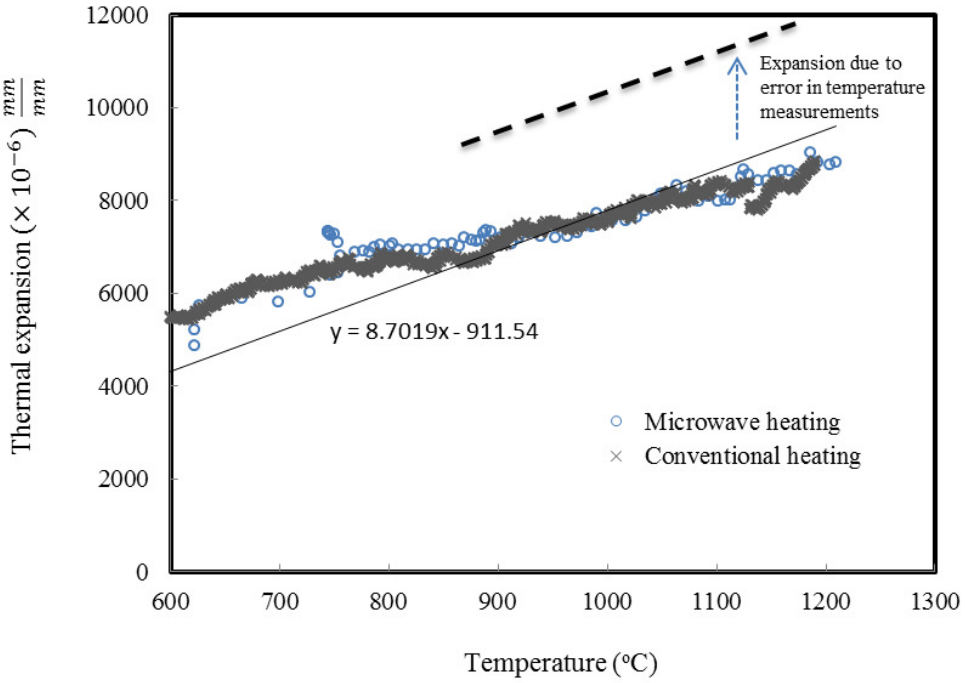

Figure 4.5: Thermal expansion readings of a standard material (alumina) with microwave heating, and conventional heating confirms the accuracy of thermocouple measurements in microwave furnace.

It can be observed that irrespective of the heating technique (conventional or microwave) the expansion of alumina remained the same with respect to temperature. In the present study, a 300°C reduction in temperature was observed for direct microwave heating to achieve the same density as

conventional heating. If the temperature readings during microwave heating were offset by 300°C, the expansion values should have fallen along the dashed line (see Figure 4.5); this confirms that the thermocouple used for measuring temperature in the microwave furnace was accurate.

The isothermal sintering behavior of 8YZ was examined using direct microwave and microwave hybrid heating, and the results were compared with conventional heating. The densification behavior of 8YZ is shown in Figure 4.6.

All of the sintering runs had a constant heating rate of 20 $\frac{^{\circ}C}{min}$ with a soak time of 20 min (see Figure 3.7 for details). It can be observed from Figure 4.6a that at temperatures below 1400 °C, microwave sintering resulted in higher density values than conventional sintering. Near full densification (97 % TD) was obtained at 1100 °C using direct microwave sintering. It required 1300 °C to reach full densification in a microwave hybrid furnace and 1400 °C in a conventional furnace. The actual picture of these pellets is shown in Figure 4.6b. It can be observed that direct microwave sintered pellet showed near-complete sintering (97 % TD), while conventionally sintered pellet (48 % TD) was similar to green pellet (46 % TD).

As can be seen in Figure 4.6a the densification curves for 8YZ sintered using microwave hybrid heating lies in between conventional and direct microwave heating. This is an indirect indication that the presence/absence of the electric field, with 2.45 GHz frequency, has an effect on densification. The conventional heating technique has no electric fields (with 2.45 GHz frequency) associated with it, while direct microwave heating (performed in singlemode microwave cavities) has electric field intensities higher than microwave hybrid heating (for details see Section 3.3.3). This may be the reason why the densification behavior associated with conventionally sintering

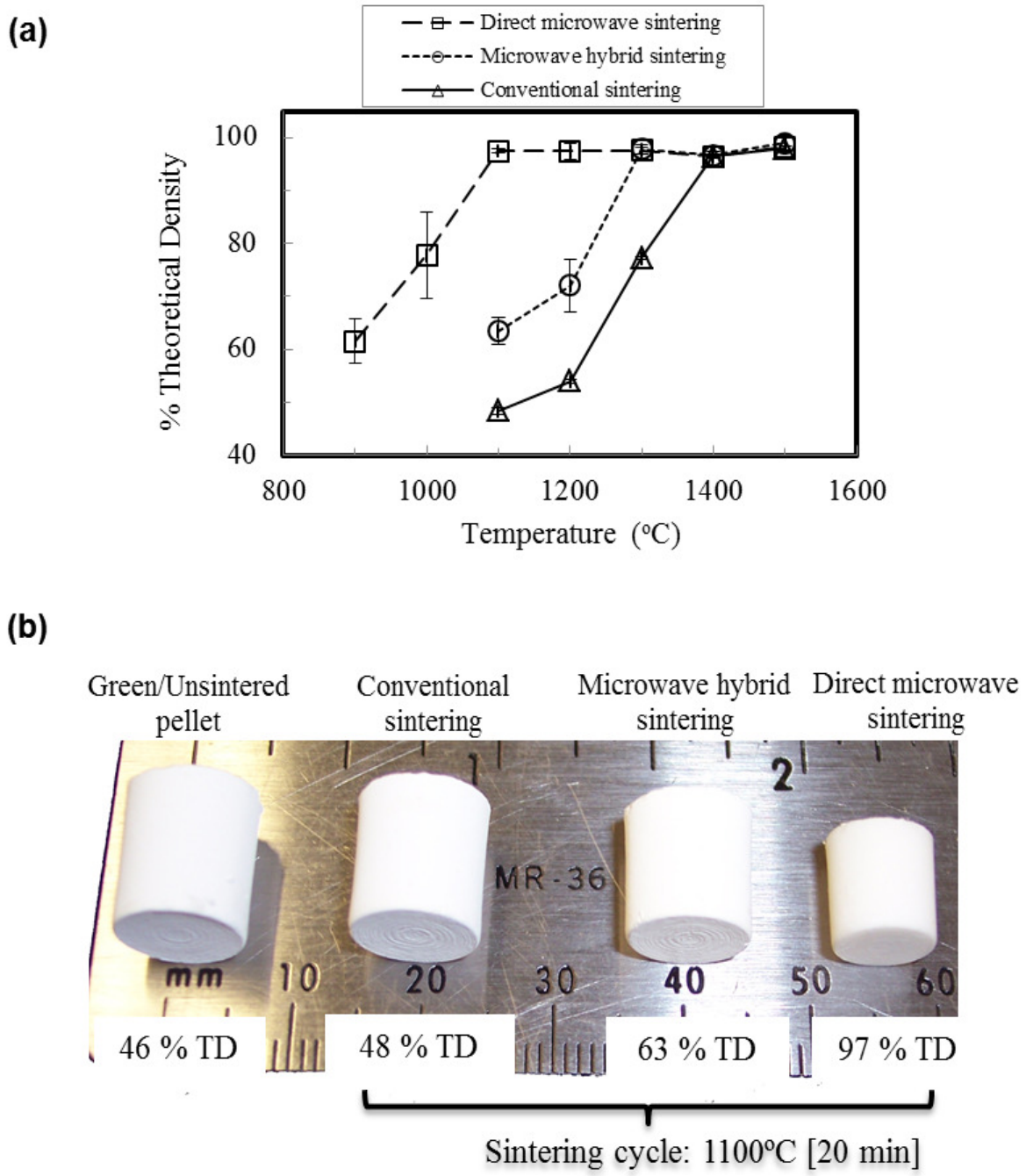

Figure 4.6: (a) Densification behavior of 8YZ with direct microwave sintering, microwave hybrid sintering, and conventional sintering and (b) Actual picture of green pellet and 1100 °C processed 8YZ pellet. The bars on each data point represent a 95 % confidence interval surrounding the mean value.

(zero electric field) fell below the microwave hybrid sintering profile; whereas, the direct microwave sintered density lines fell above the microwave hybrid sintering profile (see Figure 4.6a). The following paragraphs will present a comparison between the sintering data collected for this study and the data published in the literature.

Conventional sintering of 8YZ from Tosoh Corporation has been well-studied. Gibson et al [71] observed a 95 % TD at a temperature of 1300 °C. For this study, a 77 % TD was observed for a sintering temperature of 1300 °C. This difference in resulting densities is attributed in large part to the differences in soaking time used for this study (20 min) and Gibson's [71] work (100 min).

Janney et al [20] have used silicon carbide suceptors for microwave hybrid sintering of 8YZ. Their data show that at temperatures less than 1300 °C the densification-curves shifted towards lower temperatures by 150 °C as compared to conventional sintering. Samuels and Brandon [49] have used zirconia fiber packed in an alumina vessel as a suceptor. This setup resulted in a 80 °C difference in sintering temperature at 1300 °C. In the present study, the susceptors used for microwave hybrid sintering (performed in multimode) were made of zirconia and alumina cement. These heating conditions showed a 100 °C shift in the densification curves towards lower temperatures relative to conventional heating. Samuels and Brandon's work is in close agreement with the observation made in this study, which could be due to the similarity in the susceptor designs.

Only a few investigators have studied the direct microwave sintering of ceramics. Goldstein et al used a multimode microwave cavity and Charmond et al used a single mode microwave cavity similar to the one used for this study. Goldstein et al [53] observed that direct microwave sintering of 3 mol % yttria-zirconia resulted in a 100 °C reduction in temperature (for full densification)

when compared with conventional sintering. Charmond et al [52] studied the direct microwave sintering behavior of 2 mol % yttria-zirconia and found a 275 °C difference in sintering temperature compared with conventional sintering (to achieve ∼95 % TD). The results of the work reported in the present study are in good agreement (a difference in 300 °C) with that of Charmond et al [52] and not with Goldstein et al [53], possibly due to the differences in the experimental design. It is well known that the magnitude of the electric field intensity per mode is higher in single mode microwave cavities than multimode microwave cavities. Lower magnitudes of electric fields may have resulted in a 100 °C difference (observed in Goldstein et al [53] study) in sintering temperature as opposed to 275 °C observed in Charmond et al's [52] work and 300 °C observed in the current study.

Furthermore, the microwave hybrid dilatometer developed for this study was used to monitor the densification behavior (of 8YZ) as a function of applied electric field (associated with microwaves). Figure 4.7 shows the densification behavior (of 8YZ) as a function of electric field intensity, for a heating rate of 20 $\frac{^{\circ}C}{min}$. It can be observed from Figure 4.7 that for a given temperature the increase in the magnitude of the applied electric field is accelerating densification. This result is in agreement with the Wroe and Rowley's [22] observation; they have observed a shift in linear-shrinkage curves to lower temperatures with the increase in applied microwave power. This study supports Wroe and Rowley's observation that the electric field component of the microwaves is responsible for enhancing densification. A similar observation was made by Cologna et al [72] in the presence of a D.C electric field. They have studied the sintering behavior of zirconia (3 mol % yttria) at various intensities of D.C electric fields. The field intensity used in Cologna's [72]

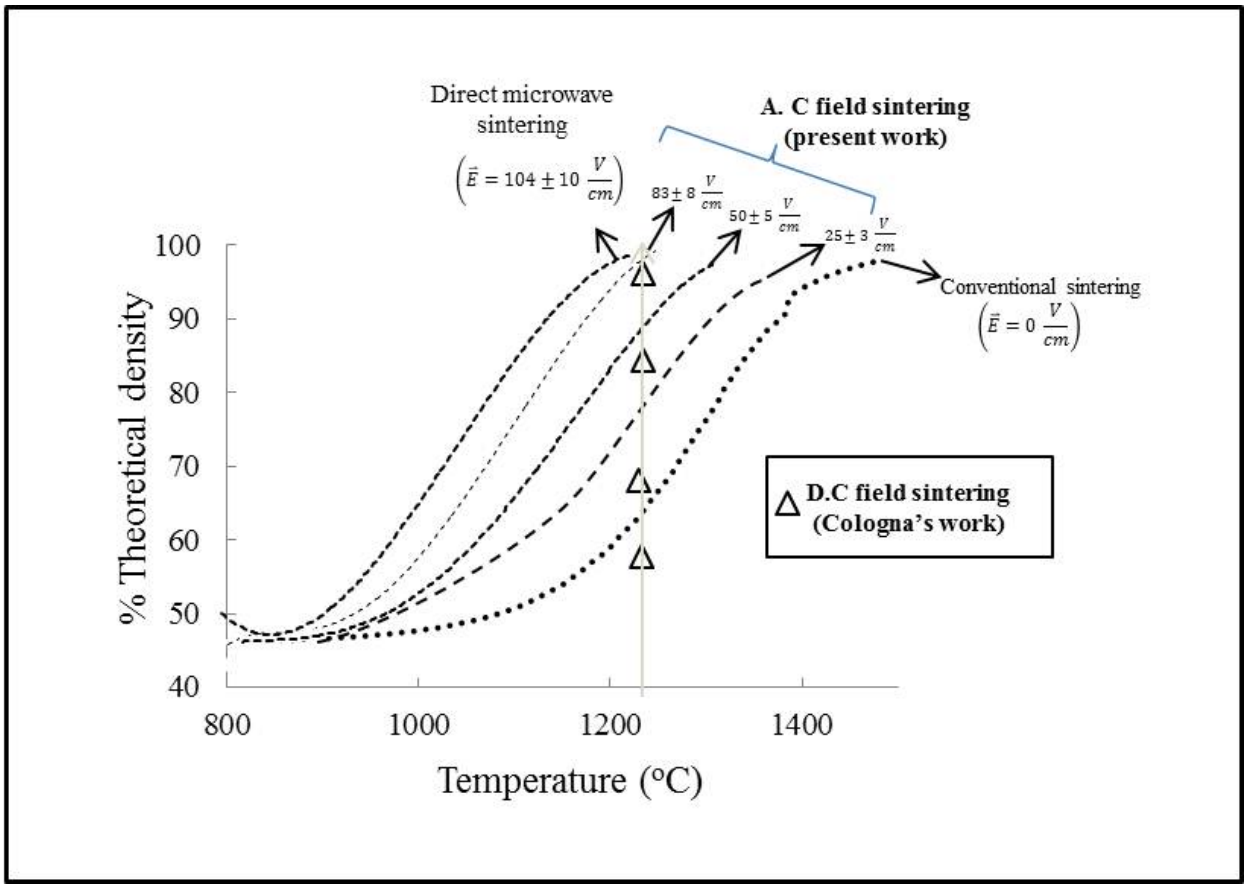

Figure 4.7: Theoretical density versus temperature curves for 8 mol % yttria-zirconia at different values of applied electric fields (oscillating at 2.45 GHz).

work were similar to the ones used in this study (0 to 120 $\frac{V}{cm}$). As a comparison Cologna's [72] results were overlaid with the data obtained for this study (see Figure 4.7). It can be observed that Cologna et al's work and the present study indicates that the presence of electric fields (be it static or oscillating) enhances densification during sintering.

Figure 4.8 shows the variation in grain size with temperature on the 8YZ sintered pellets processed using direct microwave, microwave hybrid and conventional heating (shown in Figure 4.6). The grain size values recorded for direct microwave sintering were between 0.64 μm (at 1100 °C) and 8.86 μm (at 1500 °C). For microwave hybrid and conventional sintering, an appreciable grain structure could only be seen at temperatures greater than 1200 °C. The structural integrity of the conventionally sintered samples below 1300 °C was poor as they did not survive the sectioning and grinding stage.

In many applications, smaller grain-sized ceramics are usually preferred as they exhibit better properties [32]. However, for fuel pellets large grain sizes are preferred to smaller grain sizes as they have been shown to decrease the fission gas release rate during irradiation [73]. This delay essentially decreases the rate of swelling of the fuel during irradiation. Studies on conventional sintering methods have shown that larger grain sizes were obtained only at high sintering temperatures (> 1500 °C) [54]. Figure 4.8 shows that by adopting single mode microwave sintering, larger grain sizes could be obtained at lower temperatures.

Figure 4.9 shows a polished sample and the SEM images of the grain structure for a 97 % dense sample. These samples were processed using direct microwave, microwave hybrid and conventional heating. As can be seen in Figure 4.9a, various locations were selected for measuring

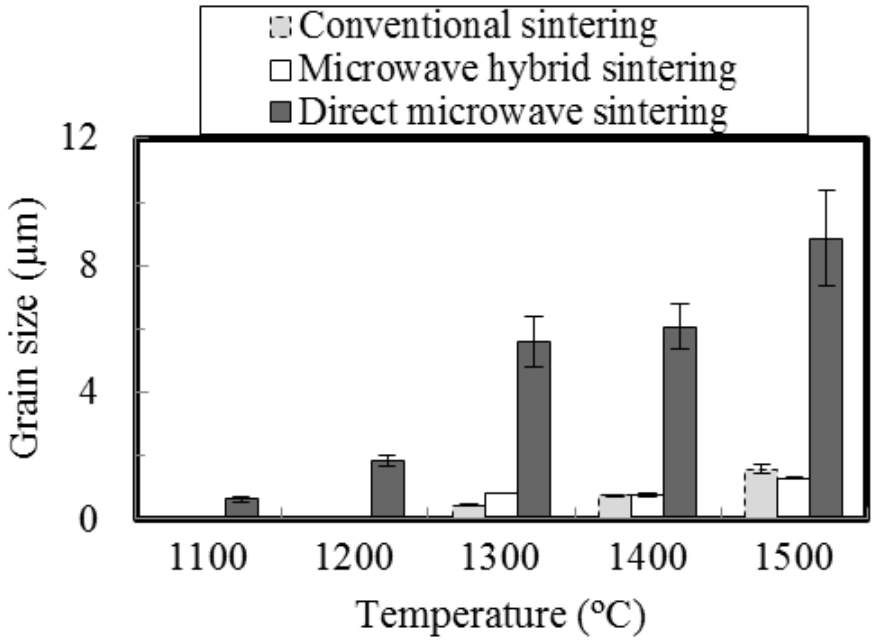

Figure 4.8: Change in grain size with temperature during direct microwave sintering, microwave hybrid sintering and conventional sintering. The lines on each bar represent a 95 % confidence interval surrounding the mean value.

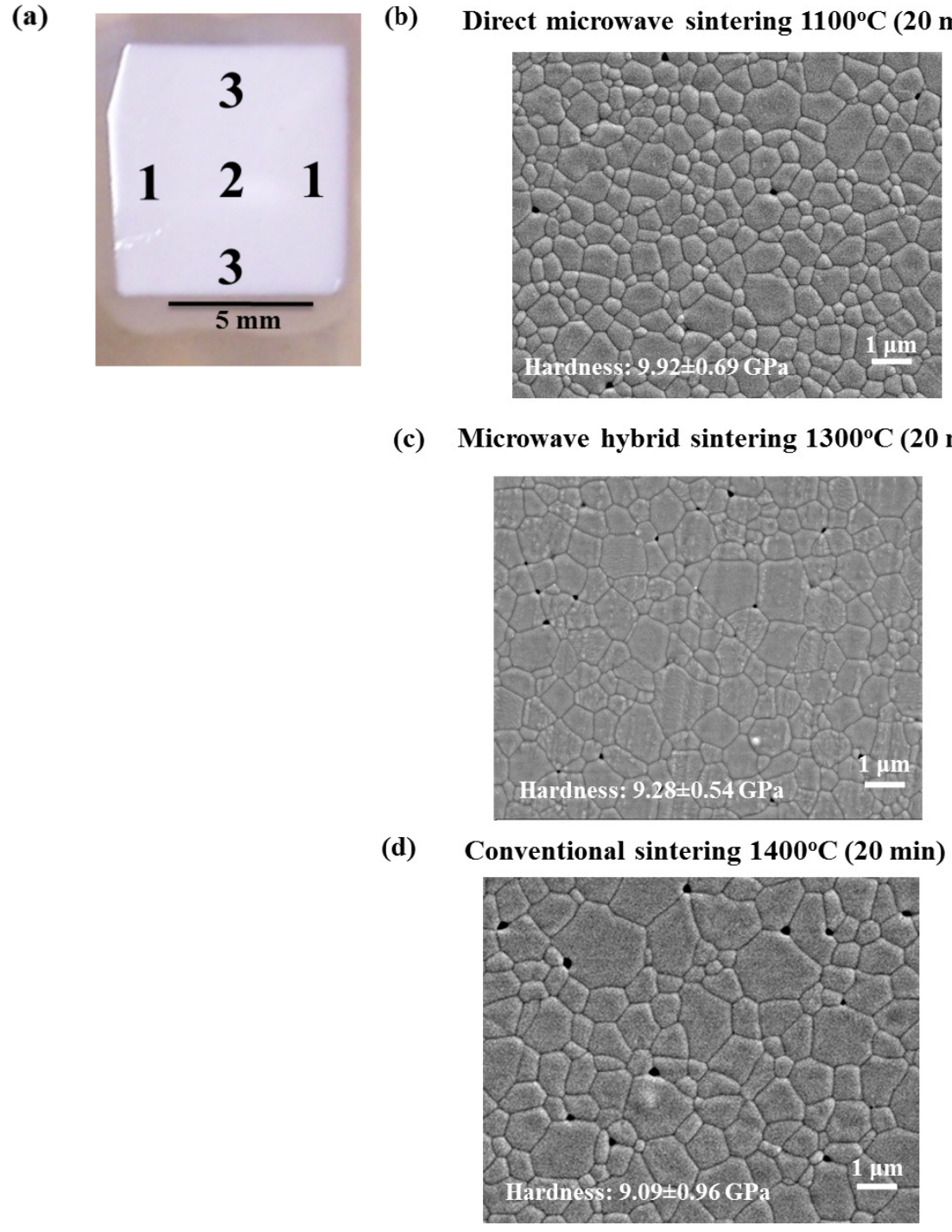

Figure 4.9: (a) Polished sample showing various locations selected for property testing, and Scanning electron microscopy images of 97 % dense 8YZ: (b) direct microwave, (c) microwave hybrid and (d) conventionally sintered samples.

grain size and hardness measurements (for testing conditions see Section 3.4.6). The variation in hardness and grain size values along the interior and the exterior regions (see Figure 4.9a) were minimal; this observation confirms that the samples experienced a uniform distribution in processing temperature. Figures 4.9b and 4.9c show similarities in the grain structure (0.7 μm) and the resulting hardness ($\sim$9 GPa) when compared with Figure 4.9d. These results confirm that the reduction in processing temperatures observed during direct microwave sintering or microwave hybrid sintering did not alter any of the resulting microstructures or the properties.

In summary, there have been reports in literature where microwave processing has enhanced the rate of sintering in comparison to conventional processing. One of the major criticisms reported in literature is the inaccuracy in temperature measurements in microwave field. This section has substantiated that enhancements in microwave sintering do occur and that they are not due to inaccuracies in temperature measurement. Thus the first goal of this study has been achieved.

4.5 Role of flux on microwave enhanced sintering

The second goal of this research was to understand which of the terms in the flux equation, if any, are responsible for the enhancement in microwave sintering compared to conventional sintering. In order to achieve this goal, (1) the magnitude of driving forces due to surface free energy and electric field were estimated theoretically; (2) the activation energy (transport coefficient) was measured using two different methods of sintering, isothermal and non-isothermal, involving three independent experimental procedures.

4.5.1 Role of driving force

It can be observed from Equation 4.1 that sintering as represented by the change in density or linear shrinkage is controlled by three independent terms, the transport coefficient, the driving force and the concentration of diffusion species. The concentration, c, is typically considered to a constant depending on the temperature and impurity levels.

$$\frac{\Delta\rho}{\rho} \approx \left(\frac{\Delta L}{L_\circ}\right)^3 = -\Bigg(\underbrace{\overbrace{D_\circ \exp\left(-\frac{Q}{RT}\right)}^{\text{Transport Coefficient}}\overbrace{\left(\frac{\gamma_{sv}}{n}\frac{dA}{dx} + z_i F \overrightarrow{E}_{rms}\right)}^{\text{Driving Force}}\frac{c}{RT}}_{\text{Flux}} \overbrace{\frac{2\pi V_m x^2}{a^3}}^{\text{Material Constants}}\Bigg)^{\frac{3}{2}} t^{\frac{3}{2}} \tag{4.1}$$

In the above equation the electric field driving force consists of the following terms: z_i (charge on the ion), F (Faraday constant, $9.65\frac{kJ}{equiv.V}$) and $\overrightarrow{E}_{rms}$ (root mean square of the electric field). In addition to the reduction in surface area driving force Equation 4.1 accounts for the driving force term represented by the electric field. It can be inferred from this equation that it is possible to change the driving force without changing the activation energy, Q.

For example, the driving force due to a reduction in particle size significantly increases the surface area. Although this would increase the densification it should not effect the activation energy. Maca et al [74] have observed an enhancement in densification with sintering nano-sized particles as compared to micron-sized particles. It was also reported that the activation energy for nano-sized powders (237 $\frac{kJ}{mol}$) was one half that of the micron-sized powders (550 $\frac{kJ}{mol}$). However this is attributed to the change in mechanism of diffusion, from volume diffusion to grain boundary dif-

fusion. The reason for the change in mechanism (from volume to grain boundary) with a reduction in particle size is due to the increased number of grain boundaries per unit volume. What is not clear based on Equation 4.1 is why there a decrease in the activation energy when the driving force (due to microwave field) is increased during microwave sintering.

Table 4.1 presents the driving forces due to the surface area and electric field in order to understand the relative differences between their magnitudes. A detailed procedure used for calculating these driving forces are presented in Appendix C. It can be observed from Table 4.1 that the driving force due to the electric fields is comparable to that of the surface area driving force for an electrical field value between 50 and 83 $\frac{V}{cm}$. Figure 4.10 shows the variation in the total driving force (as shown in Table 4.1) as a function of electric field. It can be observed that the increase in the magnitude of the electric fields will result an increase in the total driving force.

Table 4.1: Magnitude of the driving force for surface free energy and several electric fields used in this study.

Driving force, $\times 10^4 \frac{kJ}{mol.cm}$			**Total driving force**, $\times 10^4 \frac{kJ}{mol.cm}$
Surface energy	$\frac{\gamma_{sv}}{n}\frac{dA}{dx}$	2.4	2.4
Electric Field	$\overrightarrow{E}_{rms}$ = 25 $\frac{V}{cm}$	0.9	3.3
	$\overrightarrow{E}_{rms}$ = 50 $\frac{V}{cm}$	1.9	4.3
	$\overrightarrow{E}_{rms}$ = 83 $\frac{V}{cm}$	3.2	4.3
	$\overrightarrow{E}_{rms}$ = 104 $\frac{V}{cm}$	4.0	4.3

In-order to study the role of the electric field driving force on sintering, it is important to understand the role of both the surface free energy and the electric field on transport mechanisms.

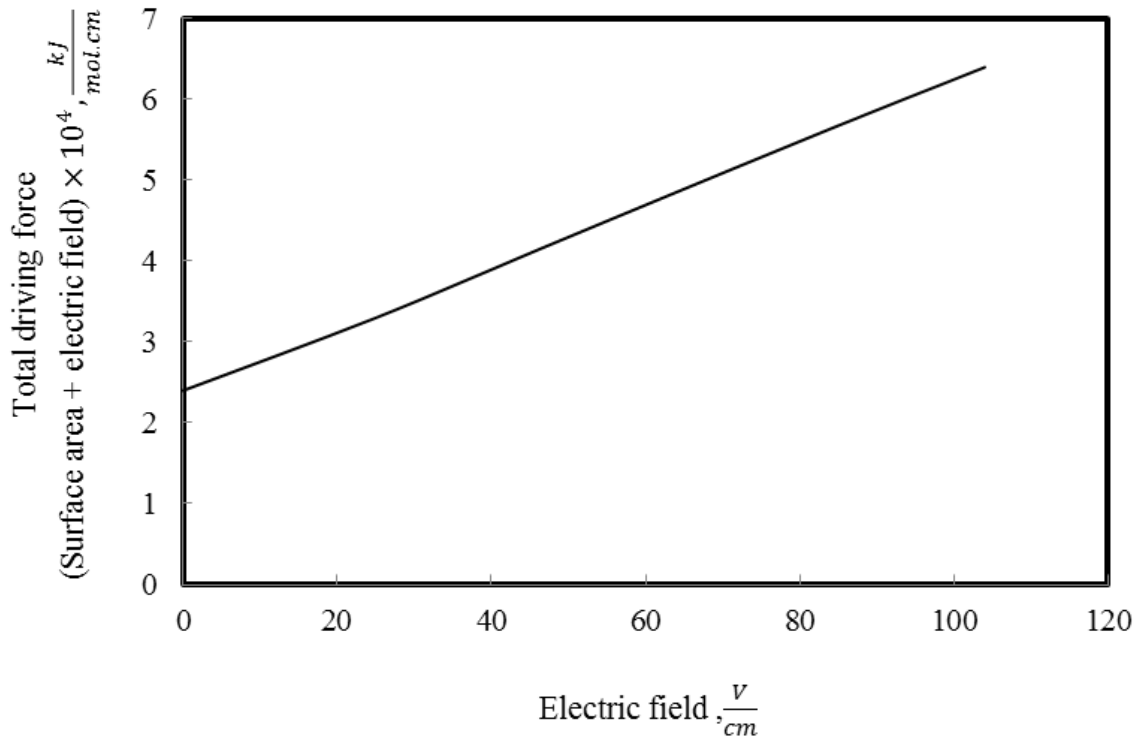

Figure 4.10: Plot of total driving force (calculated using Equation 4.1) as a function of applied electric field.

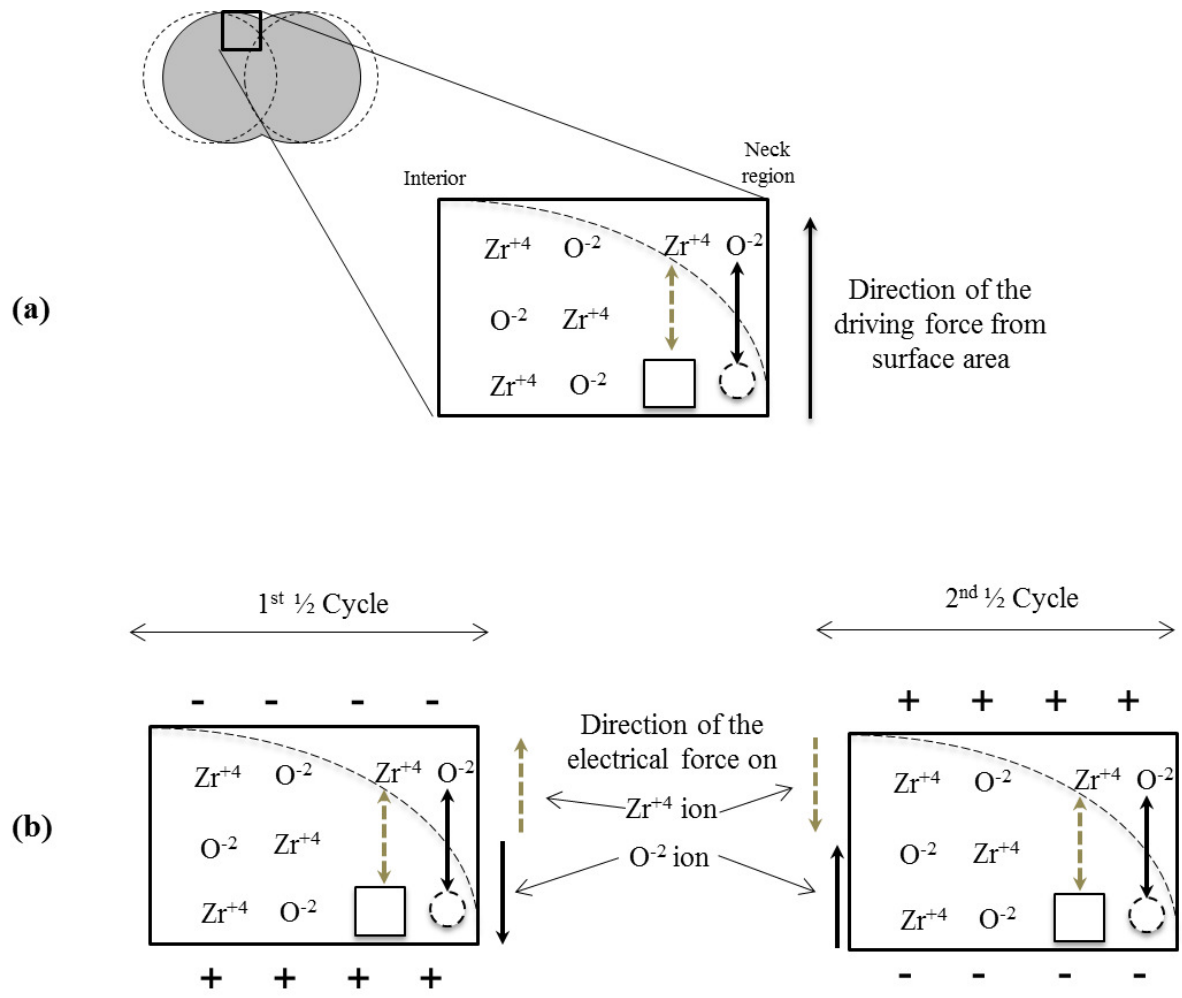

Figure 4.11: Schematic sketch of Zr^{+4} and O^{-2} ion transport during (a) conventional sintering and (b) microwave sintering.

During conventional sintering, the reduction in surface area driving force will cause Zr^{+4} ions and O^{-2} ions to move towards the neck region (see Figure 4.11a). Both Zr^{+4} ions and O^{-2} ions will move along the same direction. As the neck region primarily consists of vacant sites, the movement of these ions to this region occurs largely through a vacancy exchange mechanism (see Figure 4.11a). This will result in the counter flow of vacancies in a direction opposite to the flow

of ions and cause a net shrinkage of a powdered compact.

Figure 4.11b represents sintering in the presence of a microwave field. As the electric field component is oscillating, the direction of the field along the sample would change for every half cycle. It can be observed from Figure 4.11b that during the first half cycle the Zr^{+4} ions are experiencing an additional driving force from the electric field and results in greater mass transport. The change of the electric field during the second half cycle will reverse the direction of Zr^{+4} ion transport. It appears that the electrical driving force from the oscillating electric field is producing equivalent forces in opposite directions and this should not result in an enhancement in flux. However our experimental data and the reports from the literature show that the oscillating electric field does in fact result in enhancement in densification. A possible explanation for enhanced densification other than the driving forces is due to an increase in the transport coefficient term (see Equation 4.1).

The transport coefficient term (see Equation 4.1) consists of a pre-exponential term, $D_\circ$, and an exponential term, $exp(-\frac{Q}{RT})$. The pre-exponential term is a product of materials constants such as, attempt frequency $\nu_\circ$, inter-atomic distance λ, and correlation factor g [75] none of which should be influenced by the microwave field. Therefore, it is assumed that the term $D_\circ$ is unaffected by the microwave field. The next section will address the role of activation energy on transport coefficient.

4.5.2 Role of activation energy on transport coefficient

In the following sections the activation energy was evaluated using three different independent methods. The electric field was also varied while maintaining the same temperature to evaluate its effect on the activation energy. According to Equation 4.1 there should not be an effect. However the data show that the increase in electric field (from 0 to 104 $\frac{V}{cm}$) resulted in a decrease in the activation energy (from 500 to 200 $\frac{kJ}{mol}$).

Conventional sintering

Isothermal method: Figure 4.12a shows the isothermal sintering behavior of 8YZ at three different temperatures. To create the isothermal conditions fast heating rates (50 $\frac{^{\circ}C}{min}$) were used. It can be observed from Figure 4.12a that as the hold temperature increases the time required to reach 90 %TD decreases. The plot between the log of densification rate ($ln\frac{d\rho}{dt}$) with respect to thermal energy ($\frac{1}{RT}$) takes the form of a Arrhenius relation. This is shown in Figure 4.12b. The slope of the line represents the activation energy for sintering 8YZ and this was found to be $\sim$ 437 $\frac{kJ}{mol}$.

Non-Isothermal method: Figure 4.13a shows the non-isothermal sintering behavior of 8YZ at three different heating rates (5 $\frac{^{\circ}C}{min}$, 10 $\frac{^{\circ}C}{min}$, and 20 $\frac{^{\circ}C}{min}$). These curves show a sigmodal behavior; the sintering rate increases rapidly with temperature but then levels off as the sample starts to densify. The rate of densification ($\frac{d\rho}{dt}$) is calculated with respect to temperature from the data collected through dilatometer measurements. Using the CHR method, the densification rates are shown on the Arrhenius plot in Figure 4.13b. The activation energy for sintering 8YZ was found to be $\sim$520 $\frac{kJ}{mol}$. Figure 4.13c applies the MSC concept to density curves (shown in Figure 4.13a) for

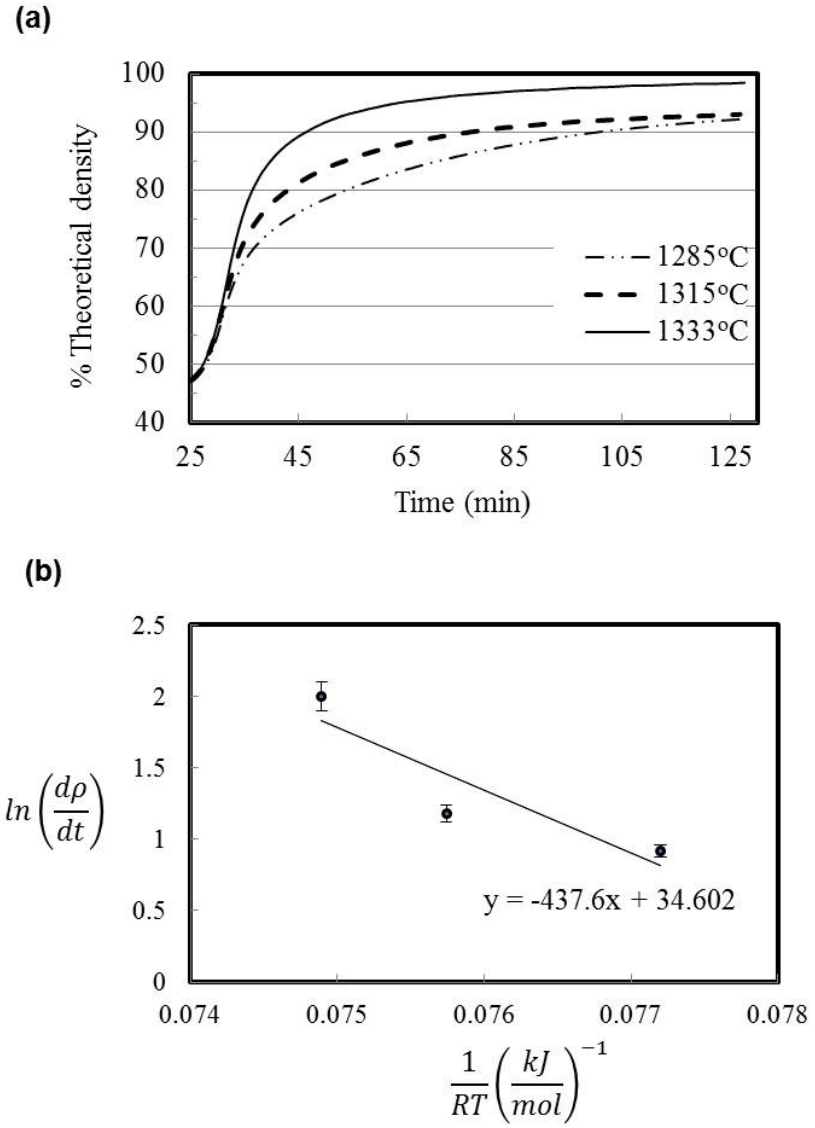

Figure 4.12: (a) Isothermal densification behavior of 8YZ at three different temperatures with conventional heating and (b) Arrhenius plot for 90 % densification determines the activation energy for isothermal sintering of 8YZ. (Bars on each data point represent standard deviation surrounding the mean value)

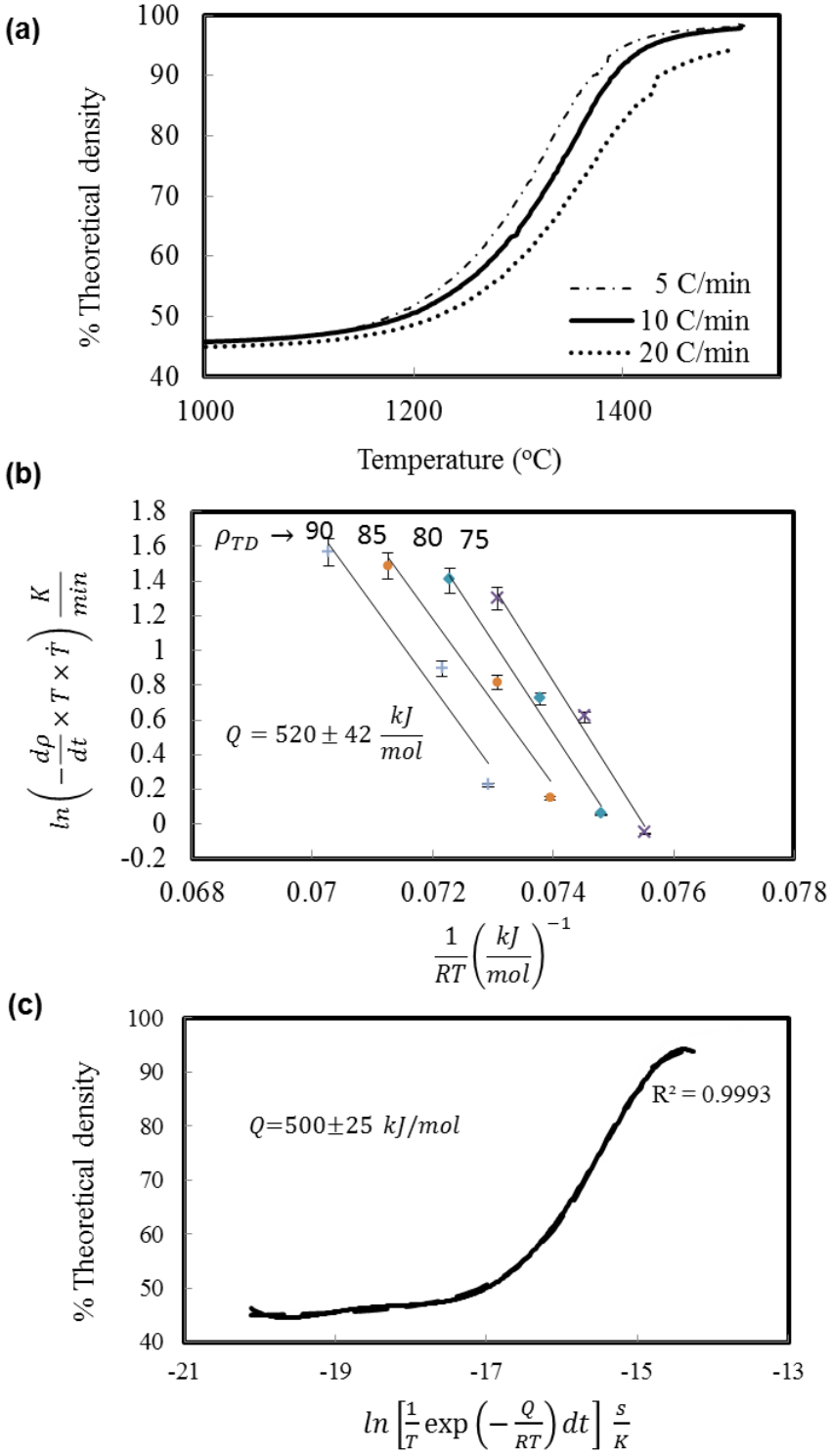

Figure 4.13: (a) Non-Isothermal sintering behavior of 8YZ at different heating rates, (b) Arrhenius plot for measuring activation energy using Constant Heating Rate method, (c) Master Sintering Curve approach for measuring activation energy. (Bars on each data point represent standard deviation surrounding the mean value)

estimating the activation energy. It was observed that a Q value of $\sim$500 $\frac{kJ}{mol}$ results in convergence of the density lines produced at different heating rates. This value (500 $\frac{kJ}{mol}$) is determined to be the activation energy for sintering 8YZ inside a conventional furnace. This is in close agreement with the activation energy value determined using CHR method (520 $\frac{kJ}{mol}$).

Microwave sintering

Isothermal method: Figure 4.14a shows the isothermal sintering behavior of 8YZ at three different temperatures. All of these experiments were conducted in a microwave dilatometer (for details see Appendix B). The value of the electric field required to maintain these temperatures was 107$\pm$10 $\frac{V}{cm}$. The time required to reach 90 %TD was used for constructing the Arrhenius plot (see Figure 4.14b). The activation energy determined through isothermal method for microwave sintering of 8YZ was found to be $\sim$214 $\frac{kJ}{mol}$.

Non-Isothermal method: Figure 4.15a shows the direct microwave sintering of 8YZ at different heating rates. The electric field intensity recorded for these experiments was 104$\pm$10 $\frac{V}{cm}$. The densification curves were used to generate the CHR and MSC plots (see Figure 4.15b and 4.15c). The activation energy required for direct microwave sintering of 8YZ was determined to be 200 $\frac{kJ}{mol}$.

Activation energies have also been measured as a function of electric field intensities (between 83$\pm$8 and 25$\pm$3 $\frac{V}{cm}$). For a given electric field intensity, the sintering experiments were performed at three different heating rates (10 $\frac{^{\circ}C}{min}$, 15 $\frac{^{\circ}C}{min}$, and 20 $\frac{^{\circ}C}{min}$). This is necessary for estimating the activation energy using MSC method. The data was then used for studying the change in activation energy with the electric field intensity. Figure 4.16 shows the MSC curves constructed for estimat-

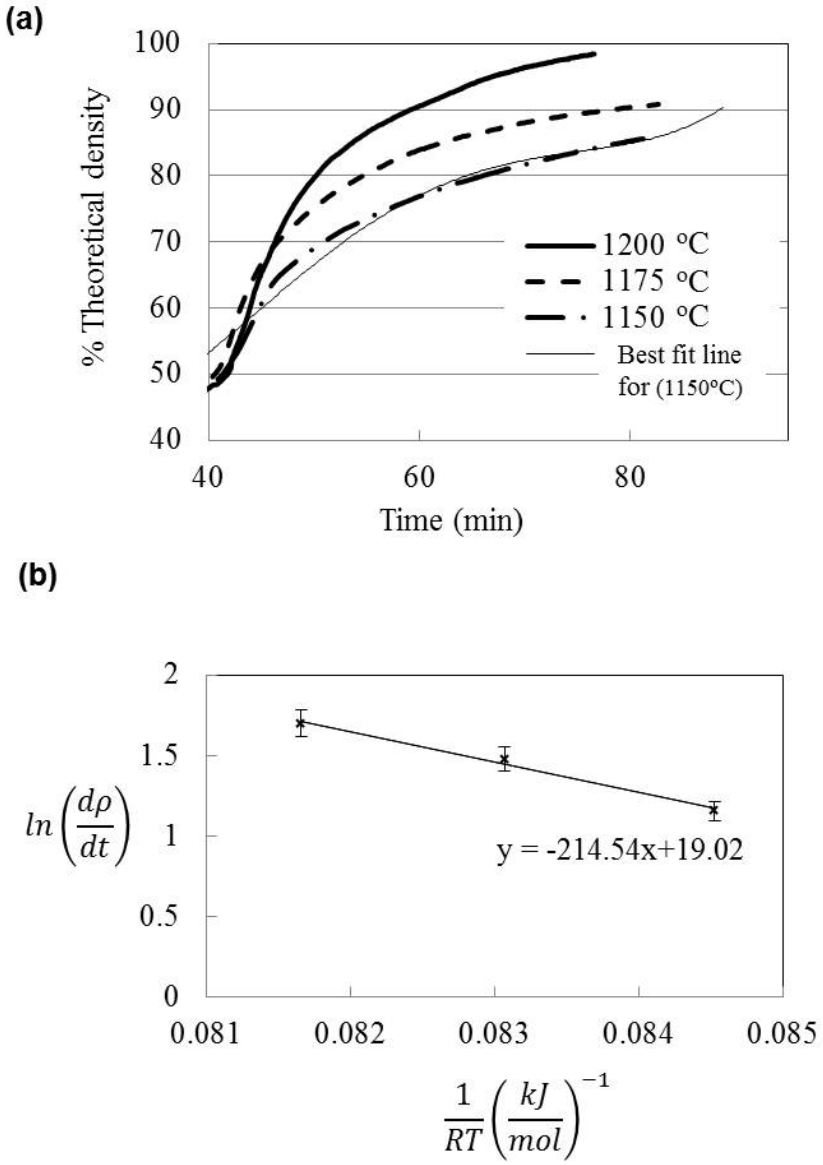

Figure 4.14: (a) Isothermal densification behavior of 8YZ at three different temperatures with microwave heating and (b) Arrhenius plot for 90 % densification determines the activation energy for isothermal sintering of 8YZ. (Bars on each data point represent standard deviation surrounding the mean value)

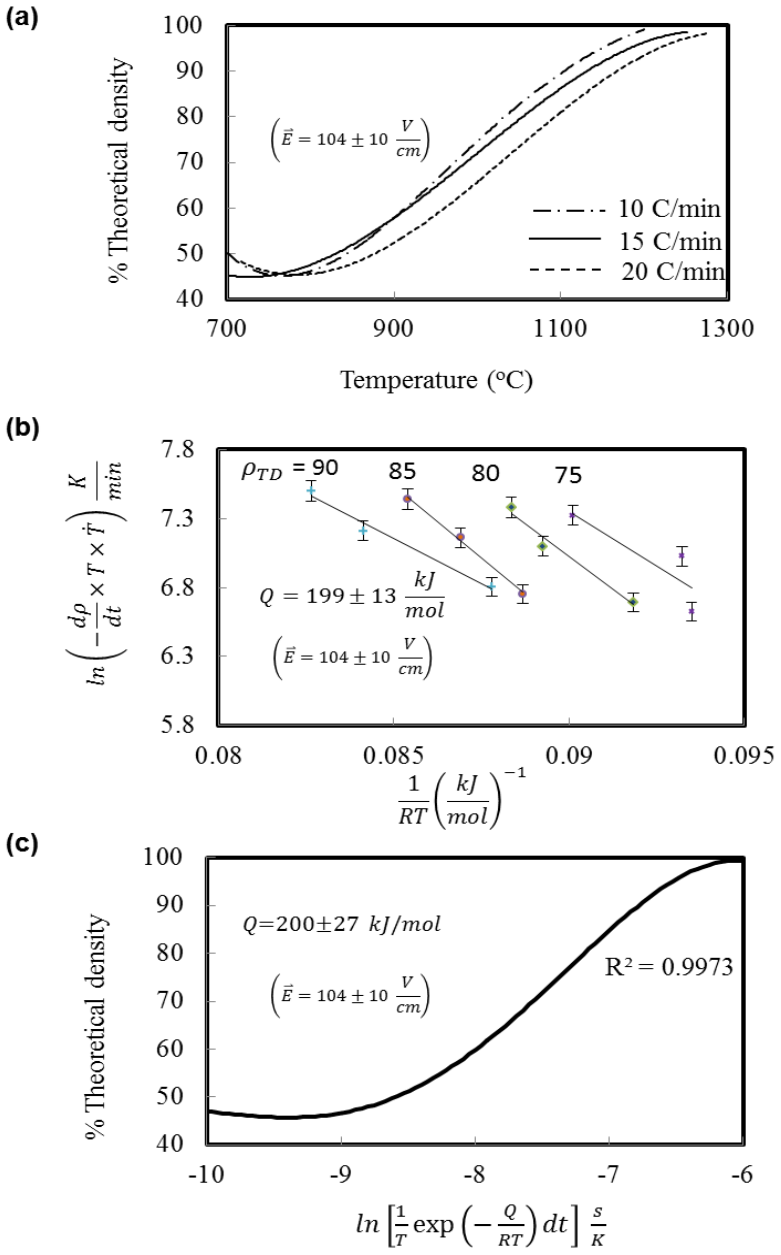

Figure 4.15: (a) Non-Isothermal sintering behavior of 8YZ with direct microwave heating, (b) Arrhenius plot for measuring activation energy using Constant Heating Rate method, (c) Master Sintering Curve approach for measuring activation energy. (Bars on each data point represent standard deviation surrounding the mean value)

ing the activation energy value with the change in electric field intensity. It can be observed that the activation energy value for sintering 8YZ decreased with the increase in the applied electric field. The activation energy measurements made for sintering 8YZ using conventional and direct microwave heating have been summarized in Table 4.2.

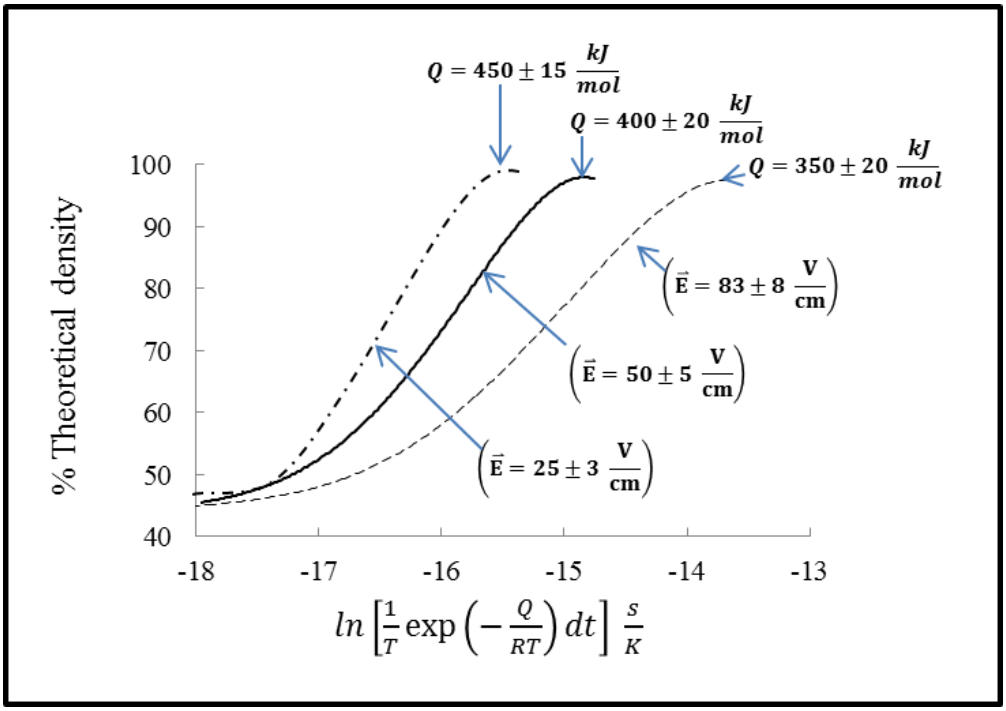

Figure 4.16: Master Sintering Curve approach for measuring the activation energy for sintering 8YZ at various values of electric field intensity.

During sintering the slowest diffusing species (cations/anions) will be limiting the rate of sintering (for details see Section 2.3.6). In 8YZ the diffusion of anions (O^{-2}) is much faster than the diffusion of cations (Zr^{+4} or Y^{+3}). Between Zr^{+4} and Y^{+3} Swaroop et al [76] observed that the Zr^{+4} is the slowest diffusing species and hence Zr^{+4} would be controlling the rate of sintering. Therefore the activation energy value recorded during sintering of 8YZ should most likely represent the diffusion of Zr^{+4} ions.

Table 4.2: Comparison of the activation energy for diffusion of Zr^{+4} ion diffusion during conventional and direct microwave sintering.

Method	**Conventional sintering,** $\frac{kJ}{mol}$	**Microwave sintering,** $\frac{kJ}{mol}$
Isothermal sintering method (Figure 4.12 and 4.14)	437±20	214±10
CHR method (Figure 4.13b and 4.15b)	520±42	199±13
MSC method (Figure 4.13c and 4.15c)	500±25	200±27
Values from literature	Volume diffusion of Zr^{+4} ion = 500 $\frac{kJ}{mol}$ [77]. Grain boundary diffusion of Zr^{+4} ion = 200 $\frac{kJ}{mol}$ [78]	Literature data unavailable

For conventional sintering, the activation energy obtained using a isothermal method (437 $\frac{kJ}{mol}$) is different from the value obtained using the non-isothermal process (CHR and MSC method, 500 $\frac{kJ}{mol}$). This difference perhaps is due to long isothermal soaking that may have resulted in a combination of both volume and grain boundary diffusion of Zr^{+4} ions. This could be a reason why Q_{Zr} determined by the isothermal method lies between the activation energy for grain boundary diffusion, 200 $\frac{kJ}{mol}$, and volume diffusion, 500 $\frac{kJ}{mol}$ of Zr^{+4} ions [74, 77, 78], while the activation energy (500 $\frac{kJ}{mol}$) estimated using the non-isothermal method is close to the volume diffusion of Zr^{+4} ions [77, 79].

For the case of direct microwave sintering (see Table 4.2) all three methods resulted in a activation energy value of $\sim$ 200 $\frac{kJ}{mol}$. It is believed that the electric field component of the microwaves may be is responsible for the reduction in activation energy [18, 61]. The results presented in Table 4.2 and Figure 4.16 have been summarized as Figure 4.17. It can be observed from Figure 4.17

that the electric field component of the microwave is decreasing the measured activation energy.

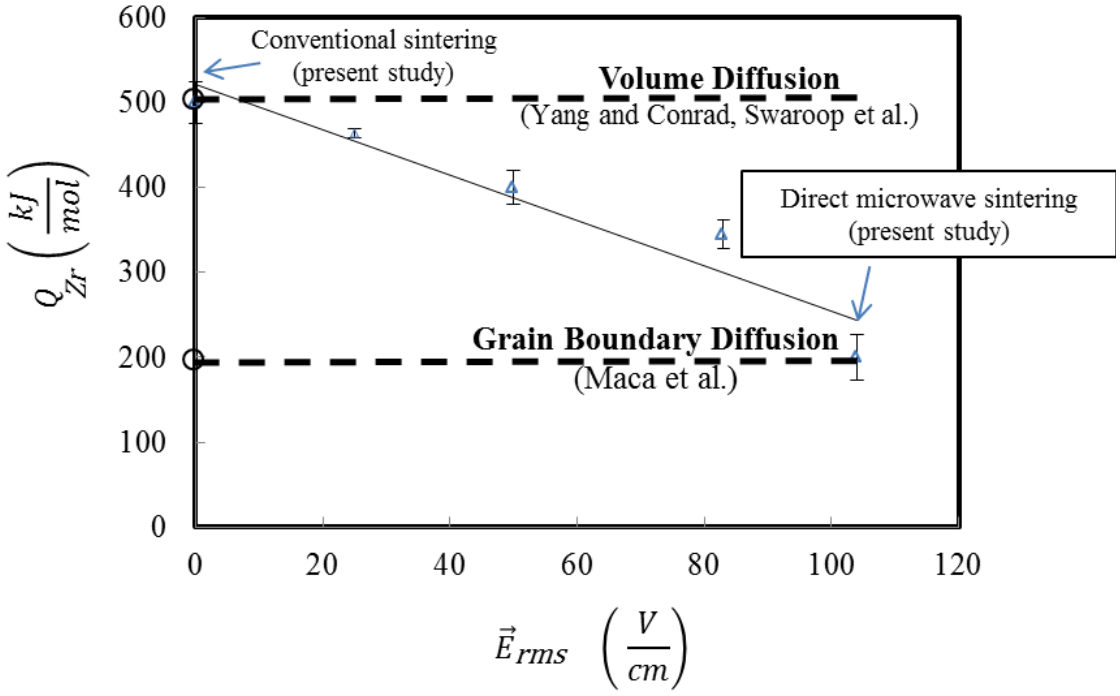

Figure 4.17: Plot of measured activation energy Q_{Zr} (volume diffusion of Zr^{+4} ion) as a function of applied electric field (oscillating at 2.45 GHz). Bars on each data point represent standard deviation surrounding the mean value.

It is possible that the microwave energy is adding an energy term, $E_{m/w}$, to the thermal energy, RT, that is part of the exponential term in the transport coefficient. The presence of an additional energy due to the electric field could result in a lower Q value.

In order to determine the magnitude of the energy, $E_{m/w}$, from the electric field the following equations were used.

$$E_{m/w} = z_i \, F \, \overrightarrow{E}_{rms} \, \frac{\lambda}{2} \tag{4.2}$$

where λ ($\sim 10^{-10}\ m$) is the inter-atomic distance. Substituting the values of z_i (= 4 $\frac{equiv}{mol}$) for the Zr^{+4} ion, F (= 96.5 $\frac{kJ}{equiv.V}$) and $\overrightarrow{E}_{rms}$ ($\sim$100 $\frac{V}{cm}$, the typical electrical field used in this study) in

the above equation will result in

$$E_{m/w} = 4\,\frac{equiv}{mol} \times 96.5\,\frac{kJ}{equiv.V} \times 100\,\frac{V}{10^{-2}\,m}\frac{10^{-10}}{2}\,m \tag{4.3}$$

$$= 1.9 \times 10^{-2}\frac{kJ}{mol} \tag{4.4}$$

As the direct microwave sintering showed complete sintering at a temperature of 1100 °C (in 20 min), the thermal energy, RT, for this temperature was 11 $\frac{kJ}{mol}$. Since the microwave energy, $E_{m/w}$ is about 10^{-2} times lower than the thermal energy ($11\frac{kJ}{mol}$), its effect on the transport coefficient should be negligible.

In summary, several different methods were used to evaluate the activation energy for both conventional and microwave processing. The activation energy values obtained for conventional sintering is consistent with the literature data, while the data for microwave case shows that the activation energies were decreased by as much as $300\frac{kJ}{mol}$. Furthermore the activation energy appears to be dependent on the electric field. It is unclear why there is a decrease in activation energy with an increase in electric field.

It appears that the transport coefficient and the driving force cannot explain the enhanced densification observed during microwave sintering. If neither the driving force nor the transport coefficient terms in the flux equation are effecting densification then what other factors could be responsible?

First, let's evaluate the possibility that the concentration of diffusion species, c, in Equation 4.1 is altered in the presence of a microwave field. This is highly unlikely considering the energy

requirements to create defects. For example, the energy required to create a Schottky defect is about, 192 $\frac{kJ}{mol}$. This is 10^5 times greater than the energy of a 2.45 GHz photon ($\sim$ 0.0097 $\frac{kJ}{mol}$) [20, 80].

Another possibility is that a mechanism other than volume diffusion is dominating the sintering behavior in the microwave field. One such mechanism could be grain boundary diffusion. The literature shows that the activation energy of volume diffusion is higher (500 $\frac{kJ}{mol}$) than grain boundary diffusion (200 $\frac{kJ}{mol}$) [77, 78]. The data collected for this study shows that as the electric field is increased the activation energy approaches that of grain boundary diffusion (see Figure 4.17).

The microwave density data, $\frac{\Delta\rho}{\rho_\circ}$, collected for this study at 1200 °C was compared to similar data obtained using a D.C field [72]. This comparison is shown in Figure 4.18. It can be observed from this figure that as the D.C field intensity is increased the densification is being accelerated. This increase is similar to the densification pattern observed for an A.C field (2.45 GHz frequency). The electric field required for a near complete densification (97 %TD) was between 80 and 100 $\frac{V}{cm}$, irrespective of the A.C or the D.C field.

Cologna et al [72] suggests that the D.C field is preferentially heating the grain boundaries, accelerating the grain boundary diffusion and resulting in the greater densification rate. Likewise, the electric field used in this study (nearly the same electric field intensities as Cologna et al [72]) could be preferentially heating the grain boundaries resulting in an activation energy that is more represented by grain boundary rather than volume transport. It should be noted that not all researchers would agree with this argument. For example, Johnson [81] considers that if the temperature of the grain boundaries is suddenly raised to a high temperature and held constant, the

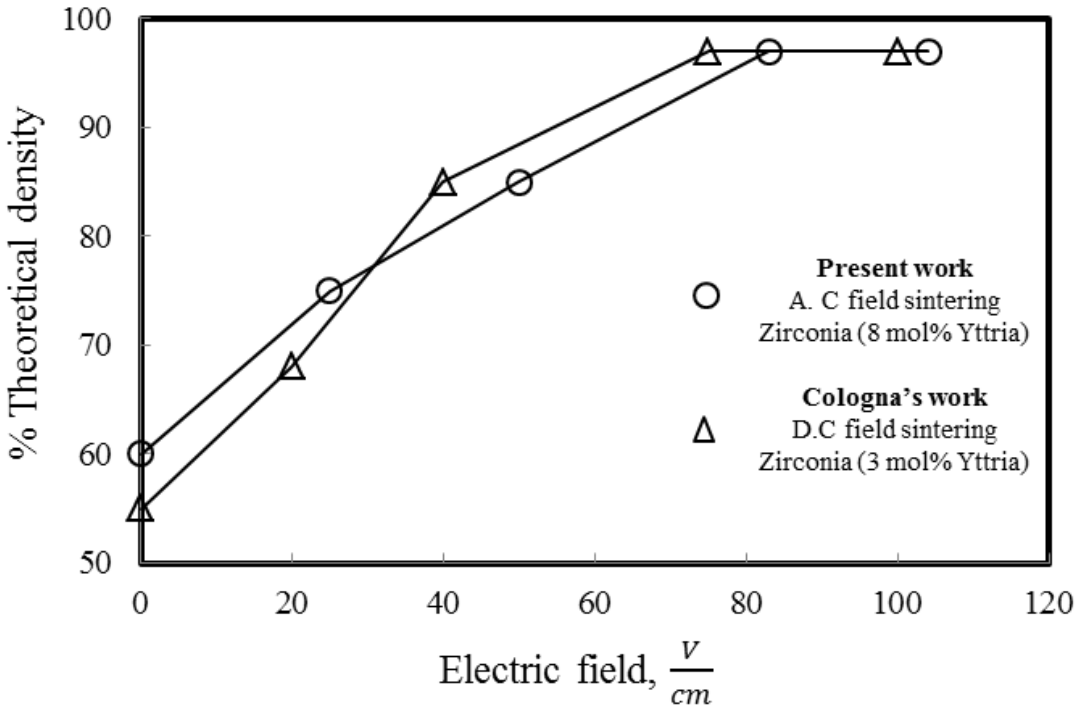

Figure 4.18: Plot of densification as a function of applied electric field for an A.C and D.C field sintering, for a processing temperature of 1200°C.

time required by the grains to reach this temperature is directly proportional to the grain boundary area and is inversely proportional to the thermal diffusivity. Johnson [81] has shown that the average time required for a 10 μm sapphire grain to reach the temperature of a grain boundary is $\sim 2\ \mu s$. According to Johnson's calculations, the material (8YZ) used for this study has a thermal diffusivity of approximately five times lower than sapphire. This would mean that the temperature differences (between a grain and grain boundary) should not be sustained more than $\sim 10\ \mu s$ [81]. Temperature differences between the grain and grain boundaries could be sustained only if the heating rate were greater than 100 $\frac{^{\circ}C}{min}$. Since all of the heating rates adopted for this study were less than 100 $\frac{^{\circ}C}{min}$, it suggests that the possibility of microwaves preferentially accelerating the grain boundary diffusion is negligible. However, Johnson's [81] calculations were based on a perfectly dense-polycrystalline material. Thus, the application of Johnson's model for sintering studies (the present work) is debatable.

A model developed by Meek [82] for sintering a system of alumina particles under a microwave field show that the heating rate of grain boundaries is approximately two times that of the grains. This difference in temperature is attributed to the relative variation in dielectric property between a grain and the grain boundary region. The material system (8YZ) used for this study was known to have a thermal conductivity of 2 $\frac{W}{m.K}$. Because of this low thermal conductivity most of the heat generated in the grain boundaries remains there.

The average temperature recorded by a thermocouple is representative of a large number of grains and grain boundaries. Assuming a grain boundary width of 10 nm, for the material used in this study the surface area of grain boundaries would represent about 30-40 % of the surface area

of the bulk (for calculations see Section A.1). Thus, the temperature reported by the thermocouple would be an average based on the relative percentages of surface area of grain boundaries and grains. So, the 1100 °C temperature reported for full densification of the material in the presence of a microwave field would be represented by the following equation.

$$T_m = \%SA_g \times T_g + \%SA_{gb} \times T_{gb} \tag{4.5}$$

where T_m is the temperature measured by the thermocouple, $\%SA_g$ is the surface area of the grain with respect to total surface area, T_g is the temperature of the grain, $\%SA_{gb}$ is the grain boundary surface area with respect to total surface area, and T_{gb} is the temperature of the grain boundary. As an example, if the grain is at a temperature of 800 °C, the temperature of grain boundary would be 1630 °C. The corresponding calculations are shown below.

$$T_m = \%SA_g \times T_g + \%\ SA_{gb} \times T_{gb} \tag{4.6}$$

$$1100^{\circ}\mathrm{C} = 0.64 \times 800^{\circ}\mathrm{C} + 0.36 \times T_{gb} \tag{4.7}$$

$$\Rightarrow T_{gb} \approx 1630^{\circ}\mathrm{C} \tag{4.8}$$

This phenomena appears as a lower temperature process in microwave sintering compared to conventional sintering. So, although it is not the inaccuracy in temperature measurement, it is possible that the temperature distribution in the sample is leading to the differences in microwave sintering.

It could be argued that even though the temperature of the grain boundaries might be higher than the grains, the volume of the grain boundary through which transport occurs is small and the

enhanced densification might not be expected. However, the volume occupied by a 10 nm grain boundary is about 50 % that of the bulk (for calculations see Section A.1). As a consequence more than half of the material is preferentially heated. This phenomena allows for substantial transport along the grain boundary region.

In summary, it may be possible that the electric field is coupling with the grain boundary regions and preferentially heating them through ionic conductivity and space charge polarization losses (in the case of A.C field). This phenomena is resulting in large temperature gradients between the grain and the grain boundaries that are "averaged out" by the thermocouple. The preferential rise in temperature along the grain boundary within a short time scale is acting as a "short-circuit" to the transport of ions. This is altering the transport mechanism from volume diffusion to grain boundary diffusion with a lower activation energy leading to accelerated flux and resulting in an enhancement in densification during microwave sintering. In this study the driving force for both conventional and microwave sintering is assumed to be the same, i.e., the surface free energy. However, the preferential heating of the grain boundaries will also result in a temperature gradient ΔT, between the grain boundary and the neck region. The ΔT is itself a driving force (see Table C.1) and can potentially result in enhanced densification. This phenomena needs to be more carefully examined by future investigators.

Chapter 5

Summary

The goals of this dissertation were to reproduce the enhanced densification (with microwave sintering) eliminating the possibility of inaccuracy in temperature measurement, and to understand which of the terms in the flux equation, if any, is leading to enhanced densification during microwave sintering.

Regarding the first goal:

- A microwave dilatometer was custom designed and built to perform sintering experiments with isothermal and non-isothermal methods. This tool was also used to validate the temperature measurements during microwave sintering. While temperature measurements were accurate, there may be a difference in temperature between grain and grain boundaries.
- It has been demonstrated that microwave sintering results in accelerated densification as compared to conventional sintering and that these differences are not due to the inaccuracy

in temperature measurement. Near full densification (97 % TD) was obtained at 1100 °C (20 min soak time) using direct microwave sintering. It required 1300 °C (20 min soak time) to reach full densification in a multimode-microwave hybrid furnace and 1400 °C (20 min soak time) in a conventional furnace.

- The microstructural features and mechanical properties such as grain size and hardness for microwave processed samples were similar to those for conventionally processed samples, but were observed at lower temperatures.

Regarding the second goal:

- It has been established that the magnitude of the electric field influenced the rate of densification. As the A.C field intensity increases so does the rate of densification. This finding is in close agreement with the Cologna's et al [72] work on D.C field sintering.

- The magnitude of the driving force for the electric field is comparable to that of the surface free energy. However, in the A.C field the net driving force should be zero. The driving force for densification is assumed to be the same for both conventional and microwave processing and is due to the energy gradient from the free surface area. The role of the additional driving force from the microwave field may be to preferentially heat the grain boundaries. It is also possible that temperature gradient exists between the grain boundaries and the neck region that could provide an addtional driving force.

- The non-isothermal sintering resulted in higher values of activation energies as compared to isothermal methods. A value of $500 \pm 25 \frac{kJ}{mol}$ was observed for non-isothermal sintering of

8YZ with conventional heating. This value was close to the volume diffusion of Zr^{+4} ion (500 $\frac{kJ}{mol}$). The direct microwave sintering resulted in activation energies values of 200 $\pm$ 27 $\frac{kJ}{mol}$. This value is close to the grain boundary diffusion of Zr^{+4} ions. It was also observed that the presence of an electric field decreases the activation energy. It is believed that the electric field is preferentially raising the temperature of grain boundaries, resulting in the enhancement of diffusion along these regions. The observed decrease in activation energy may be due to a change in transport mechanism from volume diffusion to grain boundary diffusion because of preferential grain boundary heating. It should be noted that not all investigators believe that temperature measurements can be maintained between the grain and the grain boundaries for times sufficient to enhance densification. Thus other possible reasons for the change in mechanisms have to be fully investigated.

In summary both goals have been achieved. The microwave field itself does not appear to directly effect any of the terms in the flux equation. However, the electric field does appear to be changing the mechanism of transport, which would lead to different values of terms in the flux equation. While this analysis of the data appears to be plausible, it should be understood that there may be other factors influencing microwave densification that have not been addressed. Some of them will be addressed in the Chapter 6 (Future work).

Chapter 6

Future Work

This chapter provides a list of suggestions that would further help in continuing this work or benefit research focused on explaining the phenomena of microwave enhanced sintering.

For this study, the driving force from the electrical field was considered to be exerting symmetrical forces on the diffusion of ions resulting in a net zero flux of the material. This effect has to be confirmed through a probabilistic study, as the forward and reverse fields at an atomic level may or may not be symmetrical.

This work has indicated that the grain boundaries may be experiencing preferential heating under a microwave field. The temperature differential would give rise to an additional driving force between a grain boundary and a neck region, resulting in accelerated flux. This new driving force may be contributing towards enhancement in densification during microwave sintering. This phenomena opens up the possibility for future research.

Folgar's [64] work on *structural evolution of silica aerogel under a microwave field* has shown that microwaves may be affecting the surface tension causing the enhanced densification for silica aerogel (between 900 and 1400 °C). Surface free energy, γ_{sv}, is one of the terms in Equation 1.1 that has been assumed to be constant for this study. A research initiative towards investigating the surface tension (often considered to be the material constant) under the presence of a microwave field could shed light on this potential effect.

Direct microwave sintering studies investigated for this study were performed in an oxygen rich environment (air). It would further benefit this study if these experiments would be repeated in different environments. This is important for the following reasons:

- Oxygen deficient environments have shown to decrease the processing temperatures with conventional heating [83]. Repeating these studies with microwave sintering may further lower the sintering temperatures observed in this study.
- Since most of the actinides (oxide based fuels, with $\frac{Oxygen}{Metal} < 2$) require a sintering atmospheres with different partial pressures of oxygen, setting up an inert atmosphere (Argon) in the microwave cavity would enable expansion of the microwave sintering studies for ceramic nuclear fuels with Nitrides as their base composition.

Potential improvement on the engineering aspect of the microwave hybrid dilatometer design include:

- Hardware automation for tuning the field distribution in the microwave cavity during a real

time experiment and

- The dilatometer software designed for this study can only collect and record the data. Further improvements in analyzing the data has potential for minimizing human error.

The microwave hybrid dilatometer developed for this study can aid in experiments that were previously limited either with measuring the in-situ electric field intensities or linear displacements. Also, the Master Sintering Curves (for a material system) can be generated as a function of particle size. This would provide a comprehensive database for the fuel fabrication industry in designing a sintering cycle.

Appendix A

Theoretical analysis of densification using a two-particle model

The driving force for sintering is the reduction in surface free energy for a system of particles (for details see Section 2.3.4). The flux equation that defines a sintering phenomena is quantified by the following equation:

$$J = -\frac{Dc}{RT}\,\frac{\gamma_{sv}}{n}\,\frac{dA}{dx} \tag{2.2}$$

A two-sphere model (see Figure A.1) was used to quantify the densification mechanism observed during sintering. The radius of the particle shown in Figure A.1 was marked as a, the neck between the two particles was labeled as x and the cross-sectional surface (of the neck) was represented by r. The main geometrical parameters such as the area of the neck A, volume of the neck V, and the linear shrinkage $\frac{\Delta L}{L_\circ}$ were shown in the Figure A.1.

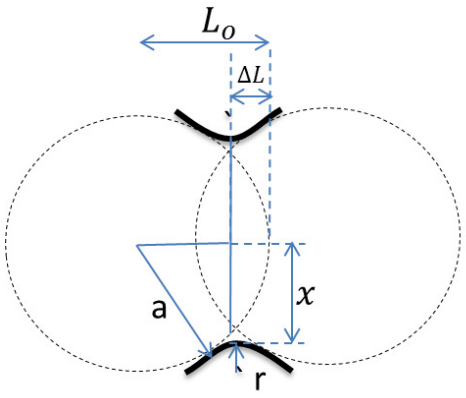

Geometrical Parameters		
Neck curvature	$r \approx \frac{x^2}{4a}$	(a-r), (a+r), x — Obtained using Pythagoras theorem
Area of the Neck	$A \approx \frac{\pi^2 x^3}{4a}$	πx, πr, $A \approx (\pi x)(\pi r)$
Volume of the Neck	$V \approx \frac{\pi^2 x^4}{16a}$	$V \approx \int A\,dx$
Linear Shrinkage	$\frac{\Delta L}{L_o} \approx \frac{x^2}{4a^2}$	$\frac{\Delta L}{L_o} \approx \frac{r}{a} \approx \frac{x^2}{4a^2}$

Figure A.1: Two sphere model representing a densification mechanism. The geometrical parameters are presented in the Table.

The rate of matter transport to the neck region $\frac{dV}{dt}$, is equivalent to the flux of molecule being transfered from the interior of the particle. This is represented as Equation A.1.

$$\frac{dV}{dt} = J\,A_d\,V_m \tag{A.1}$$

where A_d is the cross-sectional area over which diffusion occurs and V_m is the molar volume of the material being transferred. The diffusion of molecules is assumed to occur along the cross-section of the neck region x so that $A_d = 4\pi x^2$. Substituting the value of J and A_d in Equation A.1 will result in

$$\frac{dV}{dt} = -\frac{Dc}{RT}\,\frac{\gamma_{sv}}{n}\,\frac{dA}{dx}\,4\pi x^2\,V_m \tag{A.2}$$

Replacing the terms, $\frac{\gamma_{sv}}{n}\frac{dA}{dx}$ in the above equation by the surface free energy gradient $\frac{d\mu}{dx}\big|_{\gamma}$, will

result in

$$\frac{dV}{dt} = -\frac{Dc}{RT}\left.\frac{d\mu}{dx}\right|_{\gamma} 4\pi x^2\, V_m \tag{A.3}$$

In the above equation, replacing the volume of neck V by $\frac{\pi^2 x^4}{16a}$ (for details see Figure A.1) and rearranging will result in

$$\frac{d}{dt}\left(\frac{\pi^2 x^4}{16a}\right) = -\frac{Dc}{RT}\left.\frac{d\mu}{dx}\right|_{\gamma} 4\pi x^2\, V_m \tag{A.4}$$

$$\frac{x}{4a}\,dx = -\frac{4\pi DcV_m}{RT}\left.\frac{d\mu}{dx}\right|_{\gamma} dt \tag{A.5}$$

Applying the boundary conditions and integrating the above equation will result in

$$\int_0^x x dx = -\frac{16\pi DcV_m a}{RT}\left.\frac{d\mu}{dx}\right|_{\gamma} \int_0^t dt \tag{A.6}$$

$$x^2 = -\frac{32\pi DcV_m a}{RT}\left.\frac{d\mu}{dx}\right|_{\gamma} t \tag{A.7}$$

The above equation can be re-written as

$$x = -\left(\frac{32\pi DcV_m a}{RT}\left.\frac{d\mu}{dx}\right|_{\gamma}\right)^{\frac{1}{2}} t^{\frac{1}{2}} \tag{A.8}$$

$$x \times \frac{x}{4a^2} = -\left(\frac{32\pi DcV_m a}{RT}\left.\frac{d\mu}{dx}\right|_{\gamma}\right)^{\frac{1}{2}} t^{\frac{1}{2}} \times \frac{x}{4a^2} \tag{A.9}$$

$$\frac{x^2}{4a^2} = -\left(\frac{2\pi DcV_m x^2 t}{RTa^3}\left.\frac{d\mu}{dx}\right|_{\gamma}\right)^{\frac{1}{2}} \tag{A.10}$$

The change in linear dimension due to densification is given by (see Figure A.1)

$$\frac{\Delta L}{L_\circ} = \frac{x^2}{4a^2} \tag{A.11}$$

Substituting Equation A.10 in the above equation will result in

$$\frac{\Delta L}{L_\circ} = -\left(\frac{2\pi D c V_m x^2 t}{RTa^3}\frac{d\mu}{dx}\bigg|_\gamma\right)^{\frac{1}{2}} \tag{3.1}$$

Assuming the material being sintered exhibits isotropic shrinkage, the densification can be represented as follows

$$\frac{\Delta\rho}{\rho} \approx \left(\frac{\Delta L}{L_\circ}\right)^3 = -\left(\frac{2\pi D c V_m x^2 t}{RTa^3}\frac{d\mu}{dx}\bigg|_\gamma\right)^{\frac{3}{2}} \tag{A.12}$$

$$\because D = D_\circ \exp\left(-\frac{Q}{RT}\right) \tag{2.29}$$

$$\frac{\Delta\rho}{\rho} \approx -\left(D_\circ \exp\left(-\frac{Q}{RT}\right)\frac{d\mu}{dx}\bigg|_\gamma \frac{2\pi c V_m x^2 t}{RTa^3}\right)^{\frac{3}{2}} \tag{A.13}$$

To study the role of transport coefficient and driving force on densification, the above equation is rearranged as follows

$$\frac{\Delta\rho}{\rho} \approx -\left(\underbrace{\overbrace{D_\circ \exp\left(-\frac{Q}{RT}\right)}^{\text{Transport Coefficient}}\ \overbrace{\frac{d\mu}{dx}\bigg|_\gamma}^{\text{Driving Force}}\ \frac{c}{RT}}_{\text{Flux}}\frac{2\pi V_m x^2 t}{a^3}\right)^{\frac{3}{2}} \tag{A.14}$$

$$\because \frac{d\mu}{dx}\bigg|_\gamma = \frac{\gamma_{sv}}{n}\frac{dA}{dx} \qquad \text{(see Section 2.3.4)}$$

Equation A.14 can be rewritten as

$$\frac{\Delta\rho}{\rho} \approx -\left(\underbrace{\overbrace{D_\circ \exp\left(-\frac{Q}{RT}\right)}^{\text{Transport Coefficient}} \overbrace{\frac{\gamma_{sv}}{n}\frac{dA}{dx}}^{\text{Driving Force}} \frac{c}{RT}}_{\text{Flux}} \frac{2\pi V_m x^2 t}{a^3} \right)^{\frac{3}{2}} \tag{A.15}$$

or

$$\frac{\Delta\rho}{\rho} \approx \left(\frac{\Delta L}{L_\circ}\right)^3 = -\left(\underbrace{\overbrace{D_\circ \exp\left(-\frac{Q}{RT}\right)}^{\text{Transport Coefficient}} \overbrace{\frac{\gamma_{sv}}{n}\frac{dA}{dx}}^{\text{Driving Force}} \frac{c}{RT}}_{\text{Flux}} \overbrace{\frac{2\pi V_m x^2}{a^3}}^{\text{Material Constants}} \right)^{\frac{3}{2}} t^{\frac{3}{2}} \tag{1.1}$$

A.1 Volume and surface area of grain boundary with respect to a grain

Assuming a single grain (of 100 μm length) takes a shape of the cube and the length of the grain boundary is about 10 nm. A two dimensional view of this picture is shown below.

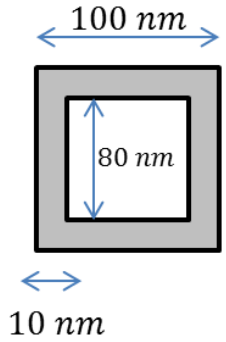

The volume of the grain is V_g = $(100\mu m)^3$.

The volume of the grain boundary is V_{gb} = $(100\mu m)^3 - (80\mu m)^3$.

The percentage of volume occupied by grain boundary to the grain is $\frac{V_{gb}}{V_g} = \frac{(100\mu m)^3 - (80\mu m)^3}{(100\mu m)^3} \approx 50\%$.

Using a similar analogy, the percentage of surface area occupied by the grain boundary with respect to the grain is given by $\frac{S_{gb}}{S_g} = \frac{6\times100^2 - 6\times80^2}{6\times100^2} \approx 36\%$

Appendix B

Measuring linear changes in materials using microwave heating with a push-rod dilatometer

Dilatometer is a tool used for studying the dimensional changes in materials as a function of temperature. A singlemode microwave cavity was altered for incorporating heating elements and a dial gauge. The heating coils were used to determine the variation in the expansion measurements with the experimental arrangement. The validity of the measurement and the calibration procedure was verified by measuring the expansion of the following materials: Sapphire, Alumina, Copper, and Fused Quartz. The experimental setup was able to determine the coefficient of thermal expansion to an accuracy of $\pm$ 3%. Microwave hybrid heating was then used (with the aid of SiC

susceptor, see Section 3.3.6) to study the variation in sintering behavior of 8YZ with the applied electric field.

B.1 Introduction

Thermal expansion in materials is commonly measured using a dilatometer. Apart from measuring the thermal expansion, dilatometers are used for monitoring the shrinkage during sintering of powdered materials (in-situ). This is useful for studying the sintering phenomena. Commercially available dilatometers utilize conventional/radiant type of heating technique. This study requires the construction of a microwave dilatometer that is not available commercially. The following sections provides a detailed description of the instrumentation (hardware and software) and the calibration procedure developed for this study.

B.2 Instrumentation

B.2.1 Hardware design

The singlemode microwave furnace was selected for adding the conventional heating elements and the dial gauge. TE_{103} applicator was chosen due to the ease of estimating the microwave field patterns in the cavity. Low intensity microwave regions were selected for proper placement of heating elements. Figure B.1 shows the overview of the singlemode microwave furnace. It can

be observed that via. a twistable waveguide the applicator was rotated by a 90° angle. This was necessary as the heating elements had to be suspended down through the narrow face of the cavity. The inset in Figure B.1 shows the slots that were machined for inserting heating elements and the pushrod into the TE_{103} singlemode microwave cavity.

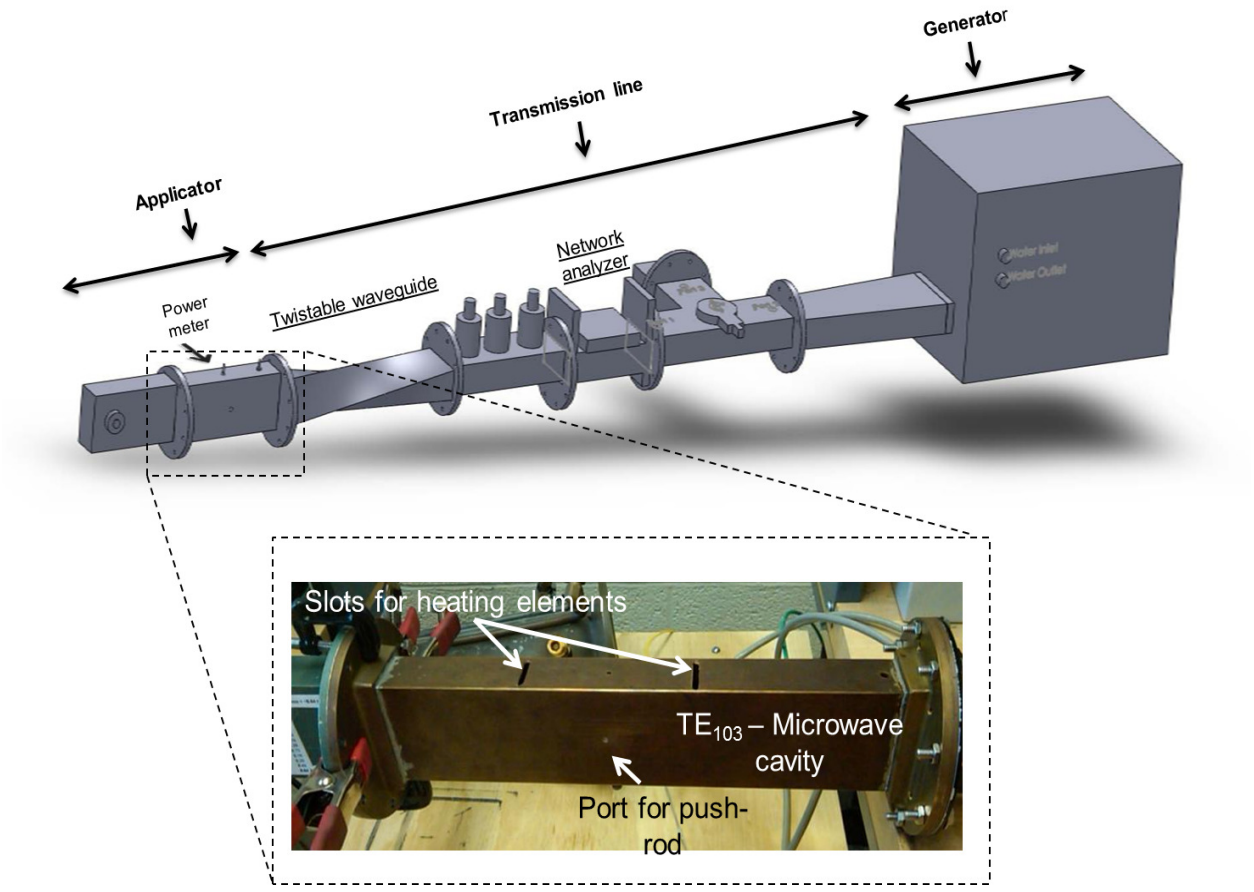

Figure B.1: Singlemode microwave furnace: inset shows the slots machined for inserting the heating elements and push-rod.

The heating elements selected for this study were custom designed for the cavity. The molybdenum disilicide elements[1] were "U" shaped. These elements need to be suspended with the bottom "U" facing the narrow section of the applicator. The elements were rated to operate at a maximum

[1]MD-33 Lu=40 Le=51 a=15, ISquaredR Inc.,

temperature of 1600 °C in an oxidizing atmosphere. They are typically operated at low voltages (0 to 2.8 $\frac{volts}{element}$) and high currents (0 to 53 $\frac{amps}{element}$) with a maximum power rating of 150 $\frac{watts}{element}$.

The dimensional specifications of molybdenum disilicide elements are shown in Figure B.2a. Two step down transformers[2] (110 V to 10 V) were connected in parallel for controlling the voltage independently for each of the heating elements. Figure B.2b shows the circuit diagram that was designed for controlling these heating elements. A potentiometer (is a three terminal resistor) was installed between the transformer and the direct power supply. This setup allowed voltage increments to the heating elements with a sensitivity of 0.1 V. Figure B.2c shows the positioning of the push-rod and the heating elements attached to the microwave cavity.

The side and top view of the finished microwave hybrid dilatometer is shown in Figure B.3. It can be seen that a "C" type clamp was used for attaching the steel railing to the cavity (see Figure B.3a). A dial gauge[3] is attached to a platform that is mounted onto the steel railing. The dial gauge had a resolution of 1 μm. The expansion/contraction of the specimen is transfered out of the furnace via. a push-rod (see Figure B.3a).

Figure B.3b shows the finished view of the dilatometer with heating elements placed in the microwave cavity. It can be observed that the heating elements are placed along the low intensity electric field regions that are separated by a distance of $\frac{\lambda_g}{2}$[4], this ensured a minimal interaction between the applied microwaves and the molybdenum disilicide elements. The positioning of the thermocouple is also shown in Figure B.3b.

[2]Rectifier Transformer 10 V, Signal Transformer Inc.,
[3]Digi Mark IV, Slyvac Inc.,
[4]λ_g is the wavelength of the wave-guide

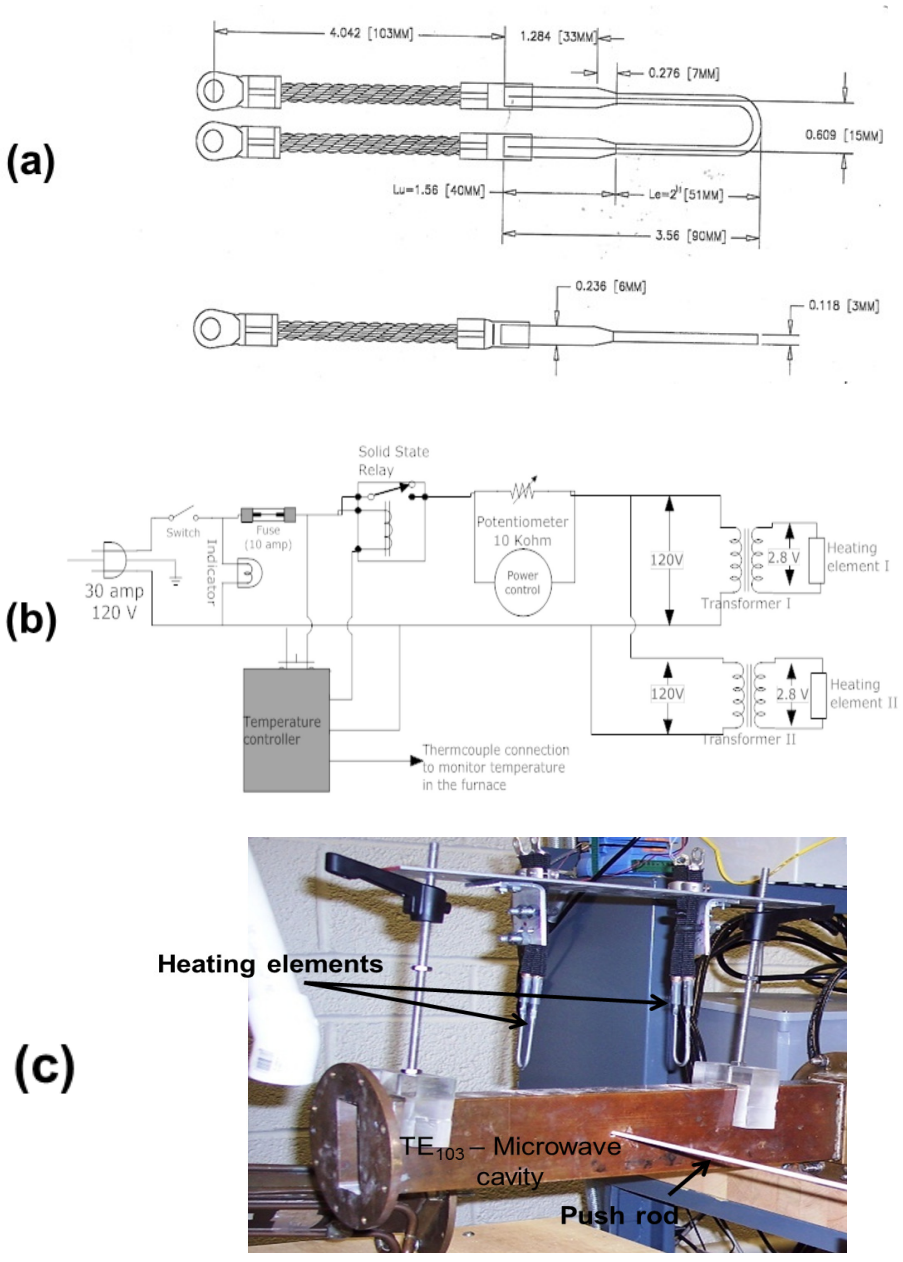

Figure B.2: (a) Dimensions of the custom ordered molybdenum dislicide heating elements, (b) Circuit designed for controlling the heating elements and (c) Singlemode microwave cavity with heating elements and the push-rod.

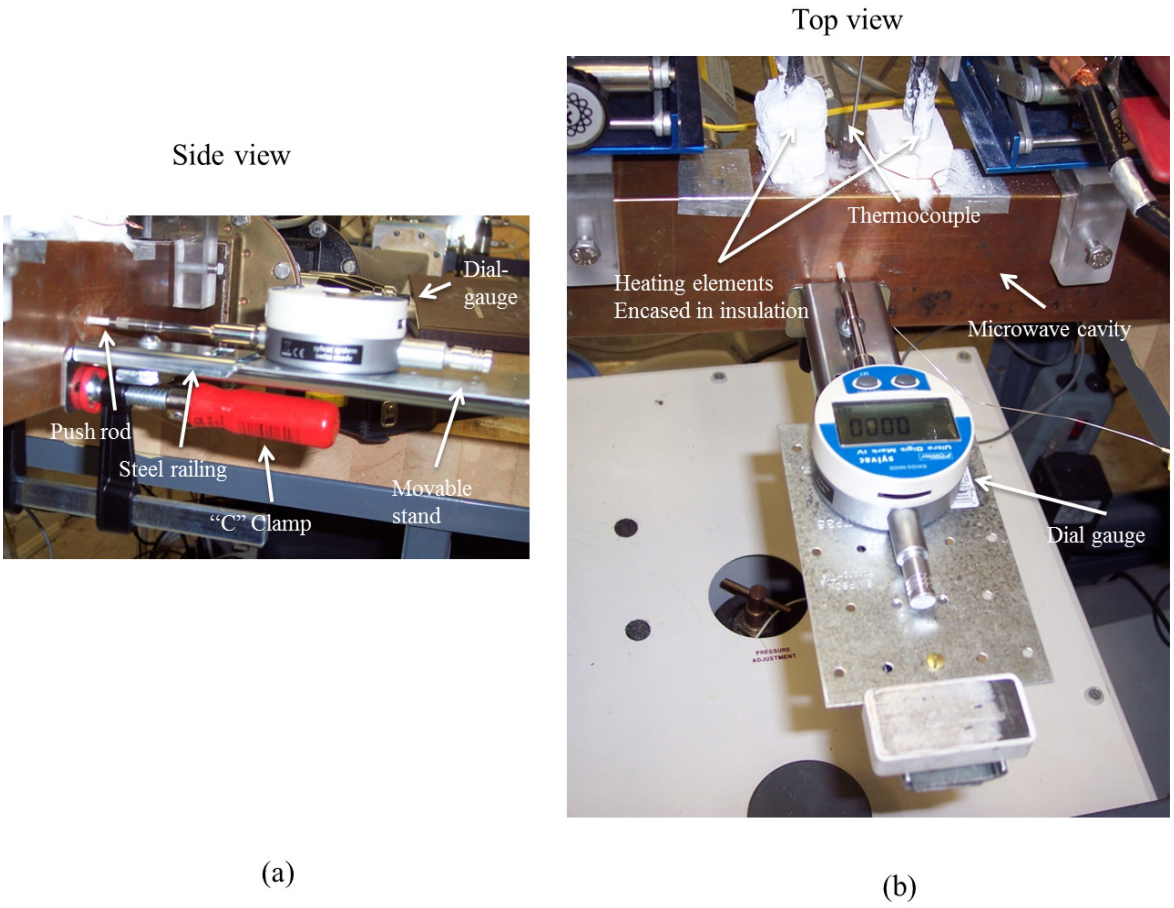

Figure B.3: (a) Side view and (b) top view of a push rod microwave hybrid dilatometer.

B.2.2 Electric field measurements

A power meter[5] consisting of a sensing unit[6] and an attenuator (20 dB) is used for measuring the microwave power along the vicinity of the sample. Based on a method developed by Folgar [64], the power scale, represented in $Milliwatts$, is converted to its equivalent units of electric field ($\frac{V}{cm}$) using the following equation:

$$\overrightarrow{E} = \sqrt{\frac{2 \times Z_{TE} \times P}{a \times b}} \qquad \text{here} \quad Z_{TE} = \frac{\eta}{\sqrt{\left(1 - \left(\frac{f_c}{f_o}\right)^2\right)}} \tag{B.1}$$

where, P is the power of the microwave, η is the impedance of the medium (air, 377 Ω), Z_{TE} is the impedance of the TE_{10} waveguide, a (=7.2 cm) and b (=3.4 cm) are the dimensions of the cavity, f_c is the cut-off frequency of the wave guide (2.80 GHz), $f_\circ$ is the frequency of the incident microwave (2.425 GHz). The conversion scale is generated by creating ideal conditions i.e., water load is used on one end (of the applicator) to avoid the resonance patterns arising from the reflection of the microwaves.

Figure B.4 plots the electric field intensities calculated (using Equation B.1) at different power levels as recorded by the network analyzer. These values are then correlated with the power readings indicated by the power meter (shown as the secondary X axis in Figure B.4). It can be observed that the values recorded by the power meter are different to that of the network analyzer; this is due to the presence of microwave attenuators. The attenuators prevent the power meter from

[5] 435B, Hewlett-Packard
[6] 8418, Hewlett-Packard

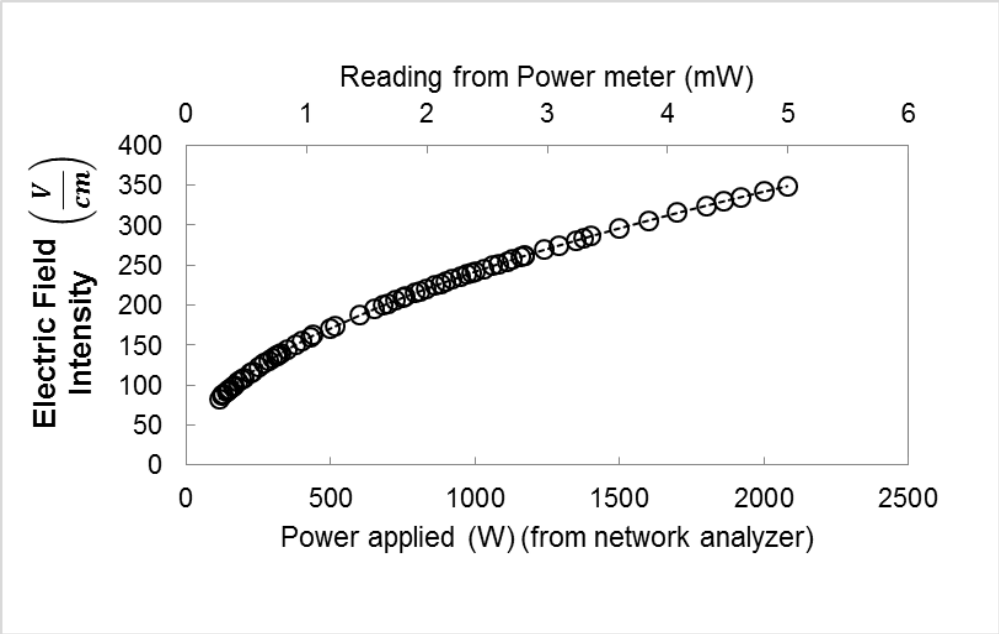

Figure B.4: Electric field intensity of the microwave field scaled with respect to the power-meter readings.

seeing the higher powered microwaves that are prone to cause damage to the internal sensing unit.

While performing the sintering experiments the reading from the power meter (as opposed to the network analyzer) is used to estimate the electric field intensity using Figure B.4. This is required as the standing wave patterns (due to resonance phenomena) result in higher magnitude of power recorded inside the cavity, which is different to that of the power measured by the network analyzer. The location of power meter and the network analyzer can be seen in Figure B.1. This procedure resulted in high frequency electric field measurements that are essential for studying their influence on activation energy.

B.2.3 Software design

The output from the dial gauge was recorded using LABVIEW[7], a software program commonly used for data collection. It is a visual programming language that has the ability to communicate with multiple devices at the same time and display the data on the computer. Figure B.5 shows the front panel design and Figure B.6 shows the block diagram of the code.

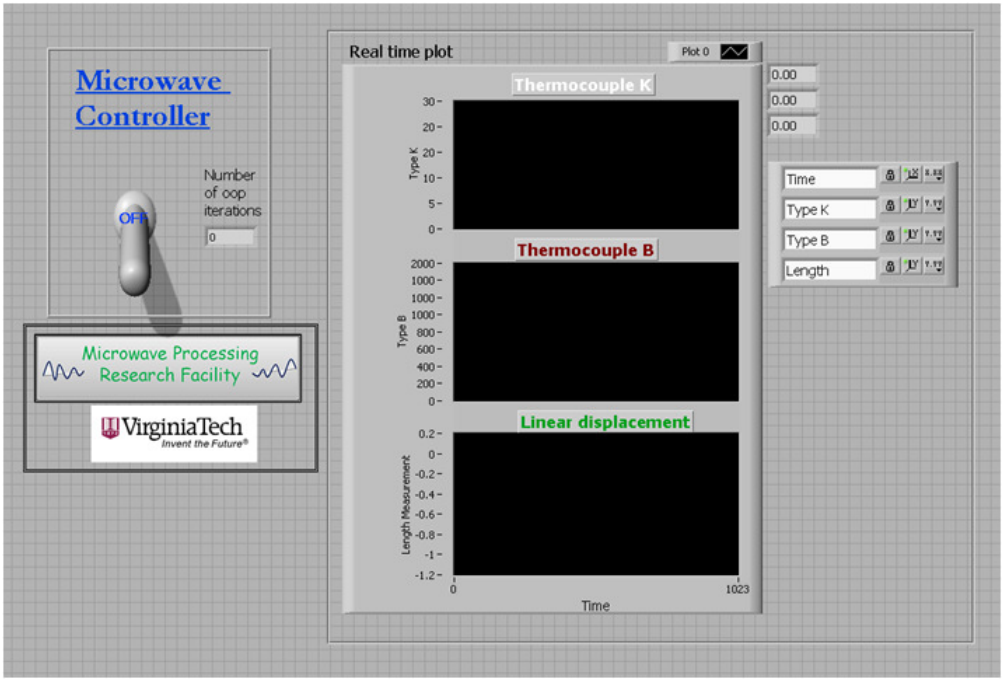

Figure B.5: Front panel of the microwave controller software developed using a LABVIEW program.

The front panel display controls the microwave source, collects data from temperature monitors and dial gauge. The block diagram aids in proper function of the front panel and assists the program in storing the data to the user specific file.

[7]National Instruments

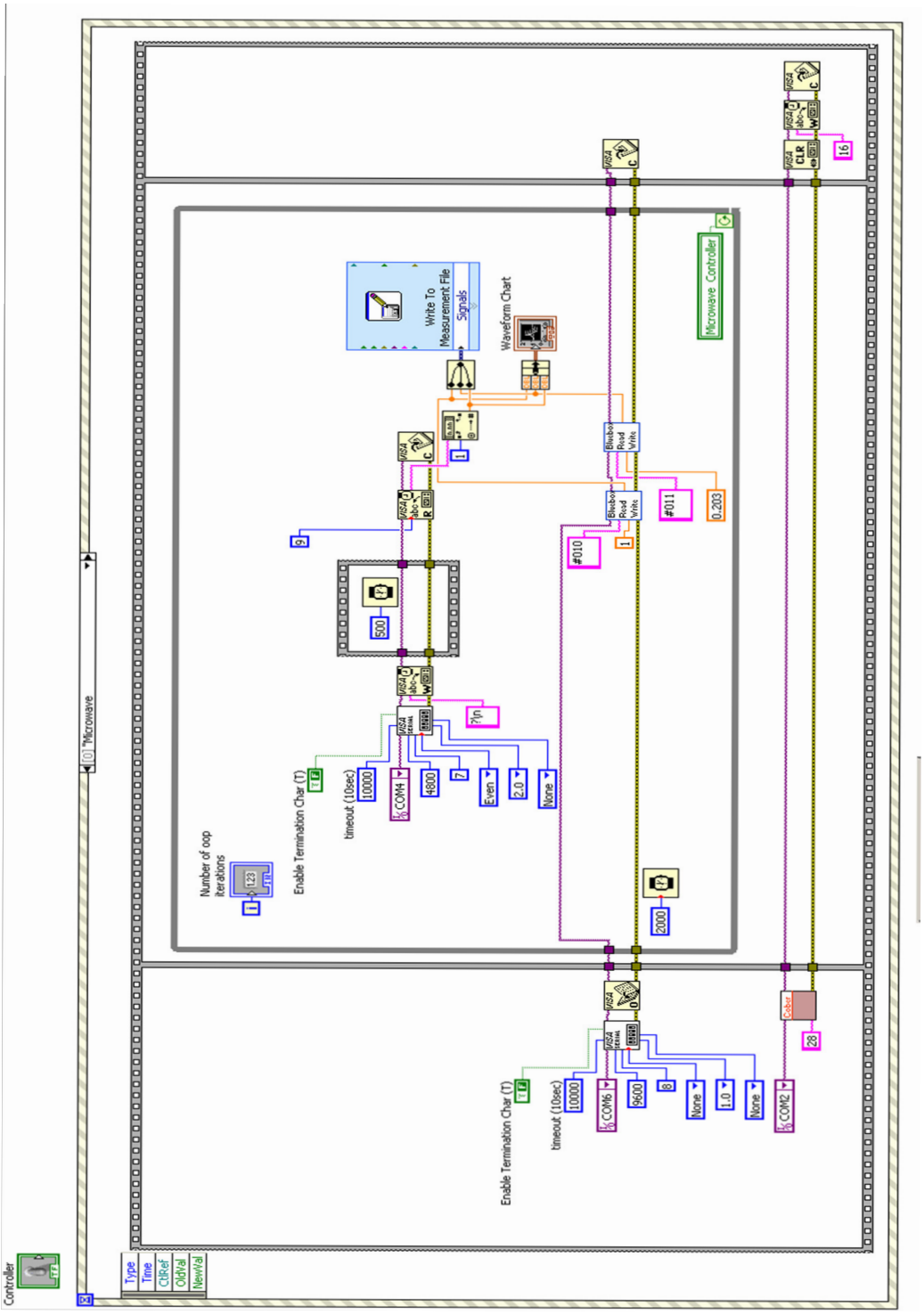

Figure B.6: Block diagram of the LABVIEW code designed for collecting data from the temperature measuring unit and dial gauge.

B.3 Calibration procedure

The calibration procedure adopted for this study was in accordance with ASTM standard E228 [84]. A slow heating rate of 5 $\frac{^{\circ}C}{min}$ was adopted for this experiment. Slow heating rates essentially minimized the thermal gradients within the material, allowing volumetric expansion of the sample. During an experiment, the furnace heated the sample along with the measuring system. This operation was quantified as

$$\frac{\Delta L}{L_o}^{Measured}_{Expansion} = \frac{\Delta L}{L_o}^{True}_{Expansion} + \frac{\Delta L}{L_o}^{Measuring-system}_{Expansion} \tag{B.2}$$

From the above equation, it can be observed that the true expansion of the sample can be obtained by subtracting the expansion of the measuring system (primarily includes push-rod and the sample holder) from the measured expansion of the sample.

The expansion of the measuring-system was determined by measuring the expansion of a reference standard that was identical in length to that of the sample. For this study, high purity (99.99%) Alumina-THETA 410 was used as a standard reference material. The expansion of the measuring system was further used to validate the thermal expansion measurements on Sapphire, Alumina, Copper, and Fused Quartz. All of these experiments were performed using conventional heating.

Figure B.7a shows the expansion ($\frac{\Delta L}{L_\circ}$) vs. temperature plot for a standard Alumina-THETA 410. The slope of the line represents the Coefficent of Thermal Expansion (COE) of the material. The central tendency of a data set pertaining to four repetitions was used to represent the data.

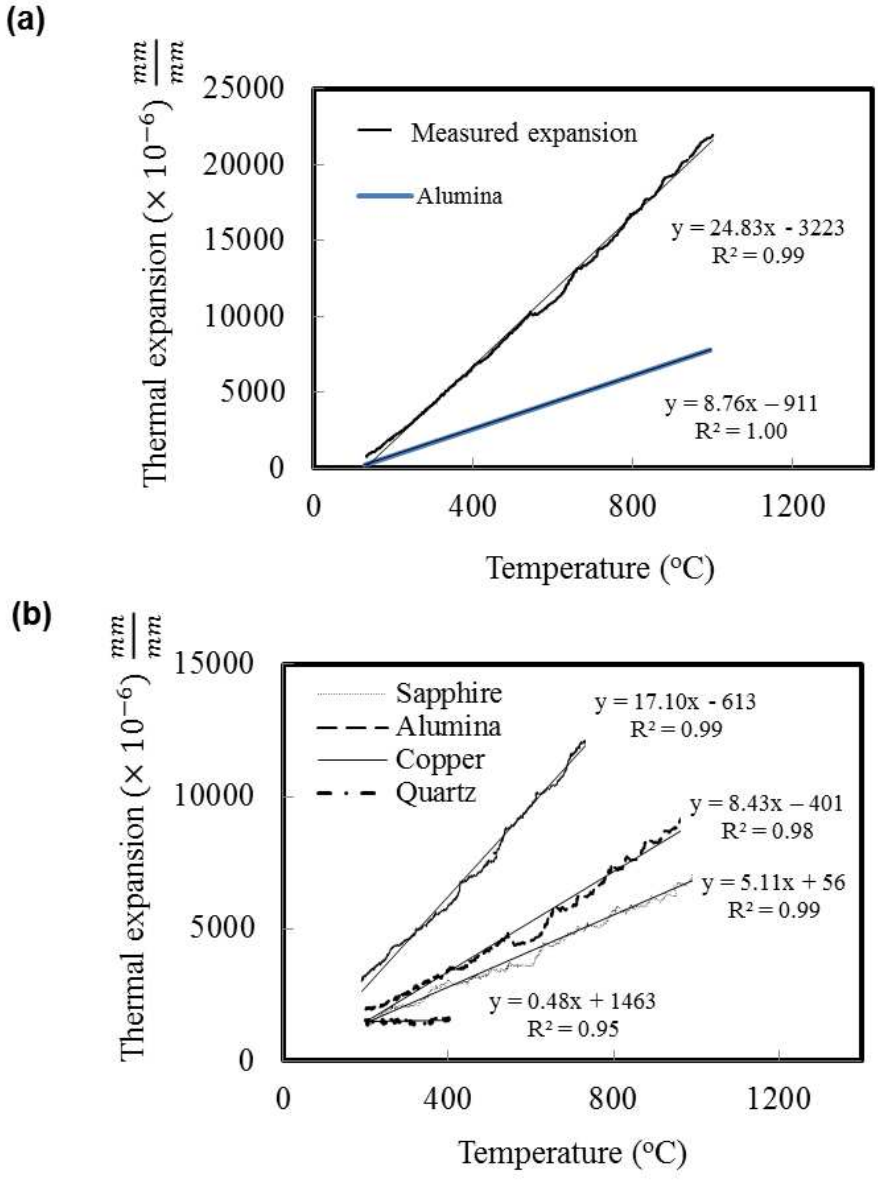

Figure B.7: (a) Thermal expansion of Theta T 410 alumina and push rod with respect to the actual expansion of alumina and (b) Expansion of Sapphire, Alumina, Copper and Quartz with temperature using conventional heating.

The measured expansion of the alumina standard, shown in Figure B.7a, deviated from the theoretical values (THETA 410). This change was due to a factor of error associated with simultaneous expansion of the push-rod and the sample holder. The deviation in the COEs of the measured expansion was recorded. These values were then substituted into Equation B.2 to obtain the true expansion of the sample.

The COE of the following materials were measured (using conventional heating) to validate the calibration procedure, Saphhire [8], Alumina [9], Copper [10], and Fused quartz [11]. These results are shown in Figure B.7b. It can be observed that the COE of Copper (17.10 $\frac{mm/mm}{^{\circ}C}$) was the highest, while Fused Quartz (0.48 $\frac{mm/mm}{^{\circ}C}$) had the lowest COE; these values were in close agreement with the COE values reported by the vendor, suggesting that the calibration procedure was reliable. The deviation in the measured values (from theoretical expansion) were observed to be within a range of $\pm$ 3 %.

B.4 Microwave dilatometer

Figure B.8 compares the thermal expansion behavior of Alumina and sintering behavior of 8YZ with respect to the heating source (conventional and microwave heating).

It can be observed from Figure B.8a that the COE of Alumina remained the same even when the heating source was changed from conventional to microwave (the electric field intensity being 107

[8] 42132-8, Kyocera
[9] THETA 410, Theta, Inc.
[10] Alloy 151, McMaster
[11] No. 3, Technical glass products

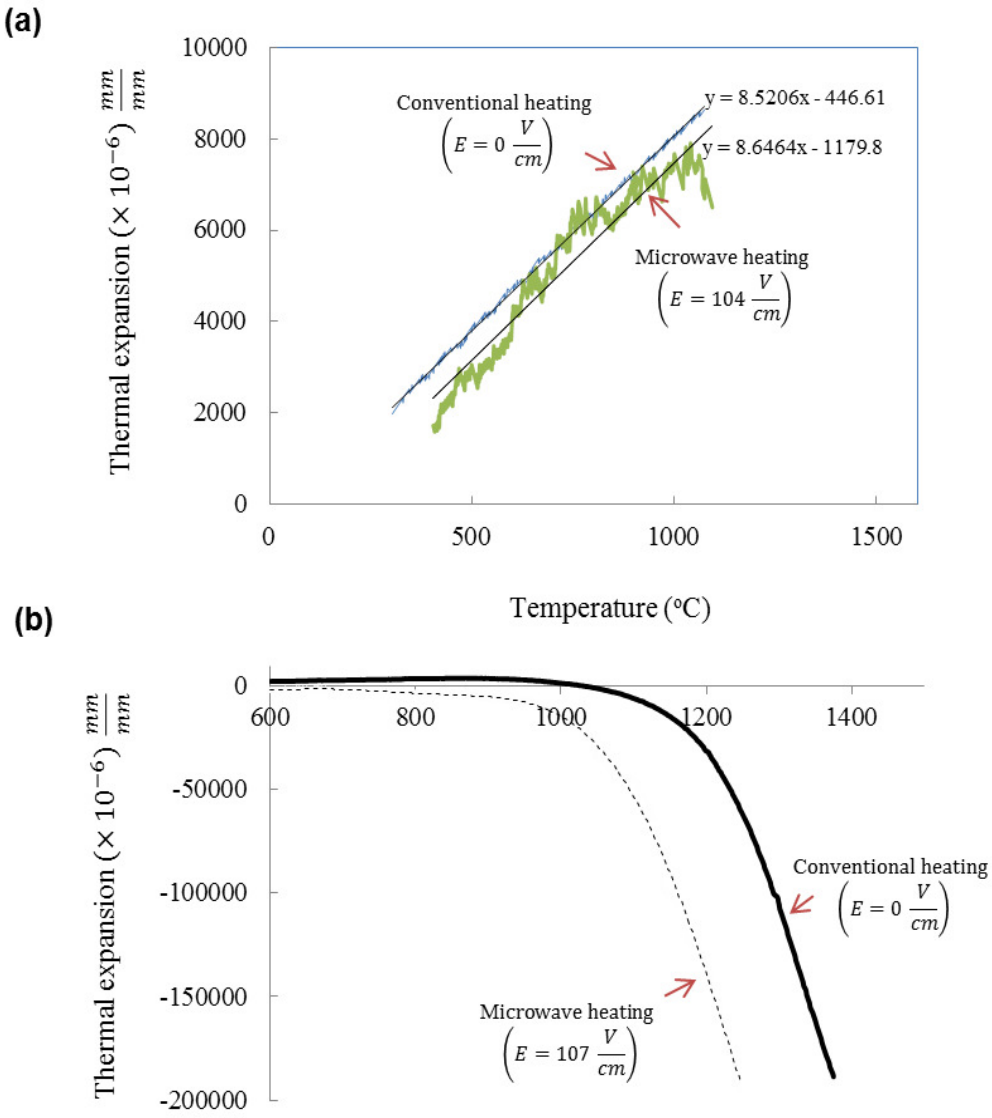

Figure B.8: (a) Thermal expansion of Alumina and (b) Sintering behavior of 8YZ with conventional heating, and microwave heating (electrical field being 107 $\frac{V}{cm}$).

$\frac{V}{cm}$). Whereas, the sintering behavior of 8YZ shifted towards lower temperature due to microwave heating (see Figure B.8b). This behavior suggests that microwaves are accelerating the sintering process at lower temperatures. This result is in accordance with many of the microwave sintering reports present in the literature [4, 5, 6].

The SiC suceptor arrangement (see Figure 3.3.6) was further used with the dilatometer setup to study the sintering behavior of 8YZ as a function of applied electric field. The data generated using this instrument was used to study the variation in activation energy with the applied electric field intensity.

Appendix C

External driving forces responsible for diffusion

Ficks first law was based on the empirical observations that only consider the possibility of matter transport due to the gradients in concentration. This law is insufficient to explain the diffusion occurring due to the presence of any external force. Displacement of the diffusing species by any kind of an external force will result in flux. The matter transport would occur from regions of high energies (energy is the amount of work performed by force) to the regions of low energies. The concept of considering the matter transport due to the change in energy with distance can generalize the situation for defining diffusion [17, 85, 75, 86]. It has been identified that the material flux could result from a variety of external forces that are acting on the system. Some of these are listed below

Table C.1: External driving forces responsible for diffusion.

Driving Force	Expression			Units
Concentration	$\frac{dc}{dx}$	$\frac{R\times T}{c}\times\frac{dc}{dx}$	c : Concentration $\left(\frac{g}{cm^3}\right)$; T : Temperature (K); R : Gas constant $\left(\frac{J}{mol.K}\right)$;	$\frac{\left(\frac{J}{mol.K}\times K\times\frac{g}{cm^3}\right)}{cm\times\frac{g}{cm^3}}\Rightarrow\left(\frac{J}{mol.cm}\right)$
Pressure	$\frac{dP}{dx}$	$V_m\times\frac{dP}{dx}$	P : Pressure $\left(\frac{J}{cm^3}\right)$; V_m : Molar volume $\left(\frac{cm^3}{mol}\right)$	$\left(\frac{cm^3}{mol}\times\frac{J/cm^3}{cm}\right)\Rightarrow\left(\frac{J}{mol.cm}\right)$
Temperature	$\frac{dT}{dx}$	$\frac{Q^*}{T}\times\frac{dT}{dx}$	Q^* : Heat of transport $\left(\frac{J}{mol}\right)$; T : Temperature (K)	$\left(\frac{J}{mol.K}\times\frac{K}{cm}\right)\Rightarrow\left(\frac{J}{mol.cm}\right)$
Surface energy	γ_{sv}	$\frac{\gamma_{sv}}{n}\times\frac{dA}{dx}$	γ_{sv} : Surface energy $\left(\frac{J}{cm^2}\right)$; A : Area (cm^2)	$\frac{J}{mol.cm^2}\times\left(\frac{cm^2}{cm}\right)\Rightarrow\left(\frac{J}{mol.cm}\right)$
Electric field	$\vec{E}$	$z_i\times F\times\vec{E}$	$\vec{E}$: Electric field $\left(\frac{V}{cm}\right)$; z_i : Effective electric charge $\left(\frac{equiv}{mol}\right)$; F : Faraday constant $\left(\frac{J}{V.equiv}\right)$	$\left(\frac{equiv}{mol}\times\frac{J}{V.equiv}\times\frac{V}{cm}\right)\Rightarrow\left(\frac{J}{molcm}\right)$
Gravitational field $(G=mg)$	$\frac{dG}{dx}$	$h\times\frac{dG}{dx}$	m : mass $\left(\frac{g}{mol}\right)$; g : acceleration due to gravity $\left(\frac{cm}{s^2}\right)$; h : height (cm);	$cm\times\frac{\left(\frac{g}{mol}\times\frac{cm}{s^2}\times cm\right)}{cm}\Rightarrow\left(\frac{erg}{cm}\right)\Rightarrow 10^{-7}\left(\frac{J}{mol.cm}\right)$
Centrifugal force $(C=m\omega^2 r)$	$\frac{dC}{dx}$	$r\times\frac{dC}{dx}$	m : mass $\left(\frac{g}{mol}\right)$; ω : angular velocity $\left(\frac{rad}{s^2}\right)$; r : radius (cm);	$cm\times\frac{\left(\frac{g}{mol}\times\frac{1}{s^2}\times cm\right)}{cm}\Rightarrow\left(\frac{erg}{cm}\right)\Rightarrow 10^{-7}\left(\frac{J}{mol.cm}\right)$
				$\left(\frac{J}{mol.cm}\right)\Rightarrow\left(\frac{10^{-2}N}{mol}\right)$

The driving force, $\frac{d\mu}{dx}\big|_{\gamma}$, for sintering two 0.1 μm diameter 8YZ particulates is shown below. One mole of 8YZ powder occupies 136.19 g. The total number of moles occupied by two 0.1 μm diameter 8YZ particulates is

$$\text{Total number of moles, } n = \frac{\text{Total weight} \times 1\, mol}{136.19\, g} \tag{C.1}$$

$$\text{Total Weight} = \rho_{TD} \times V = \frac{2 \times 5.96 \times 3.14(10^{-5})^3}{6} = 6.23 \times 10^{-15}\, g \tag{C.2}$$

$$\therefore n = \frac{6.28 \times 10^{-15}\, g \times 1\, mole}{136.19\, g} \tag{C.3}$$

$$= 4.57 \times 10^{-17} moles \tag{C.4}$$

Change in the surface area of the particle from 0.1 $\rightarrow$ 0.12 μm (final particle size) is

$$dA = 2\pi 0.1^2 \times 10^{-8} cm^2 - 3.14 \times 0.1^2 \times 10^{-8} cm^2 \tag{C.5}$$

$$= 1.33 \times 10^{-10}\, cm^2 \tag{C.6}$$

The change in surface area dA will result in the change in value of the neck region dx (maximum length of the neck region) from 0 $\rightarrow$ 0.12 μm. So, dx = 0.12 μm. Substituting the values of $\gamma_{sv} = 10^{-7} \frac{kJ}{cm^2}$ [87], n, dA and dx in the following equation will result in

$$\frac{d\mu}{dx}\big|_{\gamma} = \frac{\gamma_{sv}}{n}\frac{dA}{dx} \tag{C.7}$$

$$= \frac{10^{-7} \frac{kJ}{cm^2} \times 1.33 \times 10^{-10}\, cm^2}{4.57 \times 10^{-17} mole \times 0.12 \times 10^{-4}\, cm} \tag{C.8}$$

$$= 2.4 \times 10^{4} \frac{kJ}{mol.cm} \tag{C.9}$$

The driving force from an electric field $\frac{d\mu}{dx}\big|_{\phi}$, and is represented by

$$\frac{d\mu}{dx}|_{\phi} = z_i \, F \, \overrightarrow{E}_{rms} \tag{C.10}$$

here z_i is the the charge on the ion (= 4 for Zr^{+4} ion), F is the Faraday constant ($9.65\frac{kJ}{g\,V}$) and $\overrightarrow{E}_{rms}$ is the electric field intensity ($50\frac{V}{cm}$). Substituting the corresponding values in Equation C.10 will result in

$$\frac{d\mu}{dx}|_{\phi} = 4 \times 96.5 \, \frac{kJ}{V} \times 50 \, \frac{V}{cm} \tag{C.11}$$

$$= 4 \, \frac{equiv.}{mol} \times 96.5 \times \frac{kJ}{V \, equiv.} \times 50 \, \frac{V}{cm} \tag{C.12}$$

$$= 1.9 \times 10^4 \, \frac{kJ}{mol \, .cm} \tag{C.13}$$

Appendix D

Statistical analysis

Statistical methods were used to interpret the data collected from a particular set of experiments. Three of most commonly used descriptors in this study are shown in Table D.1.

Table D.1: Statistical parameters used for data analysis

Descriptor	*Corresponding equation*
	For a sample of n measurements
	$x_1, x_2, ...x_n$
Mean, $\bar{X}$	$\bar{X} = \frac{\Sigma x_i}{n}$
Standard deviation, σ	$\sigma = \sqrt{\frac{\Sigma\left(x_i - \bar{X}\right)}{n-1}}$
95 % Confidence interval for sample mean	$CI = \pm 1.96\left(\frac{\sigma}{\sqrt{n}}\right)$

The central tendency of the data is measured using mean. The cluster (in data) around a central value is measured using standard deviation. Variability in the data is inevitable (due to the inability to conduct perfect experiments) therefore a 95 % confidence interval for mean is also provided for the data set. Confidence interval provides a range that if an experiment is repeated under the same conditions the resulting data would fall within the range for 95 % of the time. The statistical parameters shown in Table D.1 provide an inference about the general tendency of the process/experiment under consideration.

A simple linear regression straight line model is used to plot a relation between the dependent variable, typically plotted on $y-$axis, and the independent variable, as plotted on $x-$axis. For a given sintering experiment, the dataset was visualized with the aided of interpolation (a curve fitting technique).

Bibliography

[1] O. P. Gandhi, Microwave Engineering and Appliations, Pergamon Press, New York, 1981.

[2] D. M. Pozar, Microwave Engineering, John Wiley, New York, 2004.

[3] J. M. Osepchuk, IEEE Transactions on Microwave Theory and Techniques 32 (1984) 1200–1224.

[4] W. H. Sutton, Ceramic Bulletin 68 (1989) 376–386.

[5] D. E. Clark, W. H. Sutton, Annual Review of Materials Science 26 (1996) 299–331.

[6] J. Katz, Annual Review of Materials Science 22 (1992) 153–170.

[7] D. Westlen, Progress in Nuclear Energy 49 (2007) 597.

[8] R. C. Ewing, Proceedings of the National Academy of Sciences of the United States of America 96 (1999) 3432–3439.

[9] F. Hippel, Nature 394 (1998) 415–416.

[10] V. Artisyuk, M. Saito, A. Stankovsky, Progress in Nuclear Energy 47 (2005) 327–338.

[11] R. J. M. Konings, D. Haas, Applied Physics 3 (2002) 1013–1022.

[12] C. Degueldre, J. Paratte, Journal of Nuclear Materials 274 (1999) 1–6.

[13] R. M. German, Sintering Theory and Practice, John Wiley, New York, 1996.

[14] P. Balakrishna, C. K. Asnani, R. M. Kartha, K. Ramachandra, K. S. Babu, V. Ravichandran, B. N. Murty, C. Ganguly, Nuclear Technology 127 (1999) 375.

[15] T. B. Lindemer, Thermochemical analysis of gas-cooled reactor fuels containing Am and Pu oxides, Technical Report, Oak Ridge National Laboratory, 2002.

[16] Y. V. Bykov, K. I. Rybakov, V. E. Semenov, Journal of Physics D: Applied Physics 34 (2001) R55–R75.

[17] W. D. Kingery, H. K. Bowen, D. R. Uhlmann, Introduction to Ceramics, John Wiley, New York, 1976.

[18] K. H. Brosnan, G. L. Messing, D. K. Agrawal, Journal of the American Ceramic Society 86 (2003) 1307–12.

[19] A. K. D. C. F. R. R. Thridandapani, C. E. Folgar, D. E. Clark, International Journal of Applied Ceramic Technology doi: 10.1111/j.1744-7402.2010.02570.x (2010).

[20] M. A. Janney, C. L. Calhoun, H. D. Kimrey, Journal of the American Ceramic Society 75 (1992) 341–346.

[21] S. A. Freeman, J. H. Booske, R. F. Cooper, Physics Review Letters 74 (1995) 2042–45.

[22] R. Wroe, A. T. Rowley, Journal of Material Science 31 (1996) 2019–2026.

[23] J. C. Holmes, Nuclear Powerplant Standardization: Light Water Reactors, Diane publishing, Washington, 1981.

[24] P. Medvedev, Development of Dual Phase Magnesia-zirconia Ceramics for Light Water Reactor Inert Matrix Fuel, Ph.D. thesis, Texas A&M Univeristy, 2004.

[25] Viability of inert matrix fuel in reducing plutonium amounts in reactors, Technical Report, International Atomic Energy Agency, 2006.

[26] G. S. Chang, Journal of Alloys and Compounds 444-445 (2007) 434–437.

[27] Global nuclear energy partnership, http://www.gneppartnership.org/, Accessed on April 14, 2010.

[28] Advanced fuel cycle initiative, http://afci.sandia.gov/, Accessed on May 5, 2010.

[29] P. A. Bingham, R. J. Hand, M. C. Stennett, N. C. H. and, M. T. Harrison, in: Materials Resarch Society Symposium Proceedings, volume 1107, p. 421.

[30] M. K. Meyer, U.S. Program for the development of inert-matrix fuel for transmutation systems, Technical Report, Argonne National Laboratory-West, 2001.

[31] J. J. Moore, in: 2007 ANS/ENS International Meeting and Nuclear Technology Expo, Washington D.C.

[32] C. Carter, M. G. Norton, Ceramic Materials Science and Engineering, Springer, New York, 2007.

[33] S. L. Kang, Sintering Grain Growth and Microstructure, Elsevier, Amsterdam, 2005.

[34] M. N. Rahaman, Ceramic Processing and Sintering, Marcel Dekker, New York, 2003.

[35] D. L. Johnson, Journal of Applied Physics 40 (1969) 192–200.

[36] L. A. Girifalco, Atomic Migration in Crystals, Blaisdell Publishing Company, New York, 1964.

[37] J. R. Manning, Diffusion Kinetics for Atoms in Crystal, D. Van Nostrand Company, Princeton, 1968.

[38] H. Su, D. L. Johnson, Journal of the American Ceramic Society 79 (1996) 3211–3217.

[39] J. Wang, R. Raj, Journal of the American Ceramic Society 74 (1991) 1959–1963.

[40] J. Wang, R. Raj, Journal of the American Ceramic Society 73 (1990) 1172–1175.

[41] W. S. Young, I. B. Cutler, Journal of the American Ceramic Society 53 (1970) 659–663.

[42] M. Janney, H. Kimrey, in: Spring meeting of the Materials Research Society (MRS), San Francisco, CA (United States), 16-21 Apr 1990, OSTI ID: 5193919, San Francisco, CA, 1990.

[43] NRC, Microwave Processing of Materials, Technical Report, 1994.

[44] Levinson, Method of firing ceramic articles utilizing microwave energy, 1971.

[45] I. J. C. W. H. Sutton, M. H. Brooks (Ed.), Microwave processing of materials, volume 124, Materials Research Society, Pittsburg, 1988.

[46] R. C. Metaxas, R. J. Meredith, Industrial Microwave Heating, Peter Peregrinus Ltd., London, 1983.

[47] A. De, Ultra rapid Sintering of Alumina with Microwave Energy at 2.45 GHz, Ph.D. thesis, University of Florida, 1990.

[48] A. Goldstein, L. Giffman, S. Barziv, Journal of Materials Science Letters 17 (1998) 977–979.

[49] J. Samuels, J. R. Brandon, Journal of materials science 27 (1992) 3259–65.

[50] D. E. Clark, D. C. Folz, Introduction: What is Microwave Processing?, The American Ceramic Society, Westerville, pp. 1–27.

[51] J. M. Moore, Microwave Firing of Low-purity Alumina, Ph.D. thesis, University of Florida, 1999.

[52] S. Charmond, C. P. Carry, D. Bouvard, Journal of the European Ceramic Society 30 (2010) 1211–1221.

[53] A. Goldstein, N. Travitzky, A. Singurindy, M. Kravchik, Journal of the European Ceramic Society 19 (1999) 2067–2072.

[54] J. P. Cheng, D. K. Agrawal, S. Komarneni, M. Mathis, R. Roy, Materials Research Innovations 1 (1997) 44–52.

[55] F. C. R. Wroe, in: D. E. Clark, W. R. Tinga, J. J. R. Laia (Eds.), Microwave theory and application in materials processing II, volume 36, The American Ceramic Society, Cincinnati, OH, 1993, pp. 449–459.

[56] W. Apte, P. S MacDonald, in: Microwaves: Theory and Application in Materials Processing III, volume 59, American ceramic society, 1995, pp. 55–62.

[57] I. Ahmad, Effect of Microwave Heating on the Solid State Reactions and Mass Transport in Ceramics, Ph.D. thesis, University of Florida, 1991.

[58] Z. Fathi, Surface Modification of Sodium-aluminosilicate Glasses using Microwave energy, Ph.D. thesis, University of Florida, 1994.

[59] T. T. Meek, R. D. Blake, J. D. Katz, J. R. Bradberry, M. H. Brooks, Journal of Materials Science Letters 7 (1988) 928–931.

[60] A. G. Whittaker, Chemistry of Materials 17 (2005) 3426–3432.

[61] M. Janney, H. Kimrey, W. Allen, J. Kiggans, Journal of Materials Science 32 (1997) 1347–1355.

[62] C. Degueldre, J. Paratte, Nuclear Technology 123 (1998) 21–29.

[63] D. W. Richerson, Modern ceramic engineering: properties, processing, and use in design, CRC press, 2006.

[64] E. F. Carlos, Structure Evolution of Silica Aerogel under a Microwave Field, Ph.D. thesis, Virginia Polytechnic Institute and State University, 2010.

[65] G. Roussy, J. Pearce, Foundations and Industrial Applications of Microwave and Radio Frequency Fields : Physical and Chemical Processes, Wiley, New York, 1995.

[66] ASTM, E112 standard test methods for determining average grain size, 2009.

[67] ASTM, C 20 standard test methods for apparent porosity, water absorption, apparent specific gravity, and bulk density of burned refractory brick and shapes by boiling water, 2009.

[68] R. Hutcheon, M. Dejong, F. Adams, Journal of Microwave Power and Electromagnetic Energy 27 (1992) 87–92.

[69] U. Taffner, V. Carle, U. Schafer, in: ASM Handbook, volume 1057-1066, ASM International, 2004, pp. 1057–1066.

[70] ASTM, C 1327 standard test method for vickers indentation hardness of advanced ceramics, 2009.

[71] I. Gibson, G. Dransfield, J. Irvine, Journal of material science 33 (1998) 4297–4305.

[72] M. Cologna, B. Rashkova, R. Raj, Journal of the American Ceramic Society 93 (2010) 3556–3559.

[73] K. Une, M. Hirai, K. Nogita, T. Hosokawa, Y. Suzawa, S. Shimizu, Y. Etoh, Journal of Nuclear Materials 278 (2000) 54–63.

[74] M. Maca, K. Trunec, P. Daobsak, Reviews on Advanced Materials Science 10 (2005) 84–88.

[75] H. Mehrer, Diffusion in Solids: Fundamentals, Methods, Materials, Diffusion-controlled Processes, Springer, New York, 2007.

[76] S. Swaroop, M. Kilo, C. Argirusis, G. Borchardt, A. H. Chokshi, Diffusion Fundamentals 3 (2005) 13.1–13.2.

[77] S. Swaroop, M. Kilo, C. Argirusis, G. Borchardt, A. H. Chokshi, Acta Materialia 53 (2005) 4975 – 4985.

[78] M. J. Mayo, International Materials Reviews 41 (1996) 85–115 (31).

[79] G. Suarez, L. B. Garrido, E. F. Aglietti, Materials Chemistry and Physics 110 (2008) 370–375.

[80] J. H. Booske, R. F. Cooper, I. Dobson, Journal of Materials Research 7 (1992) 495–501.

[81] D. L. Johnson, Journal of the American Ceramic Society 74 (1991) 849–850.

[82] T. T. Meek, Journal of Materials Science Letters 6 (1987) 638–640.

[83] K. Wheeler, P. Peralta, M. Parra, K. McClellan, G. Dunwoody, J. Egeland, Journal of Nuclear Materials 366 (2007) 306–316.

[84] ASTM, E228 - 06 standard test method for linear thermal expansion of solid materials with a push-rod dilatometer, 2009.

[85] R. T. Dehoff, Thermodynamics in Materials Science, Mc-Graw Hill, New York, 1993.

[86] P. G. Shewmon, Diffusion in Solids, McGraw-Hill, New York, 1963.

[87] A. Tsoga, P. Nikolopoulos, Journal of Materials Science 31 (1996) 5409–5413.